JP0650248

5.2   Analysis of Light Elements in Carbon Materials

Y. Horino*, Y. Mokuno*, A. Chayahara*, H. Yasui**, K. Awazu**,
S. Yamamoto***, K. Narumi****and H. Naramoto****
National Institute of Advanced Industrial Science and Technology*
Industrial Research Institute of Ishikawa**
Department of Material Development, JAERI***
Advanced Science Research Center, JAERI****

1. Introduction

Carbon materials such as diamond or diamond-like carbon are well known for their high hardness, low friction, excellent corrosion resistance, wear resistance and excellent biocompatibility.   Therefore, many applications of carbon materials are being under intense study. The plasma enhanced chemical vapor deposition (PECVD) using a hydrocarbon gas such as methane or acetylene is most used method to synthesize carbon materials. So the light elements such as hydrogen are involved during processing and they influence properties of the carbon materials.   In order to investigate the influences, we examine the distribution of hydrogen in some carbon materials by a nuclear reaction analysis (NRA).

The illustration of the method of the analysis is shown in Fig. 1.   The hydrogen is analyzed by a nuclear reaction analysis, NRA, based on the reaction as bellow.

$$^1H\,(\,^{15}N,\,\alpha\gamma\,)\,^{12}C$$
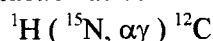
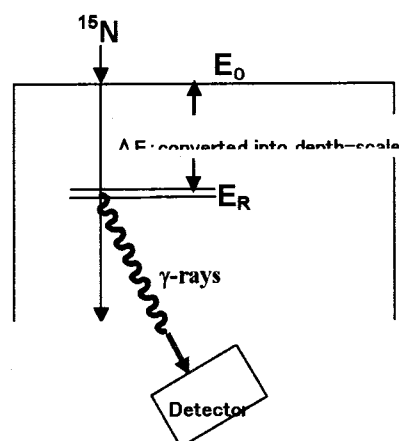(E_R=6.385MeV, width of resonance=1.8keV)
The probe ion (^{15}N) with incident energy of E_0 travels in a target material as losing its energy. When the energy becomes E_R, the nuclear reaction occurs and then γ-ray with energy of about 4.4MeV is emitted.   The depth from the surface where hydrogen exists is calculated by the energy loss of the probe ion (E_0-E_R) and the number of detected γ-ray corresponds to the amount of the hydrogen.   Therefore, by scanning the energy of the probe ion, it is able to know the depth profile of hydrogen in the materials.   As the width of the resonance of the reaction is very narrow,   the depth resolution of this method depends on the energy stability of the probe ion.   In this study, the depth resolution was about 5nm.   The hydrogen depth profiles of some carbon materials measured by this method are shown in the followings.

2. Results and discussion

2-1 Synthetic diamonds

Studies of diamond as a wide band-gap semiconductor which is one of the prospective applications of the CVD synthesis diamond are being done very well.   The · electrical
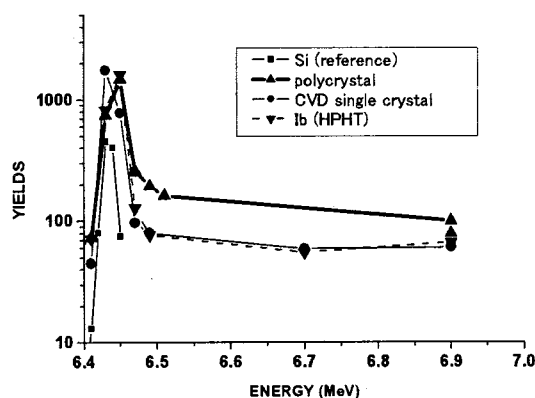

Fig. 1 Schematic of the analysis.

Fig. 2 Hydrogen profiles for 3 types of diamonds.

conductivity in the surface region of a diamond varies drastically depending on the condition of termination of the surface by hydrogen or oxygen. So information of hydrogen profile from the surface to the inside is very important for development of the devices. In Fig. 2, measured hydrogen profiles for 3 types of diamonds (Polycrystalline, CVD single crystal and HPHT single crystal) are shown[1]. In this paper, the horizontal axis of a hydrogen profile dose not show exact energy but nominal voltage of the accelerator. So there is an energy shift of a few tens keV from the real probe energy. In the case of fig. 2, the energy around 6.45MeV corresponds to the surface region of the sample and the energy higher than 6.5MeV corresponds to the inner part of it. The probe energy of 6.9MeV corresponds to about 150nm from the surface. The amount of hydrogen at inner part was about 0.2at% for the polycrystalline diamond. However, for the CVD single crystal or the HPHT single crystal, the amount of hydrogen seems less than the detection limit of the system which mainly depends on signal-to-noise (S/N) ratio. The FWHM of the hydrogen profiles at the surface region of the diamonds are larger than that of silicon which used as a reference. It could be inferred that the hydrogen has a distribution at surface region of diamonds. But the vacuum system was not good enough and there is a possibility of hydrogen adsorption from residual gas that is induced by probe irradiation. Those data indicate that it

is necessary to improve S/N ratio of the detection system and to realize measurement under good vacuum circumstances. Furthermore, surface treatments under UHV such as like sputtering are also needed.

2-2 DLC thin films

The properties of DLC (Diamond Like Carbon) are close to those of diamond. Although the hardness is less than diamond, DLC is able to be synthesized at low temperature and it has a low coefficient of friction. DLC film coatings can contribute to improving mechanical and tribological properties of materials. Therefore DLC is widely used in the field of mechanical equipments such as grinding tools.

Recently, it was found that the amount of hydrogen in the DLC affects its properties such as hardness[2]. Examinations of hydrogen quantity become quite important to use DLC films. The Fig. 3 shows the amounts of hydrogen for 3 DLC films which were synthesized from 3 source gases (methane, acetylene and acenaphthlyene). The horizontal axis corresponds to atomic percentage of hydrogen in the source gas. In the case of methane, it was found that the amount of hydrogen involved in a DLC film was about 2 times higher than that of other cases. However, the amount of hydrogen was decreased as the fluence of the probe increased as shown in Fig.4. On the other hand, the amount of hydrogen in the DLC which was made from acetylene did not decrease.
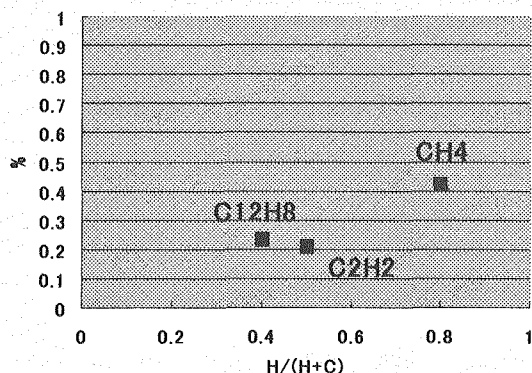

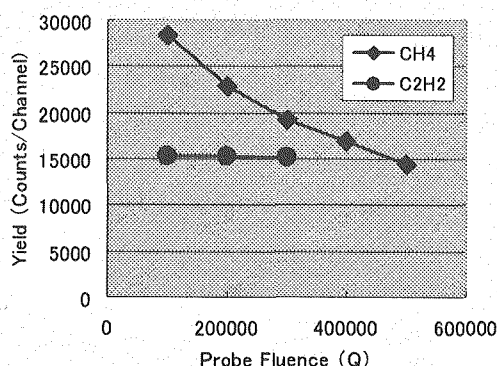Fig. 3 Amounts of hydrogen for 3 DLC films which were synthesized by 3 source gases.

Fig. 4 ^{15}N probe fluence dependence of the amount of hydrogen in DLC films.
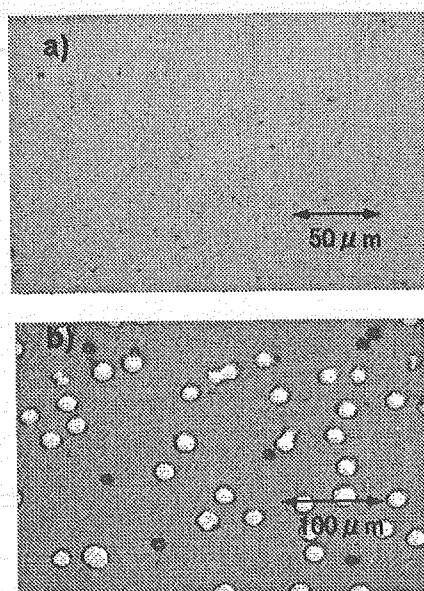
Fig.5 photographs of the surface of the DLC which made from methane, a) before and b) after hydrogen analysis observed by optical microscope.

Fig. 5 contrasts the surface change of DLC film made from methane after hydrogen analysis. The topographic change was easily recognized even under the optical microscopic observation. The analysis was done with $\sim$ ·6.5MeV ^{15}N ions at room temperature with the total dose of about 1×10^{15} ions/cm^2. From Fig.5 b), blister formation is recognized after the hydrogen analysis. The white circles correspond to blisters before rupturing, and the black ones correspond to lifting off the blister dome. The present results suggest that hydrogen atoms in this DLC are easily liberated by electronic excitation during the analysis. But the original chemical nature in this DLC may not help the easy migration and/or the trapping of hydrogen atoms, resulting in the bubble formation of hydrogen atoms on the large scale. The size distribution of bubbles seems to be small, and this process can be utilized to convert the present DLC into
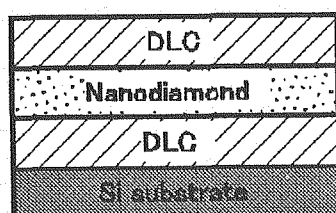

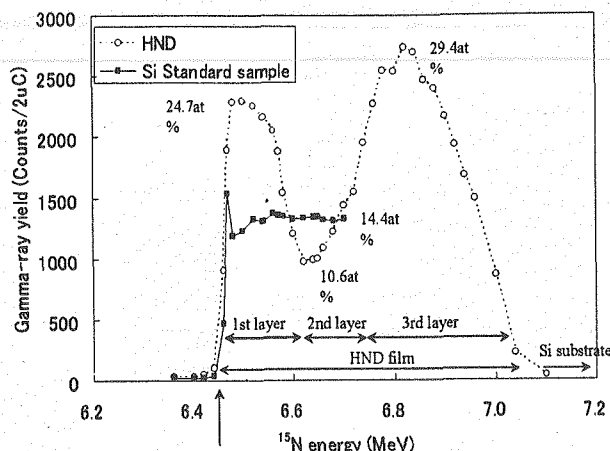Fig. 6 Cross-sectional details of the HND film.

Fig. 7 Hydrogen profile in an HND film.

porous matter with the ion beam processing.

2-3 Hybrid nano diamond (HND) films

The hybrid nano diamond (HND) film was newly developed by a group of Industrial Research Institute of Ishikawa[3]. The properties of the HND film are superior to those of DLC in hardness, wear toughness and flatness. The HND film, as illustrated in Fig. 6, is composed of alternative DLC and diamond films which are synthesized at completely different temperature and pressure of original gas materials. The measured hydrogen distribution is shown in Fig. 7. It shows two peaks and a bottom. At the peak, the amounts of hydrogen are 24.7 and 29.4at% respectively and 10.6at% at the bottom. The DLC film contains higher amount of hydrogen than diamond which has less than 1/2 of amount of hydrogen of the DLC.

References

1) Y. Mokuno, A. Chayahara, Y. Soda, Y. Horino, N. Fujimori, Synthesizing single-crystal diamond by repetition of high rate homoepitaxial growth by microwave plasma CVD, Diamond Related Materials, to be published.

2) H. Yasui, Y. Hirose, T. Sasaki, K. Awazu and H. Naramoto, Measurement of Hydrogen in BCN Films by Nuclear Reaction Analysis, Journal of Jpn. Society of Materials Science, 50, (2001) p727.

3) K. Awazu, H. Yasui, N. Ikenaga, T. Kawabata, N. Sakudo, Fabrication of hybrid nano diamond film and its properties, New Diamond, 2005, Vol.21, No1. pp.28-29.

5.3 Radiation Effect with Low Energy C_{60} Ions on Crystalline C_{60} and Si Targets

H. Naramoto[*], S. Sakai[*], K. Narumi[*], V. I. Lavrentiev[*], K. Takahiro[**],
K. Kawatsura[**], S. Nishibe[**], N. Hasuike[**], H. Harima[**],
S. Yamamoto[***] and H. Kudo[****]
Takasaki-branch, Advanced Science Research Center, JAERI[*]
Graduate School of Science & Technology, Kyoto Institute of Technology[**]
Department of Material Science, JAERI/Takasaki[***]
Institute of Applied physics, The University of Tsukuba[****]

1. Introduction

The mixture between C_{60} and a transition metal is supposed to develop the novel structures spontaneously because both components play a complementary role in the charge transfer under the influences of various applied fields. The recent effort has elucidated that the evolved structures are endowed with the electrical and magnetic properties characteristic for the nano-composites[1-5]. The structures include the carbon-allotrope-conversion through the chemical process. The directional energy beams such as ions are useful means to design the structures suitable for the application conditions.

In this report, is described the radiation-effect-study with a few 10's keV C_{60} ions onto C_{60} and Si crystalline samples together with some additional results by cobalt-implantation into C_{60} films. The ion irradiation includes the violent process depositing the energy far beyond the binding one but the careful application has been shown to be useful for the materials functionalization[6-12].

2. Experimentals

Highly pure C_{60} thin films and Si(100) were employed for the radiation-effect study using 10-50keV C_{60} ions at the beam current of 10-100nA/cm^2. In addition, 150keV Co ions were implanted into C_{60} films to study the transportation behavior of Co in a C_{60} condensed phase. Incident ions with larger mass induce the severe sputtering of the contaminant molecules and/or component species in target substances, and the development of a precise current measurement system has been a big concern for the C_{60} ion users in TIARA. We have developed the integrated counting system with two Farady cups, one for the conventional, intermittent monitoring with the larger stereographic angle (156msr) and the other for the precise measurement with the smaller one (6msr). Figure 1 illustrates a calibration curve to obtain the true current by monitoring the beam current with the conventional Farady cup. The irradiated surfaces of C_{60} films were analyzed with Raman spectrometry, Atomic Force Microscopy and step-profilometry. The step height changes were evaluated referring to the pristine region in the same sample. The lattice disorder and contaminant carbon localized on a Si surface were analyzed by RBS/channeling and RBS/nuclear reactions. In addition, the depth-sensitive Raman analysis was performed by employing the resonant process with two different UV lights (266 and 364 nm).

3. Conclusive results

In the course of irradiation the special cares were taken for the precise counting of incident ions as described in the previous section. This procedure has made it possible to evaluate the several parameters important as the universal figures for a possible comparison among the relevant scientists.

The employment of resonant Raman process with two different wavelengths in UV region was effective to detect the radiation-induced disorder in Si because the degree of disorder in the near surface region a few nms thick can not be characterized by RBS/Channeling even under the grazing exit condition. In the following, the conclusive results are listed together with the sputtering curve in Fig. 2.

1) Radiation effect on C_{60} films with 50keV self ions: At the initial stage of irradiation ($\leqq 10^{13}$ C_{60}/cm^2), the Ag(2) peak narrowing in Raman spectra was observed with the apparent increase of step height associated with faceting in AFM observation. This can be explained by a kind of recrystallization after the release of gaseous impurity atoms adsorbed in the near surface region of a C_{60} film. In the following stage ($\geqq 10^{14}$ C_{60}/cm^2), the exponential sputtering became dominant, resulting in the polymerization with the tough nature for further change. The cross-section for the sputtering was estimated as 0.41×10^{-15} cm^2 with the good correspondence to a C_2 molecule.

2) Evaluation of cobalt transportation in a C_{60} matrix by implantation technique: The Co-implantation induced the mixed structure composing of C_{60} molecules combined with Co atoms and C-clusters decomposed from C_{60} in the shallower region, and any changes were not detected in the deeper region than the projected range. The shallower region is too much distorted for the atomistic transport, and different from the usual diffusion behavior, implanted Co atoms moved into the deeper region in the temperature range of 300-570K judging from RBS analysis. The activation energy for this transport was estimated as 0.74eV. This is the first, important data to evaluate the thermal properties of C_{60}/metal mixtures.

3) Bombardment effect on Si crystals with 10-50keV C_{60} ions: The resonant Raman analyses with two different UV laser lights revealed the depth-dependent changes of the induced disorder by ion irradiation. In this report, the common features are described mainly. The bombarded surface of Si accumulates the disorder as a function of ion dose, followed by saturating behavior as evaluated by RBS/Channeling but the region never changes into amorphous completely judging from the resonant Raman analysis with 266nm light. The possible structure can be described as the nm-sized domains dispersed into the amorphized Si matrix, and the domain size is dependent on the energy and the dose of C_{60} ions. The disorder evaluated by RBS/Channeling tends to grow gradually after the dose of $\sim 3 \times 10^{13}$ C_{60}/cm^2 but the disorder evaluated through the peak shift in the resonant Raman spectrometry decreases gradually from the maximum just after $\sim 1 \times 10^{12}$ C_{60}/cm^2. This tendency was found in the samples irradiated with 10-20keV C_{60} ions. This could be associated with the recovery of the disordered region by further bombardments.

The radiation effect can be detected also as sputtering. Figure 2 illustrates the dose-dependent removal of a Si layer for 50keV C_{60} ions. One may observe the linear increase of removed thickness different from

the case for C_{60} films. The sputtering yields in Si and Co for C_{60} ions amount to 55 Si atoms/C_{60} (50keV) and 125 Co atoms/C_{60} (400keV). The sputtering rate is more pronounced in Si samples irradiated with 50keV C_{60} ions compared with that by carbon ions with the corresponding energies.

References

1) V. Lavrentiev, H. Abe, S. Yamamoto, H. Naramoto, K. Narumi, Physica B: Con. 323 (2002) 303-305.

2) V. Lavrentiev, H. Abe, S. Yamamoto, H. Naramoto, K. Narumi, Mater. Lett. 57 (2003) 4093-4097.

3) S. Sakai, H. Naramoto, Y. Xu, T. H. Priyanto, V. Lavrentiev, K. Narumi, MRS Sym. Proc. 788, L11.49.1(2004).

4) V. Lavrentiev, H. Naramoto, H. Abe, S. Yamamoto, K. Narumi, S. Sakai, Fullerene, Nanotubes and Carbon Nanostructures 12 (2004) 519-528.

5) S. Sakai, H. Naramoto, V. Lavrentiev, K. Narumi, M. Maekawa , A. Kawasuso, T. Yaita, Y. Baba, Mater. Trans. 46 (2005) 765-768.

6) H. Naramoto, X. D. Zhu, J. Vacik, Y. Xu, K. Narumi, S. Yamamoto, K. Miyashita, Phys. of Sol. State 44 (2002) 668-673.

7) X. D. Zhu, Y. H. Xu, H. Naramoto, K. Narumi, K. Miyashita, J. Phys. :Con. 14 (2002) 5083-.

8) X. D. Zhu, H. Naramoto, Y. H. Xu, K. Narumi, K. Miyashita, J. Chem. Phys. 116 (2002) 10458-10461.

9) X. D. Zhu, H. Naramoto, Y. H. Xu, K. Narumi, K. Miyashita, Phys. Rev. B 66 (2002) 165426.

10) X. D. Zhu, X. H. Wen, R. J. Zhan, H. Naramoto, F. Arefi-Khonsart, J. Phys.: Con. 16 (2004) 1175-1181.

11) X. D. Zhu, K. Narumi, Y. Xu, H. Naramoto, F. Arefi-Khonsari, J. Appl. Phys. 95 (2004) 4105-4110.

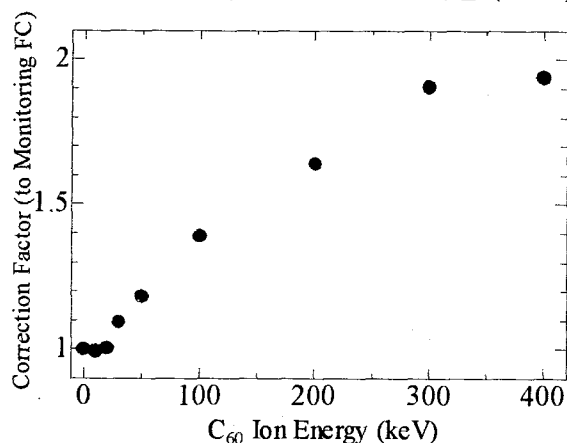12) J. Vacik, H. Naramoto, S. Kitazawa, S. Yamamoto and L. Juha, J. Phys. and Chem. Sol. 66 (2005) 581-584.

Fig. 1 The calibration curve for a monitoring Farady cup as a function of C_{60} energies. The current in the monitoring Farady cup should be multiplied by the correction factors at the corresponding energy. The discrepancy becomes more pronounced in the energy region beyond 30keV.
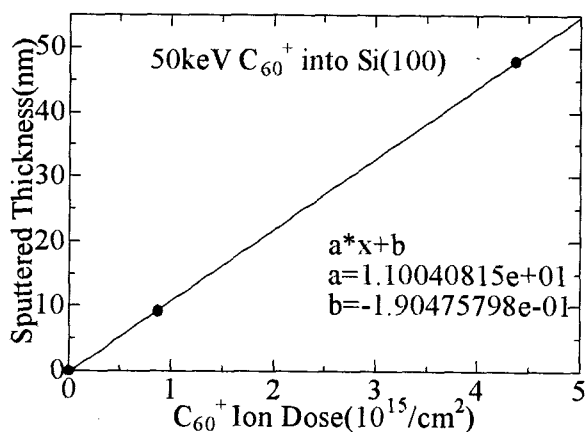

Fig. 2 Sputtering behavior of a Si target for 50keV C_{60}^+ ions. One may observe the linear change in the thickness of a removed Si layer. The sputtering yield reduced to the single carbon atoms is fairly high compared with that for single Ne ion bombardment with the same energy region.

This is a blank page.

6. Nuclear Science and RI Production

This is a blank page.

6.1   Production of Positron-emitting Cadmium Tracer for Plant Study

N. S. Ishioka*, S. Fujimaki**, N. Suzui*, S. Watanabe* and S. Matsuhashi*

Department of Ion-bam-applied Biology, JAERI*

Theoretical Analysis Group for Radiation Application, JAERI**

1. Introduction

Cadmium (Cd) is the heavy metal which is one of the environmental pollutants. Soils and drinking water contaminated with the Cd causes food pollution. The Cd ingested via food is absorbed from the gastrointestinal tract. In an acute toxicity, the Cd causes vomit and diarrhea, while in a chronic toxicity the target organ for the Cd toxicity is the kidney. To avoid Cd absorption via food, it is important that we understand the mechanisms of absorption and translocation of Cd in crop constituting a large portion of food.

There is a potential interest in using a radiotracer of Cd for plant physiological studies. Being highly useful radiotracers, ^{109}Cd and ^{115}Cd can be produced by the $^{109}Ag(p,n)^{109}Cd$ reaction using the accelerator and $^{114}Cd(n,\gamma)^{115}Cd$ reaction using the reactor. Using these radiotracers the tracer experiments have been done in plants, for example, accumulation and internal translocation of Cd in crop grains.[1] But they are a limited utilization because it has been impossible to conduct the multiple time course studies with the same intact plants.

The use of positron emitting nuclide such as ^{107}Cd ($T_{1/2}$=6.5 h) and the PETIS[2] has been expected to explain the mechanisms of Cd absorption by plants. So we are interested to explore the feasibility of cyclotron production of ^{107}Cd nuclides using the $^{nat}Ag(p,n)^{107}Cd$ reaction.

In the present work, positron-emitting radiotracer of ^{107}Cd has been developed using a proton beam from the TIARA AVF cyclotron.

2. Production of ^{107}Cd

2.1 Irradiation

We can produce 107Cd by proton bombarding a natural silver sheet of a 1 mm thick. The Ag target was irradiated for 120 min at a beam current of 2 μA; the incident energy on the target was about 17 MeV. After the irradiation, the target was led to a hot-cell from a irradiation port with a target holder by solid-target transfer system. Using manipulators the target was taken out from the target holder and collected in a polyethylene vial.

2.2 Radiochemical separation

The ^{107}Cd separation was accomplished by a precipitation method with hydrochloric acid (HCl). The chemical separation method used in this work is shown schematically in Fig.1. After the irradiation, the Ag target was dissolved in 4 ml of 14 M HNO_3. And then, HCl was added to the dissolved target solution. For making the HCl gradient condition the system needs 3 beakers. The one contained 8M HCl. The others contained ultra-pure water and the dissolved target solution. The 8M HCl was added in the ultra-pure water at a typical flow rate of 0.1 ml/min. The ultra-pure water was added in the target solution at a
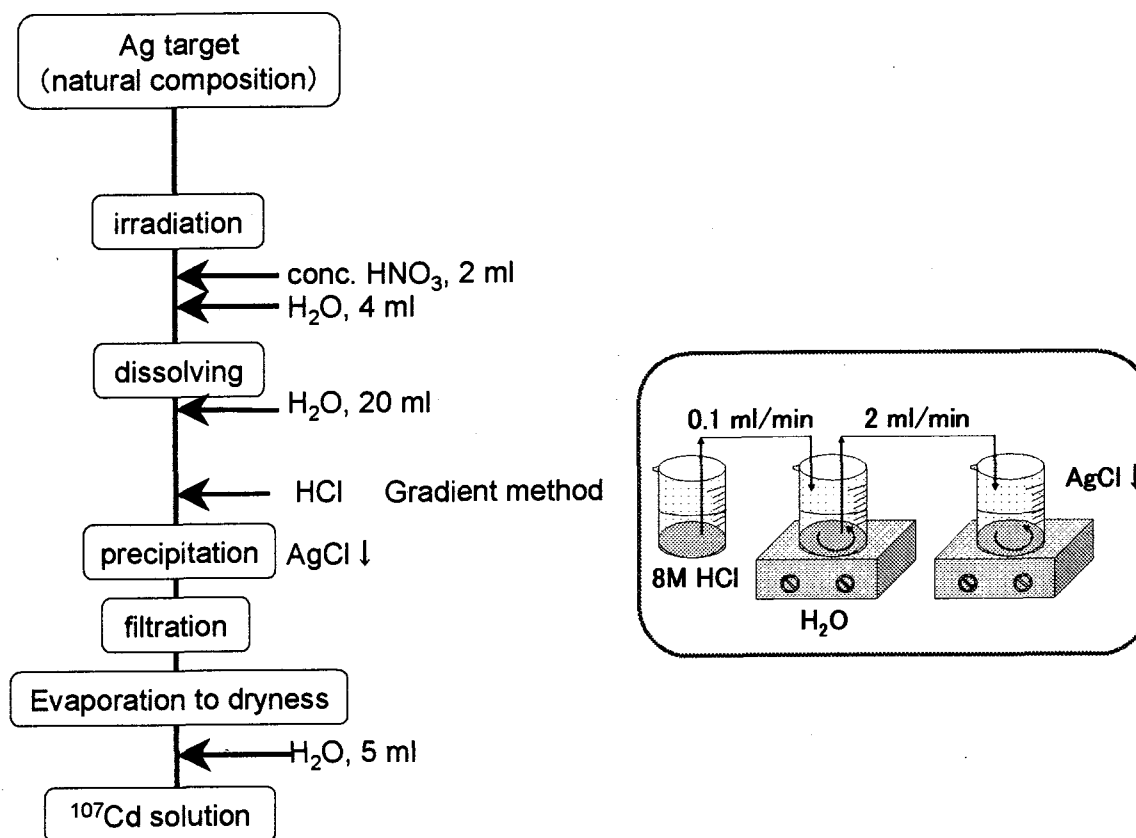
Fig.1 Chemical procedure of the separation of ^{107}Cd from an Ag target

typical flow rate of 2 ml/min. After the precipitation, the ^{107}Cd was separated from the AgCl by a filtration.

The ^{107}Cd was concentrated near dryness and dissolved in 5 ml of water. The addition of 5 ml of water and evaporation to dryness was repeated. The beaker for evaporation to dryness was inclined at an angle of forty-five degrees to avoid absorption of carrier free ^{107}Cd to the beaker wall. Finally, the ^{107}Cd was dissolved in water for subsequent plant experiments. The activity of each sample was determined by Gamma-ray spectrometry using a HPGe detector coupled to SEIKO 7600 MCA.

3. Results and Discussion

The thick target production yields were determined at 17 MeV using ^{nat}Ag targets of 1.05 mg/cm^2 to give resultant yields of ^{107}Cd 220 MBq/μAh. Table 1 shows the recovery yields of ^{107}Cd at precipitation conditions. Using the gradient-method, the radiochemical recovery of ^{107}Cd after the precipitation separation was 93%. Earlier

Table 1 Radiochemical recovery of ^{107}Cd
after the precipitation separation

Separation method	Recovery yield of ^{107}Cd	Ag content
Gradient	93%	not detected
Constant	53%	not detected

work from this laboratory[3] illustrated that the recovery yields of ^{107}Cd was about 53% by constant-method which was used precipitator of 2M HCl. No Ag impurities were detected after the both separations.

Figure 2 shows the amount of precipitator by calculation with each elapsed time. These results suggest the following. It is important that we need to keep the low concentration of HCl at the beginning of producing AgCl, and to produce the precipitation in a short period of time. The gradient-method technique avoids precipitating Cd with AgCl and the decomposition of AgCl. The decomposition of AgCl is caused by exposing the precipitation to light condition for long time. The effects of released Ag contribute to the behavior of carrier free ^{107}Cd. To know the separate mechanism of the carrier free ^{107}Cd from Ag target, it needs further consideration.

References

1) K. Tanaka, S. Fujimaki, T. Fujiwara, T. Yoneyama and H. Hayashi, Soil Sci. Plant Nutr. 49 (2003), 311-313.

2) T. Kume, S. Matsuhashi, M. Shimazu, H. Ito, T. Fujimura, K. Adachi, H. Uchida, N. Shigeta, H. Matsuoka, A. Osa and T. Sekine, Appl. Radiat. Isot., 48 (1997), 1035-1043.

3) N. S. Ishioka, F. Behrooz, S. Watanabe S. Fujimaki, S. Matsuhashi and T. Kume, The abstruct of the 40th Annual Meeting on Radioisotopes and Radiation in the Physical Sciences and Industries (2003), 12.
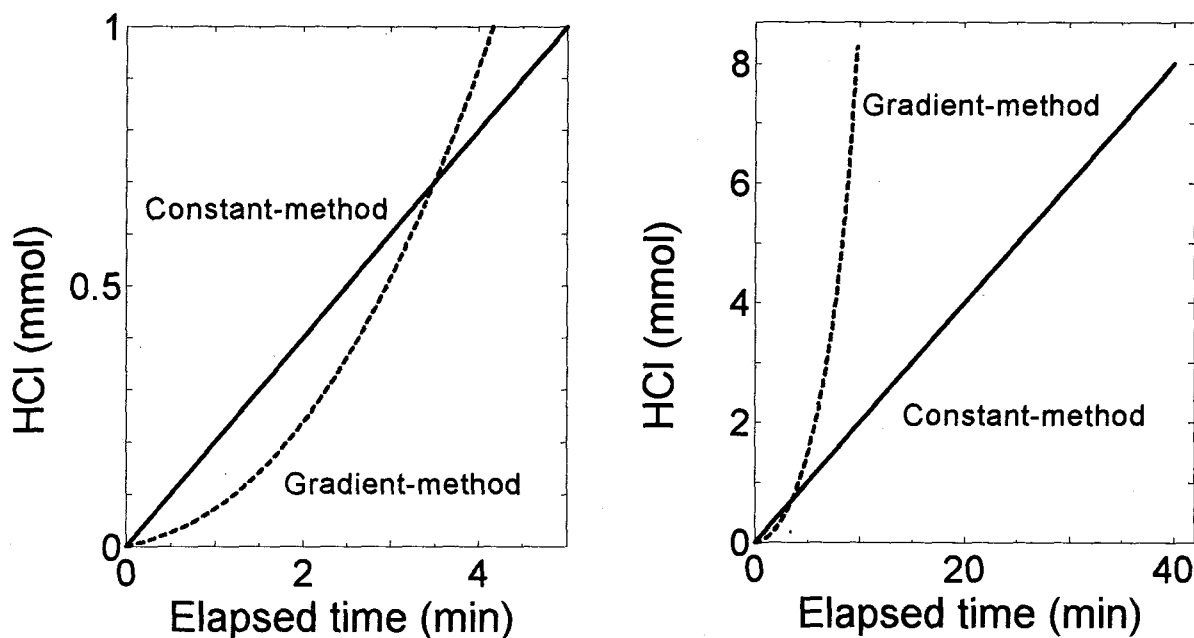
Fig.2 The comparison of a quantity of HCl precipitator in the gradient-method and constant-method: right side; the whole scale (from 0 min to 40 min), left side; an expansion of the x-axis (from 0 min to 5 min).

JP0650251

6.2 Development of Analysis Methods for Tracer Dynamics on the PETIS Data

S. Fujimaki[*,**], N. Kawachi[**], N. S. Ishioka[**], S. Matsuhashi[**] and A. Miyashita[*]
Theoretical Analysis Group for Radiation Application, JAERI[*]
Department of Ion-beam-applied Biology, JAERI[**]

1. Introduction

Today, the Positron Emitting Tracer Imaging System (PETIS) is getting popular as the unique tool for capturing the movie of positron-emitting radiotracer fed in a plant body. However, analyses of the obtained image data have not been sufficient.

Our conclusive purpose is to establish a method of mathematical analysis which leads to quantitative understanding of physiological conditions. The concrete subject to be analyzed is "time-activity curve (TAC)", the time course of activity within a selected region of interest (ROI) on a moving image. The TACs should have great information about the dynamics of tracer, thus an appropriate analysis may reveal the structural conditions which determine the dynamics.

A plant vascular bundle consists of xylem vessels and sieve tubes as flow paths, and of surrounding tissues absorbing various substances from the paths. In a previous report, we have prepared models of a vascular bundle and made clear the pattern of the four elemental TACs reflecting permeableness of the wall of flow path and the feeding manners (pulse / constant).[1] In the present study, we focused the flow speed in the path. In studies of plant responses to environmental conditions, the speeds of xylem and phloem flow are important indexes. We aimed to read a change of mass flow inside a plant body into the TAC, and examined the influence of change of the flow speed on the TAC pattern.

2. Experimental procedure

2.1 Models

Plastic strings two millimeters in diameter were set on the centers of acrylic pipes. Two percent (w/v) of agarose gel (LO3, TAKARA, Japan) was dissolved in 0.1 % (w/v) KNO_3 solution and poured in the pipes. The string was pulled out after the gel solidified to make straight path throughout the gel. The completed models were illustrated in Fig. 1.

The agarose gel is widely used for electrophoresis of DNA, a macromolecule. The $^{13}NO_3^-$ tracer ions in this experiment can enter the gel wall easily off from the flow path by simple diffusion. In addition, the gel layer completely captures the positrons emitted from tracers and prevents loss of detection by PETIS.
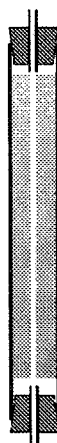
Fig. 1 Model of a vascular bundle. The pale colored parts indicate agarose gel.

2.2 Production of tracer

$^{13}NO_3^-$ was produced in the $^{16}O(p, \alpha)^{13}N$ reaction by bombarding water with a 20 MeV proton beam from the TIARA AVF cyclotron. The tracer was finally served for the experiments as 0.1 % (w/v) KNO_3 solution including $^{13}NO_3^-$.

2.3 PETIS experiments

The models were set in the view of the PETIS, and were connected to syringe pump to flow tracer solution and non-radioactive one at a constant rate. Two experiments with different patterns of tracer feeding were done. The tracer solution was flowed through the models during the measurement (constant feeding), or it was flowed only for the first 30 seconds and followed by flow of non-radioactive solution (pulse feeding). For each experiment, three models were used, and three runs of imaging were carried out with sufficient intervals for decay. The flow rate was changed and set to 0.5, 1.0, or 2.0 mL min^{-1} in each run of imaging.

2.4 Data processing

A computer program we specially made was used for extracting the TACs in the selected ROIs from the obtained image data. The ROIs were placed from upstream to downstream at even intervals of approximately 4 cm.

3. Results and Discussion

Figure 2a shows the TACs with pulse feeding. The TACs after the passage of pulse were nearly steady state. The activities at the phase indicate amounts of tracer accumulated in the respective ROIs.[1] In this experiment, the activity got lower at
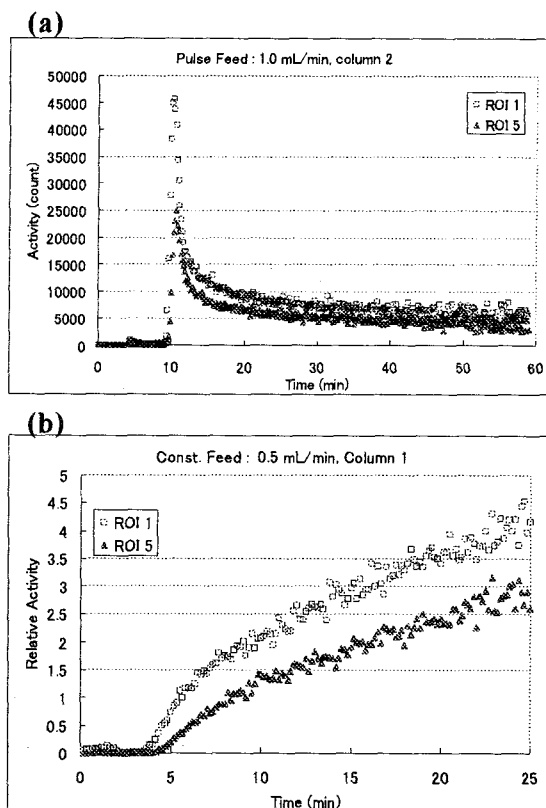

(a)

(b)

Fig. 2 TACs of an upstream ROI (ROI 1) and downstream ROI (ROI 5). (a) pulse feeding, (b) constant feeding.
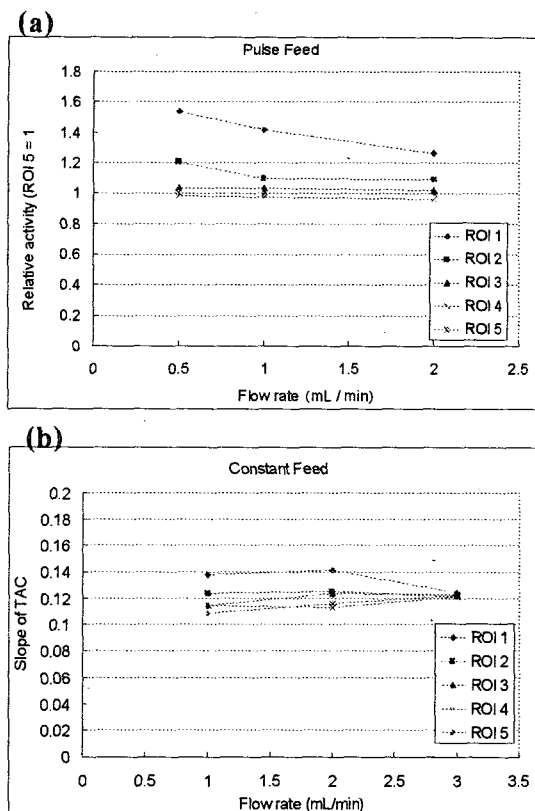

(a)

(b)

Fig. 3 (a) Activities of the ROIs at the steady state phase with different flow rates of tracer. (b) Slopes of the TACs of the ROIs with different flow rates of tracer.

more downstream ROI, and this tendency got weaker with higher flow rate (Fig. 3a). Figure 2b shows the TACs with constant feeding. The TACs showed linear increase after the first phase. Their slopes indicate the rates of tracer accumulation in the respective ROIs.[1] In this experiment, the slope got smaller at more downstream ROI, and this tendency also got weaker with higher flow rate (Fig. 3b). As a summary, the amount of accumulated tracer or the rate of tracer accumulation was higher at upstream region and lower at downstream one, but the difference got smaller with higher flow rate.

Like the models, if the unloading rate of a tracer from xylem or phloem tubes to the surrounding tissues is proportional to the concentration of the tracer in the tubes, the present result can be applied to estimation of change of the xylem or phloem flow in an intact plant body.

Reference

1) S. Fujimaki, K. Sakamoto, N. S. Ishioka, S. Matsuhashi and A. Miyashita. JAERI-Review TIARA Annual Report 2003 (2004) 242-244.

JP0650252

6.3 Measurements of Deuteron-induced Activation Cross Sections for Vanadium, Iron, Nickel and Tantalum in 14-40 MeV Region

M. Nakao*, K. Ochiai*, N. Kubota*, S. Sato*, N. S. Ishioka** and T. Nishitani*

Department of Fusion Engineering Research, JAERI*

Department of Ion-beam-applied Biology, JAERI**

1. Introduction

The IFMIF is an accelerator-based D-Li neutron source designed to produce an intense neutron field for testing fusion reactor candidate materials [1]. In the design of IFMIF, long-term operation with the total facility availability is conceived to be at least 70 %. However, activation of the structural materials of the beam transport lines by deuteron beam loss limits maintenance and makes long-term operation difficult. To estimate the activation, determination of activation cross sections (ACS) for the materials shown below is necessary. Aluminum is the main component of the beam duct and electrode. Vanadium and Nickel are the corrosion materials in Li target. Iron is the inner material of drift tube. Copper is used in the cavity walls, electrodes and magnetic conductors. Tantalum and tungsten are candidate materials for beam slits and coating to protect the beam facing components. But, there is a little or no deuteron-induced ACS data for some materials. Thus we had determined ACS data for aluminum, copper and tungsten in the past [2] and ACS data for vanadium, iron, nickel and tantalum were determined in this work.

2. Experiment and Data processing

ACS were determined by using a stacked-foil technique. The stacked-foils consisted of natural composition vanadium, iron, nickel and tantalum foils (1cm square, thickness=10-50μm). The stacked-foils were wrapped in aluminum sheet with a thickness of 10 μm and irradiated with deuteron beam accelerated by the AVF cyclotron at TIARA. After cooling, the decayed gamma rays emitted from the irradiated foils were measured by a calibrated HPGe detector and the induced activities were obtained for ^{49}Cr, ^{55,56}Co, ^{60,61}Cu and ^{178,180}Ta.

The energy degradation along the stack and the effective deuteron energy at the middle position of each foil were estimated by IRACM code [3]. The number of incident deuteron on each stacked-foil was determined from ^{65}Zn activities and the ^{nat}Cu(d,x)^{65}Zn reaction cross section data reported by Takács et al. [4]. The cross sections were derived from the induced activities and the number of incident deuterons.

3. Results

ACS determined in this work were compared with previous ones by other groups. Takács et al. [4] had determined ACS for monitor reactions (^{nat}Fe(d,x)^{55}Co and ^{nat}Ni(d,x)^{61}Cu) and comparison with these values was done to check the reliability of present ACS determination. The comparison with the value in ACSELAM library calculated by the ALICE-F code [5] was also done for evaluation of this library. The error of the present results was 13-19%. This value results from the error in the determination of continuous background for net counts of the decayed gamma-ray, the error of the standard cross sections for the ^{nat}Cu(d,x)^{65}Zn reaction, the full energy efficiency of the Ge detector and the foil thickness.

Figure 1 shows the cross sections for the ^{51}V(d,x)^{49}Cr($T_{1/2}$=42.3m) reaction. The present ACS value were 2-3 times higher than the value

reported by Weinreich et al.[6] and 4-6 times smaller than that in ACSELAM

Figures 2 and 3 show the cross sections for the $^{nat}Fe(d,x)^{55}Co(T_{1/2}=17.5h)$ and $^{56}Co(T_{1/2}=77.2d)$ reactions, respectively. For ^{55}Co, the present cross sections were in agreement with the data by Clark et al.[7] within 60% and the data by Hermanne et al.[8] within 30%. The values in ACSELAM were in agreement with the present results within 30% below 20MeV and 4-7 times higher than the present results above 20MeV. For ^{56}Co, the present cross sections were in agreement with the data by Takács et al.[4] within the experimental error and the values in ACSELAM within 2 times.

Figures 4-6 show the cross sections for the $^{nat}Ni(d,x)^{55}Co(T_{1/2}=17.5h)$, $^{60}Cu(T_{1/2}=23.7m)$ and $^{61}Cu(T_{1/2}=3.33h)$ reactions, respectively. For ^{55}Co the present results were in agreement with the values in ACSELAM within 2 times. For ^{60}Cu the values in ACSELAM were 3-7 times larger than the present results below 20MeV and in agreement with the present result within 2 times above 20MeV. For ^{61}Cu the present results were in good agreement with the data reported by Takács et al.[4]. The values in ACSELAM were 2-3 times larger than the present results by above 20MeV and in agreement with the present result within 2 times below 20MeV.

Figures 7 and 8 show the cross sections for the $^{nat}Ta(d,x)^{178}Ta(T1/2=2.4h)$ and ^{180}Ta (T1/2=8.2h) reactions, respectively. For these reactions there is no experimental data below 40MeV. The values in ACSELAM were 2-7 times higher than the present data for ^{178}Ta and 2-3 times lower than the present data by for ^{180}Ta.

4. Conclusion

Deuteron-induced activation cross sections were determined for vanadium, iron, nickel and tantalum at about 1MeV interval in 14-40 MeV region. The present results were reliable values because these values of the $^{nat}Fe(d,x)^{55}Co$ and $^{nat}Ni(d,x)^{61}Cu$ reactions were in agreement with that determined by Takács et al. In this work cross sections for the $^{nat}Ni(d,x)^{55}Co$, $^{nat}Ni(d,x)^{60}Cu$, $^{nat}Ta(d,x)^{178}Ta$ and ^{180}Ta reactions were determined for the first time. Because most of the values in ACCSELAM were over or under estimation, it needs to review the values.
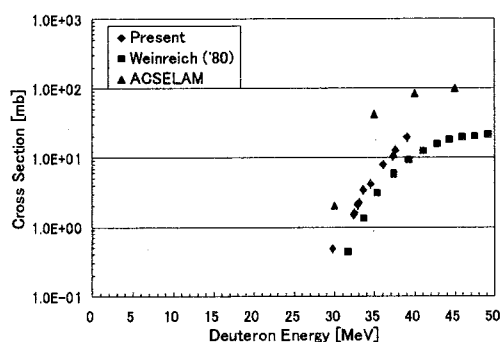

Fig. 1 Cross sections for the $^{51}V(d,4n)^{49}Cr$

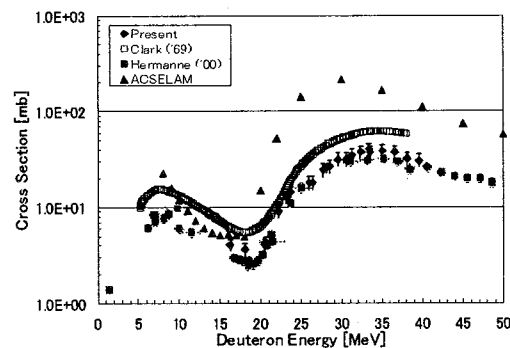Fig. 2 Cross sections for the $^{nat}Fe(d,x)^{55}Co$

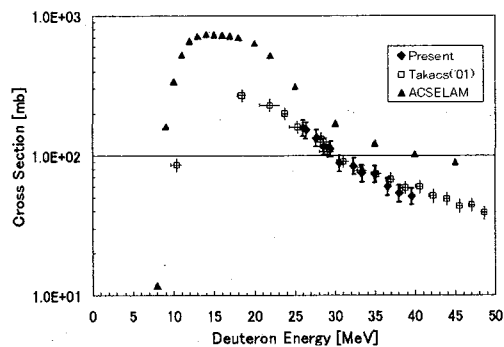Fig. 3 Cross sections for the $^{nat}Fe(d,x)^{56}Co$
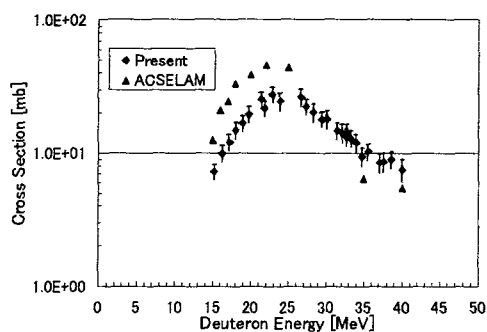
Fig.4 Cross sections for the $^{nat}Ni(d,x)$ ^{55}Co
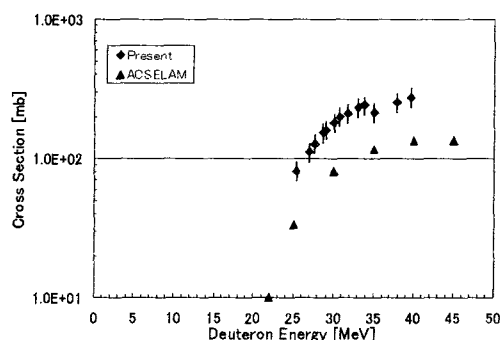
Fig.8 Cross sections for the $^{nat}Ta(d,x)$ ^{180}Ta
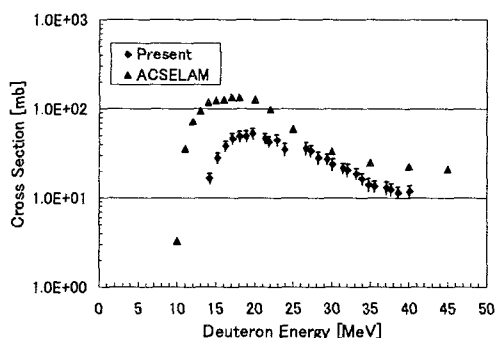
Fig.5 Cross sections for the $^{nat}Ni(d,x)$ ^{60}Cu
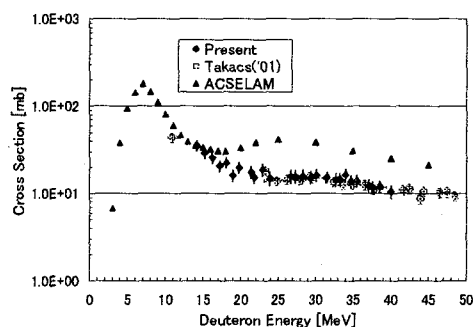
Fig.6 Cross sections for the $^{nat}Ni(d,x)$ ^{61}Cu
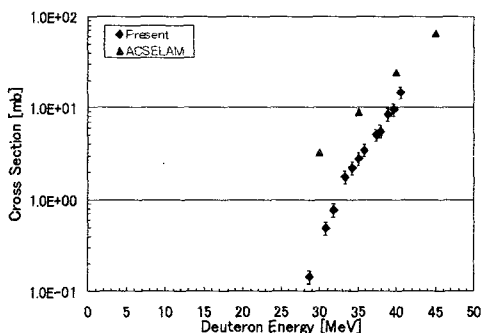
Fig.7 Cross sections for the $^{nat}Ta(d,x)$ ^{178}Ta

References

1) IFMIF International Team, JAERI-Tech 2003-005 (2003).

2) M. Nakao, J. Hori, K. Ochia, S. Sato, M. Yamauchi, N.S. Ishioka, T. Nishitani, Proc. International Conference on Nuclear data for Science and Technology, Santafe, New Mexico, 26 Sep.-1 Oct., 2004, AIP Conf. Proc. 769 (2005) 1489.

3) S. Tanaka, M. Fukuda, K. Nishimura, JAERI-Data/Code 97-019 (1997).

4) S. Takács, F. Szelecsényi., F. Tárkányi, M. Sonck, A. Hermanne, Y. Shubin, A. Dityuk, M.G. Mustafa, Z. Youxizng, Nucl. Inst. Meth., B 174 (2001) 235.

5) T. Fukahori, Proc. The Specialists' Meeting on High Energy Nuclear Data, Tokai, 3-4 Oct., 1991; JAERI-M 92-039. (1992)114.

6) R.Weinreich, H.J. Probst, ,S.M.Qaim, Int. J. Appl. Radiat. Isotope 31 (1980) 223.

7) J.W.Clark, C.B.Fulmer, I.R.Williams, Phys. Rev, 179 (1969) 1104.

8) A. Hermanne, M. Sonck, S. Takács, F. Tárkányi, Nucl. Inst. Meth., B 161-163 (2000) 178.

6.4 Production of ^{133}Xe@C$_{84}$ by Ion Implantation

S. Watanabe, T. Katabuchi, N. S. Ishioka and S. Matsuhashi
Department of Ion-Beam-Applied Biology, JAERI

1. Introduction

Endohedral fullerenes encapsulating a radioisotope attract as radiopharmaceuticals for cancer therapy. Xenon-133 ($T_{1/2}$ = 5.243 d) would be useful for cancer therapy because it emits 0.346-MeV β^- rays (maximum range in water: 1.0 mm) followed by 81-keV γ rays and conversion electrons associated with the γ transition. We made endohedral ^{133}Xe-fullerenes (^{133}Xe@C$_{60}$ and ^{133}Xe@C$_{70}$) by ion implantation[1),2)]. However, we have not succeeded in the isolation of endohedral ^{133}Xe-fullerene from empty fullerene yet. For medical application, endohedral fullerenes isolated from empty fullerenes are desired. In the present paper, we describe the production of ^{133}Xe@C$_{84}$ by implantation of ^{133}Xe ions into a C$_{84}$ fullerene target and a possibility of the isolation of ^{133}Xe@C$_{84}$ from C$_{84}$.

2. Experimental

The targets used for ion-implantation were made by vacuum evaporation of 0.2 mg of C$_{84}$ (SES Research) on Ni foils in an area of 10 mm x 10 mm. Implantation of ^{133}Xe ions was carried out with an isotope separator at an acceleration energy of 38 keV. After ion implantation, the targets were dissolved in o-dichlorobenzene. The target solutions were filtered through a membrane filter with 0.2 μm pore size (Millipore, JGWP) to remove insoluble matters. The 0.2 mL of the filtrates were injected into a column of Cosmosil Buckyprep (silica bonded with pyrenylpropyl-group, Nakalai Tesque) of 4.6 mm I. D. x 250 mm and eluted with o-dichlorobenzene at a flow rate of 1 mL/min. The concentration of C$_{84}$ in the effluent was continuously monitored with a UV detector using its UV absorption at 329 nm. The effluent was collected for every 1 mL and the ^{133}Xe radioactivity in each fraction was measured by γ-ray spectrometry.

3. Results and Discussion

Elution curves of ^{133}Xe radioactivity and C$_{84}$ concentration are shown in Fig. 1. In the elution curves, the strong correlation observed between the ^{133}Xe and C$_{84}$ peaks corroborates the
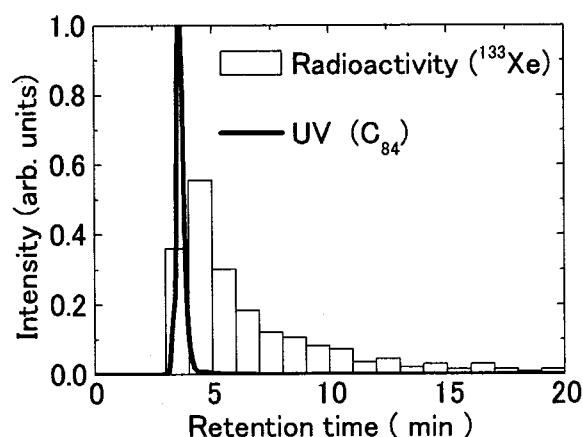
Fig. 1 Elution curves of ^{133}Xe radioactivity and C$_{84}$ concentration.

formation of $^{133}Xe@C_{84}$. The ^{133}Xe peak corresponding to $^{133}Xe@C_{84}$ was shifted about 0.5 min backward from C_{84} peak. The separation mechanism of this column is interaction of π electrons between the fullerenes and the column material (pyrenylpropyl-groups). Therefore, the shift of $^{133}Xe@C_{84}$ peak was considered to be caused by the change of the electronic state of π electrons in the fullerene molecule encapsulating ^{133}Xe atom.

For $^{133}Xe@C_{60}$ and $^{133}Xe@C_{70}$, we have not observed the shift of endohedral ^{133}Xe-fullerene. The shift of $^{133}Xe@C_{84}$ peak in this study suggests a possibility of isolation of endohedral ^{133}Xe-fullerene from empty fullerene.

References

1) S. Watanabe, N. S. Ishioka, T. Sekine, A. Osa, M. Koizumi, H. Shimomura, K. Yoshikawa, H. Muramatsu, *J. Radioanal. Nucl. Chem.*, **255** (2003) 495.

2) S. Watanabe, N. S. Ishioka, H. Shimomura, H. Muramatsu, T. Sekine, *Nucl. Instr. Meth. Phys. Res.*, **B 206** (2003) 399.

This is a blank page.

7. Microbeam Application

JP0650254

7.1 Focused Microbeam Formation for Heavy Ion Beam from AVF Cyclotron

W. Yokota, T. Satoh, M. Oikawa, T. Sakai, S. Okumura, S. Kurashima,
N. Miyawaki, H. Kashiwagi and M. Fukuda
Advanced Radiation Technology Center, JAERI

1. Introduction

A microbeam formation system is being developed at TIARA with which heavy ion beams accelerated to above a hundred MeV by the AVF cyclotron are focused down to 1 μm with a quadruplet quadrupole lens. The microbeams will be applied to biomedical science such as radio microsurgery and mutagenesis as well as study of single event upset of semiconductors for space environment. The major component of the system was installed in the HX vertical beam line in the 1st heavy ion room and the test operation started in 2002. The detail of the system is described in Ref. 1. In 2003, a beam spot diameter of 70 μm was observed. The flat-top acceleration system was installed in the cyclotron[2] in order to permit energy spread ($\Delta E/E$) less than 0.02% which is necessary for 1 μm spot formation.

In 2004, the focusing and the bending magnets and the diagnostic elements on the beam lines of HA and HX were re-aligned with a maximum correction of 2 mm. The beam steerer upstream of the micro-slit was replaced with a beam shifter. As a result, more precise beam transportation has been allowed in shorter tuning time, where beams pass through a pair of the micro slit and the divergence defining slit aligned in series with very small acceptance. Furthermore, it was found that a coil current for a beam scanning magnet, which scanned the beam spot on the target for spot size measurement, oscillated even when the control input voltage was zero. The inductance, the resistance and the capacitance of the coil and the cables together with the current supply might make up an oscillator circuit. The oscillation was removed by putting a capacitor in parallel with the scanning coils. The beam spot size was remarkably reduced as a result of these treatments.

2. Formation and measurement of beam spot

The beam of 260-MeV Ne accelerated with the flat-top acceleration system was used in the experiments. The microbeam was scanned two dimensionally on a tantalum mesh or a copper grid at the focal point by the scanning coil magnets. Before the oscillation was found, the intensity of beam passing through the mesh holes was measured by a scintillator ($CaF_2(Eu)$) with a photo multiplier. The values of the scanning coil currents were used as X-Y position of the beam. The detail of the

100μm
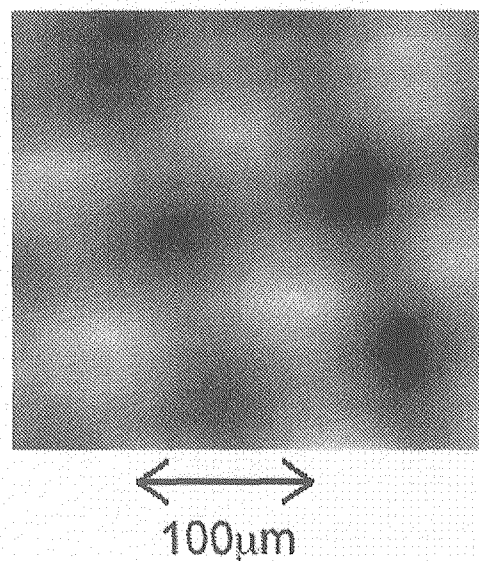
Fig.1 Image of the mesh obtained from the intensity of ion beam passing through the mesh holes. White circles are spaces.

measurement system is reported in Ref.3. The slit gaps and the quadrupole lens currents were adjusted so as to make the mesh image as clear as possible under real-time observation of the image. The obtained image shown in Fig. 1 is quite out of focus. The oscillation might take place in this case. We used detection of secondary electron emitted from the grid by means of a plastic scintillator with a photo multiplier after the oscillation was removed. The obtained grid image is remarkably sharp as shown in Fig.2. The beam spot size was estimated from the width of the electron intensity peak at the grid edge (Fig.3), and the smallest was below 2 μm. This is currently the smallest in the world for the cyclotron heavy ion beams above a hundred MeV.

3. Summary

The beam spot size below 2 μm was obtained using 260-MeV Ne beam in the successive four experiments performed after November in 2004, and a 1 μm diameter is expected to be attained around the middle of 2005. The test irradiation of the microbeam is planed to living cells in the atmosphere and to semiconductors in early 2006.

The trajectory and the intensity of the beam sometimes changed suddenly or gradually with time. Instability in the cyclotron magnetic field, the ion source plasma or acceleration voltage etc. might cause the changes. They are the subjects to be solved before regular microbeam application that will start in a few years.

References

1) M. Oikawa, T. Kamiya, T. Satoh, M. Fukuda, S. Kurashima and N. Miyawaki, JAERI-Review 2003-33 (2003) 267-269

2) M. Fukuda, S. Kurashima, N. Miyawaki, S. Okumura, T. Kamiya, M. Oikawa, Y. Nakamura, T. Nara, T. Agematsu, I. Ishibori, K. Yoshida, W. Yokota, K. Arakawa, Y. Kumata, Y. Fukumoto and K. Saito, Nucl. Instr. and Meth. B210 (2003) 33-36

3) T. Satoh, M. Oikawa, T. Sakai, M. Fukuda, S. Okumura, S. Kurashima, N. Miyawaki and T. Kamiya, JAERI-Review 2004-25 (2004) 253-255
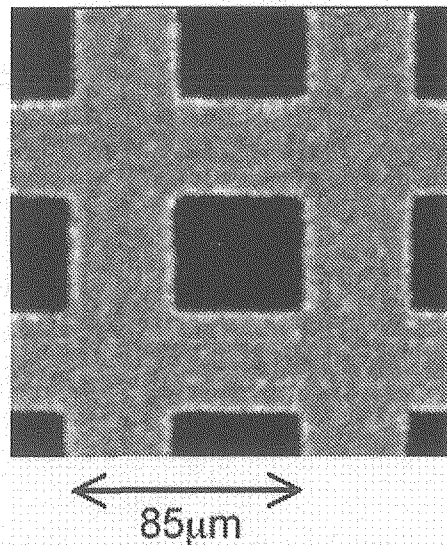
Fig.2 The secondary electron image of the copper grid. Black squares are spaces.
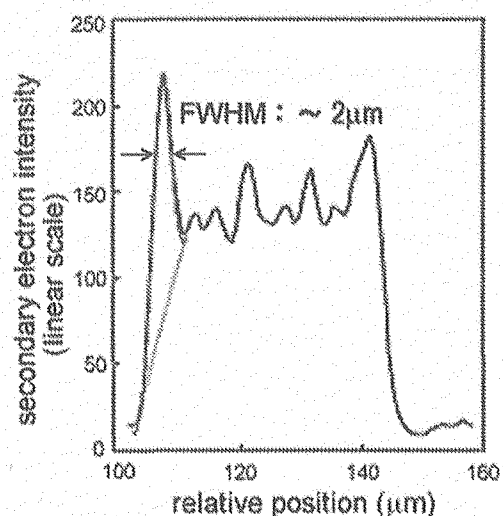
Fig.3 One dimensional distribution of secondary electron intensity across the grid. The beam spot size was estimated from a peak width at a grid edge.

JP0650255

7.2 Micro-PIXE for the Study of Atmospheric Environment

M. Kasahara*, C.- J. Ma*, M. Okumura*,
T. Kojima**, T. Hakoda**, M. Taguchi**, T. Sakai*** and Y. Ohara***
Graduate School of Energy Science, Kyoto University*
Department of Material Development, JAERI**
Advanced Radiation Technology Center, JAERI***

1. Introduction

The nucleation scavenging of aerosols in clouds refers to activation and subsequent growth of a fraction of the aerosol population to cloud droplets. Clouds are a major factor in the Earth's radiation budget, reflecting sunlight back to space or blanketing the lower atmosphere and trapping infrared radiation emitted from the Earth's surface. Also the properties of aerosols in cloud have an influence on different heating/cooling rates. The ability of a given particle to serve as a nucleus for water droplet formation will depend on its size, chemical composition, and the local supersaturation. Thus, to know the characteristics of cloud is one of key issues in understanding the cloud scavenging mechanism as well as the Earth's radiation budget.

In this study, to investigate the characteristics of cloud a huge vertical mine located in Kamaishi City, Japan was employed for cloud generation experiment. A huge vertical pit employed as the real-scale chamber for artificial cloud generation in this study is also one of the extinct iron-copper mines located at steep mountains and valleys. Due to the subterranean water, the atmosphere of vertical mine (approximately 10 °C temperature) is always wetted with relative humidity (Rh) near 100%. Thus background cloud is always forming.

Here, we report the physical properties of cloud artificially generated at a huge vertical chamber. We also describe the cloud chemical characteristics concentrated on individual cloud droplets.

2. Experimental procedure

A huge experimental chamber consists of a vertical pit with 430 m height and 5.5×2.9 m^2 cross sectional area. Since upward motion of moist air is an essential prerequisite for cloud formation, air parcel should be lifted to top of pit. The ascending air parcel wind speed was controlled by two large ventilators at the top of pit. The polydisperse dry particles were generated from the three-step concentrations of NaCl solutions by an atomizer (TSI 3076) at bottom of pit.

In order to collect individual cloud droplets, the collodion film replication method introduced from Ma et al.[1] was applied. Since the droplet replication process was already described in former studies[1,2], it was noted here briefly. A viscous collodion solution was mounted onto the Mylar film just before sampling. Cloud droplets adhere onto the thin layer of collodion film, and then they gently settled without bounce-off. After evaporation of alcohol and ether from collodion, a thin film containing the replications of individual cloud droplets was left. The chemical composition of residual material on droplet replica was be determined by micro-Particle Induced X-ray Emission (PIXE). Micro-PIXE analysis was performed at the division of Takasaki Ion Accelerator for Advanced Radiation Application (TIARA) in Japan Atomic Energy Research Institute (JAERI). Single droplet replica was scanned by

2.6 MeV H^+ micro beam accelerated by 3 MV single-ended accelerator.

3. Results and Discussion

To estimate the number size distribution cloud droplets at upper of pit , we measured the size of individual cloud droplet replicas for each three-step cloud generations by microscopic (Keyence, VH-7000) observation. Figure 1 shows the size spectra of droplet number concentration formed by background particles and dry NaCl particles generated from three-kind solution types. The number size distributions of droplets are bimodal showing the peaks around 9 μm and 20 μm for every case. The strong decrease of the droplet number concentration between 14 μm and 16 μm was observed. Also they show the slightly positive skewness with the tail toward larger sizes. From the droplets spectra, it can be suggested that droplet number concentration strongly depends on the droplet size. Also these spectra suggest that the particle affecting the cloud droplets within the air mass was quite different among the properties of CCN particles. As one of possible reasons for this bimodal spectrum, because the newly activated droplets are much larger than the pre-existing background ones, the second peaks might be developed. Figure 2 exhibits an example of individual droplet replicas

Fig. 2 An example of micro-PIXE spectrum and Cl map on a single cloud drop formed under NaCl particle nebulization.

Fig. 1 Size spectra of droplet number concentration formed by different solution type.

(upper left), Cl map on a single cloud droplet formed under NaCl particle nebulization (upper right), and micro-PIXE spectrum (below). As shown in Fig. 2, the micro- PIXE spectrum and elemental map were successfully drawn for a single cloud droplet formed. Chlorine with absolutely high peak was distributed on a whole droplet with about 30 μm diameter. Also the NaCl residue with strong X-ray count for Cl is concentrated in the center of elemental map. Both chemical inhomogeneities and homogeneities in individual droplet replicas were obviously observed from micro-PIXE elemental images. Since the number of single droplet analyzed by micro-PIXE is not enough, though we cannot discuss the detail ratio that how many droplets are incorporating NaCl particles (or background mineral particles), it can be suggested that the internal and external mixtures of particles of different chemical composition was at least partly preserved in the droplet phase.

Consequently, through the results of micro-PIXE analysis we can presume the behavior of CCN particles.

Figure 3 displays the schematic view for the life cycle of cloud droplet in the vertical mine chamber. The numbers labeled at both sides mean height scale of vertical pit and time scale of air parcel by fixed updraft velocity, respectively. In the real atmosphere the mechanisms of lift air are orographic lifting, frontal lifting, convergence, and localized convection due to instability, while in the present vertical chamber air parcel was ascended (W) by high volume ventilator installed at the top of mine. The introduction of artificial NaCl CCN (P_C), formation of initial droplet (D_I), condensation growth (D_G), and falling droplet (D_F) in the vertical transport are important processes that determine the droplet size distribution, droplet number concentration, and W_L in the vertical fixed environment. And then, cloud droplet number concentration, which is largely determined by how many aerosol particles are activated as CCN, influences cloud droplet size, liquid water concentration, reflectivity, and precipitation. Here, the parameter A_S determines the potential for droplet growth. Since the particle growth rate is variable according to Rh and particle species in the early period of cloud generation, the different Rh should be continuously handled to determine the deliquescence behavior of NaCl particles. However, in the present study, we cannot discuss about this point because, as mentioned earlier, the subterranean water of vertical mine makes the mine atmosphere always wet with Rh near 100%. At a slight supersaturation, when the Rh can become greater than the critical value, the droplet will leave the equilibrium state and grow without limitation by condensation of water

P_C: CCN particle D_I: Initial droplet
D_G: Droplet growth D_F: Falling droplet
V_t: drop's terminal velocity A_s: Saturated air
V_g: ground relative fall W: updraft velocity
  speed of the drop
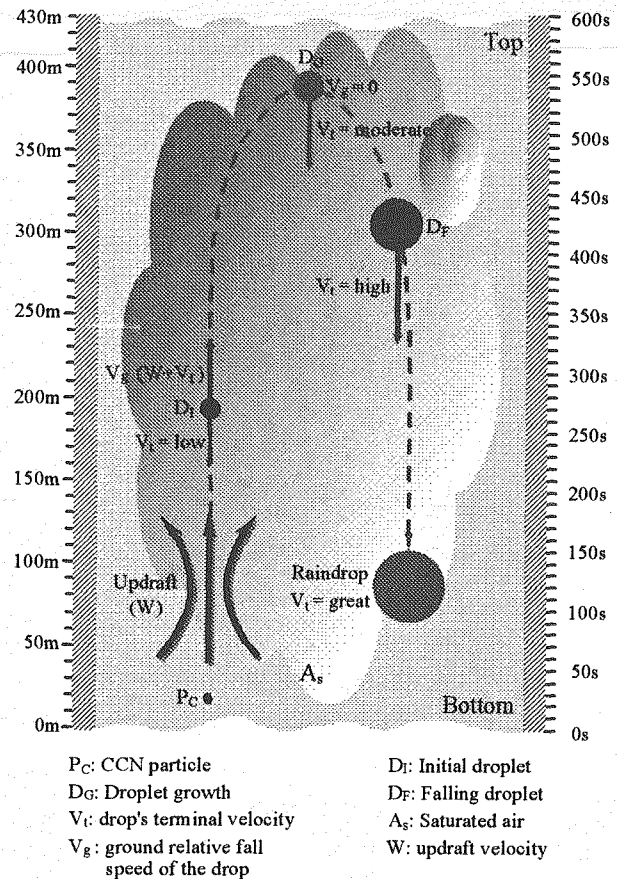
Fig. 3 Schematic view for the cycle of cloud droplet in the vertical mine chamber.

vapor. This step (D_G in Fig. 3) is called activation. In addition, coalescence of these large droplets is responsible for growth of droplets. Large droplets (D_F in Fig. 3) play a very important role in the initiation of warm rain and their concentration gives an influence on the broadness of the droplet size distribution.

References
1) C.-J. Ma, M. Kasahara and S. Tohno, Water, Water, Air and Soil Pollution 130 (2001) 1601-1606.
2) C.-J. Ma, M. Kasahara, S. Tohno and T. Sakai, Atmospheric Environment 37 (2003) 4679-4686.

JP0650256

7.3 Research Activities using Micro-PIXE on the Study of Elements Accumulation by Microorganisms in The Fiscal Year 2004

T. Ohnuki*, F. Sakamoto*, N. Kozai**,

T. Sakai***, M. Oikawa*** and T. Satoh***

Advanced Science Research Center, JAERI*,

Department of Environmental Science, JAERI**,

Advanced Radiation Technology Center, JAERI***,

1. Introduction

The presence of radionuclides in nuclear reactors and radioactive wastes is a major environmental concern due to their radiation emissions. In order to estimate the potential impact of radionuclides to human being, we must elucidate the migration behavior of the elements involving radionuclides in geological and terrestrial environment. Abiotic and biotic reactions of the elements should be considered to estimate the impact. In last three decades, many researchers have studied the interactions between the elements and inorganic materials. However, the biotic reactions of the elements have received less attention.

Some microorganisms can accumulate the elements on cell surface and inside cell. Great amounts of elements accumulation have been reported and have been expected to apply remediation methods for the contaminated area. Fundamental understanding of the interaction between the elements and microbes is needed to develop appropriate waste treatment and management strategies as well as to predict the microbial impacts on the long-term performance of the waste repositories.

State-of-the-art analytical techniques should be used to determine the interaction of elements with microorganisms at the molecular level to understand the structure function relationship.

Particle induced X-ray emission (PIXE) is one of the possible methods detecting elements in the level of ppm[1]. If we use probe beams of μm order or less in diameter, hazardous elements as well as other elements distribution in a lower plant sample can be determined with such spatial resolution. A light ion microbeam system[2] with the spatial resolution of less than 1 μm was constructed on a beam line of 3 MV single-ended accelerator in the TIARA facility at Japan Atomic Energy Research Institute (JAERI). And the in-air μ-PIXE analyzing system was developed on the TIARA facility for chemical analysis with a sub-micron level spatial resolution[3]. Thus, mapping of hazardous elements of ppm level is available by μ-PIXE.

In fiscal year 2004, we have conducted the following experiments using μ-PIXE analysis.
(i) Accumulation of Co by *Saccharomyces cerevisiae*.
(ii) Accumulation of Pb by *S. cerevisiae*.
Here, we report the detail of accumulation of Co by *S. cerevisiae*.

2. Objective

Cobalt exists in low-level radioactive wastes. This indicates that the interaction of Co with microorganisms should be elucidated to understand the impact of radioactive waste to environment. The yeast *S. cerevisiae* is a

eukaryot that has a cell sized of approximately 10 μm in diameter. The yeast is known to be accumulate metals[4]. Thus, the μ-PIXE technique was used to examine the accumulation and localization of Co and the essential elements such as, P, K and Fe in yeast.

3. Experimental

The yeast of *S. cerevisiae* X-2180 was obtained from National Research Institute of Brewing, Japan and was grown in on YPD medium containing the following ingredients: yeast extract (Difco), 10 g; peptone (Difco), 20 g; glucose (Difco), 20 g and agar (Difco), 20g in 1 L DDI. The cells were grown in 100 ml of YPD broth in 500 ml flasks for 24 hours at 30 °C on a shaker at 110 rpm.

The yeast cells were added to 100 ml of YPD medium containing 0.1, 0.5, and 1.0 mM of Co. Effect of Co on growth of the yeast was determined by removing an aliquot at 0.1, 21 and 48 h and measuring the optical density at 600 nm (OD_{600}).

The yeast cells grown in the presence of Co were removed from the growth medium at 0.1, 21 and 48 h, washed twice with DDI and attached on the sample folders, freeze-dried, and analyzed by μ-PIXE. A proton beam with the energy of 2.6 MeV from the single-ended machine was used for in-air μ-PIXE analysis[3], so that the proton penetrates into the yeast exciting elements both on the surface and internal region of the yeast. The beam spot was approximately 1 μm in diameter. The maximum scanning area available at the μ-PIXE set-up was of 740 x 850 μm^2. In μ-PIXE analysis peak intensity of element was normalyzed to that of S.

The chemical states of Co accumulated in yeast cells were examined by X-ray absorption fine structure (XAFS).

4. Results and summary

Presence of Co slowed the growth. Micro-PIXE analysis showed that the intensity of Co peaks in the PIXE spectrum increased with an increase of OD_{600}, and with an increase in Co concentration. The intensity of Fe peak in the yeast samples cultured in the nutrients containing Co of 0.5 and 1 mM was higher than that of the control samples, while the intensities of P and Zn were the same as those of the control samples. The intensity of K peak was kept at approximately 0.2-fold of the control samples up to 0.3 OD_{600}, then increased with an increase of OD_{600} to be attained the same intensity of the control samples. XAFS spectrum of the accumulated Co in the yeast indicated that distance and coordination numbers of the nearest neighbor oxygen was the same as $Co(NO_3)_2$, and the second neighbor atom was detected suggesting complexation of Co with the functional group of the yeast

These results indicate that Co association with yeast is accompanied with the increase of Fe uptake and the decrease of K uptake. It is concluded that interaction of hazardous element with microorganisms affests the migration behavior of not only hazardous element itself, but also those of essential ions of microorganisms in the environment.

References

1) S. Sueno, Eur. J. Mineral., 7, (1995) 1273-1297.

2) T. Kamiya, T. Suda and R. Tanaka, Nuclear Inst. Method B 118 447-450(1996).

3) T. Sakai, et al., Biological Trace Element Research 71-72 (1999)77-82.

4) B. Volesky, H.A. May-Phillip, Appl Microbiol Biotechnol 42 (1995) 797.

JP0650257

7.4 Development of a Very Fast Beam Chopping System

T. Sakai, M. Oikawa, T. Satoh
Advanced Radiation Technology Center, JAERI

1. Introduction

In TIARA facility, the light ion microbeam system is mainly used for elemental analysis such as PIXE and PIGE techniques [1]. In those analytical methods, relatively high current beam is required. On the other hand, single ion hit systems have been installed in two heavy ion microbeam systems, which are connected to a 3MV tandem accelerator and an AVF cyclotron. [2,3] The single ion hit technique is very unique tool for the studies on single event effects in semiconductor devices and several interesting radiobiological processes known as bystander effect [4].

In the present work, we have developed and installed a very fast beam chopping system in the external light ion microbeam system. The system provides a very fast pulsed beam within 1μm spatial resolution. This technique is a promising tool not only for single ion hit applications, but also for time-resolved analytical methods such as ion-induced fluorescence lifetime measurement.

2. Fast beam chopping system

The beam chopping has two purposes, namely providing the timing signal and reducing the beam current to single ion hitting level. An electrostatic fast beam chopping was introduced to meet this requirement by controlling injection timing and shortening the width of beam pulse to limit the active time of ion injection to the sample.

A pair of conical shape electrodes and 50 Ω coaxial cables were used to reduce the refraction in fast deflection pulses due to impedance mismatching. The gap between the
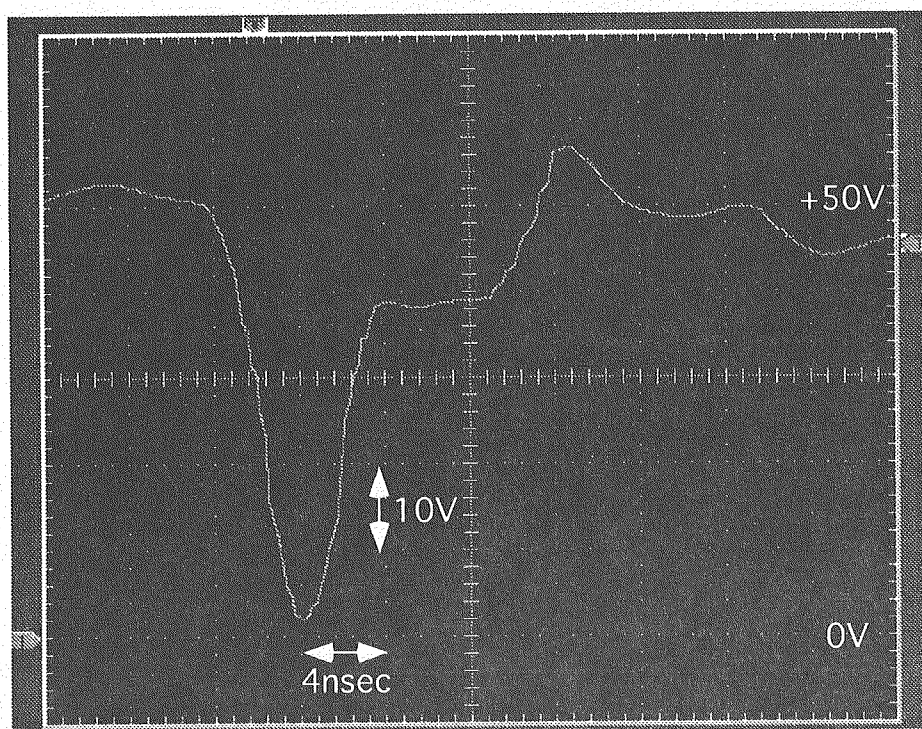
Fig. 1 An oscillographic trace of the output pulse applied to the conical shape electrode.

Microbeam-line (SB)

Newly installed
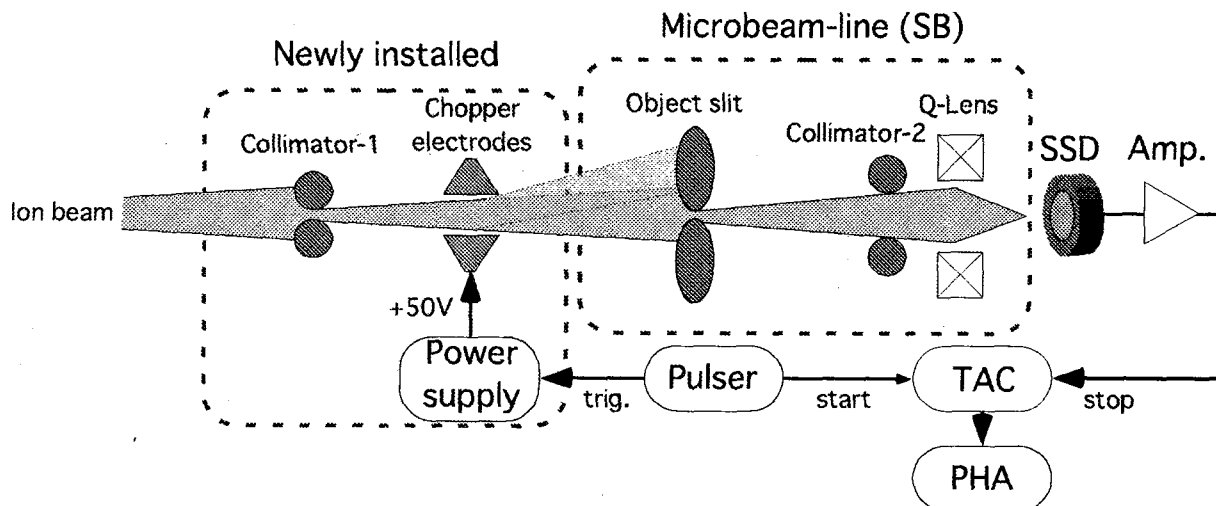
Fig. 2 Schematic diagram of the beam chopping and time spectrum measurement systems.

electrodes was 0.2 mm. A custom-made high voltage power supply (Matsusada Precision Inc.) provides very fast pulse (p.p. 50V). The details of the system is described elsewhere [5]. The waveform of the pulse is shown in Fig. 1.

A beam current reduction rate is roughly the same as a product of repetition rate and the pulse width. When the pulse width is 10 nsec with 1000 Hz repetition rate and the 10 pA beam current, nearly 600 ions come to the sample periodically in a second.

3. Experiment

The pulsed beam is formed by a fast

FWHM
6.0 nsec
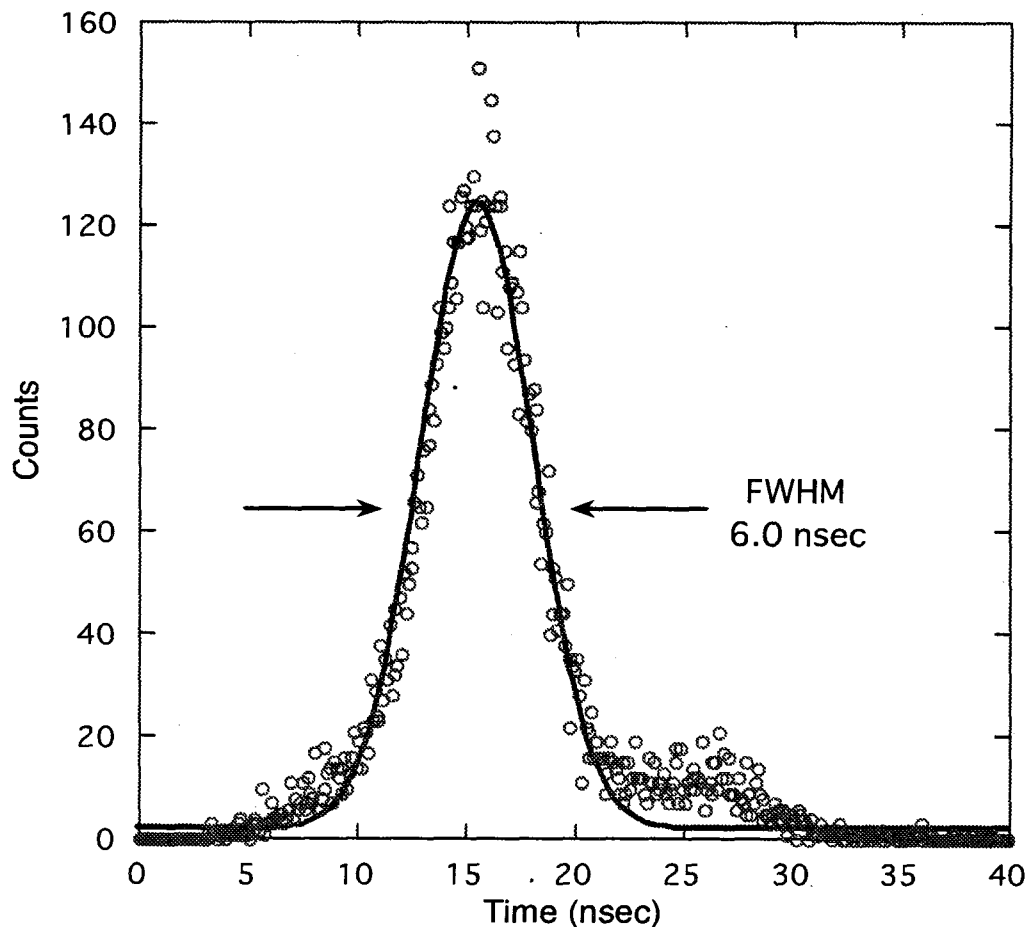
Fig. 3 Measured time spectrum of the pulsed beam.

beam deflection and a collimation in the beamline. Figure 2 illustrates a schematic diagram of the beam chopping and time spectrum measurement systems. Normally the high voltage of the fast beam chopper is applied to a deflector electrode (beam off). When a beam injection requirement trigger is formed by the research pulser (STANFORD RESEARCH SYSTEMS, DG535), the high voltage power supply outputs a fast pulse (beam on). The pulse repetition rate can be changed up to 1 MHz.

The time spectrum of the pulsed beam is shown in Fig. 3. A time to amplitude converter and a pulse height analyzer were used to measure the spectrum. The initial ion beam current was reduced to less than 0.0001 ions/pulse in order to minimize the probability that one pulse includes plural ions. The pulse width of 6 nsec (FWHM) is successfully achieved by this method.

4. Conclusions

A very fast beam chopping system has been developed and installed in the external light ion microbeam system. The combined system provides 6 nsec width pulsed ions within 1μm spatial resolution in-air environment.

The first step of development for time-resolved precise irradiation technique was completed in this work. In near future, we will start ion-induced fluorescence measurement for biological and radiation chemistry studies.

References
1) T. Sakai, T. Kamiya, M. Oikawa, T. Sato, A. Tanaka and K. Ishii , Nucl. Instr. Meth. B190 (2002) 271.
2) T. Sakai, T. Hamano, T. Suda, T. Hirao, T. Kamiya, Nucl. Instr. and Meth. B130 (1997) 498.
3) Y. Kobayashi, M. Taguchi, S. Okumura and H. Watanabe, JAERI TIARA Annual Report 1995 (vol. 5) p38.
4) H. Nagasawa and B. J. Little, Cancer Research 52 (1992) 6394.
5) T. Sakai, Y. Naitoh, T. Kamiya, Y. Kobayashi, Nucl. Instr. Meth. B158 (1999) 250.

JP0650258

7.5 Nuclear Reaction Analysis of Boron Doped in Steel with Microbeam

H. Shibata*, Y. Kohno**, Y. Hosono***, K. Amemiya****, T. Satoh*****, M. Oikawa***** and T. Sakai*****

Graduate School of Engineering, Kyoto University*
Department of Materials Science and Engineering,
Muroran Institute of Technology**
School of Engineering, The University of Tokyo***
National Institute of Advanced Industrial Science and Technology****
Advanced Radiation Technology Center, JAERI*****

1. Introduction

Recently the microanalysis of trace amount of elements by using PIXE and PIGE becomes a very powerful tool for various research fields. In addition an in-air measurement system by proton microbeams is developed for biomedical research, dental study, environmental science, geology and so on [1]. This system enables sample handling easier in atmospheric environment with spatial resolution of ~1 μm.

An addition of trace amount of boron to steel materials improves mechanical properties. Behavior of boron additive, however, is not sufficiently understood because of the difficulty of microscopic analysis, although boron treatment substantially may prevent hydrogen from segregating at grain boundaries. Recently imaging of boron distribution in a cell has been also required to elucidate the mechanism of BNCT (Boron Neutron Capture Therapy). These requirements to analyze the behavior of 20-50 ppm boron in materials with a good spatial resolution stimulates us for developing an imaging technique of trace amount of boron distribution by using PIGE or α-particle detection by nuclear reaction[2-7]. In most research of boron analysis α–particles are measured in vacuum condition through the nuclear reaction of ^{11}B (p, α) ^8Be because of its larger cross section than γ-ray emission. However we have tried to detect γ-ray from ^{10}B (p, α'γ) ^7Be nuclear reaction, because in-air measurements will be required for BNCT samples.

2. Experimental

A proton microbeam from 3MV single ended electrostatic accelerator of TIARA facility, Advanced Radiation Technology Center[8] was used for microanalysis of trace amount of boron. The mapping techniques of trace amount of boron (several tens ppm) distribution by detecting γ-ray emitted from ^{10}B (p, α'γ) ^7Be or α-particle from ^{11}B (p, α) ^8Be nuclear reaction have been developed.

In this study the in-air microanalysis system has been used for simultaneous γ-ray and X-ray measurements. The measurement system is described briefly. A schematic view of the external beam apparatus for micro-PIGE and -PIXE is shown in Fig.1. An hp - Ge γ-ray detector (Ortec 1601-1231- S-2), which has $100 cm^3$ crystal volume, is remodeled by Raytech Corporation. The end cap of the detector is converted to L-shape to set the detector crystal just behind the sample this time. The resolution of this detector is 1.7 keV at 1.33MeV with a cooled FET pre-amplifier. A Si(Li) detector is also installed for micro-PIXE analysis of heavier elements. The simultaneous measurements of X-ray and γ-ray can be performed in this study. For α-particle measurements, an annular type SSD detector will be installed in just front of sample inside the
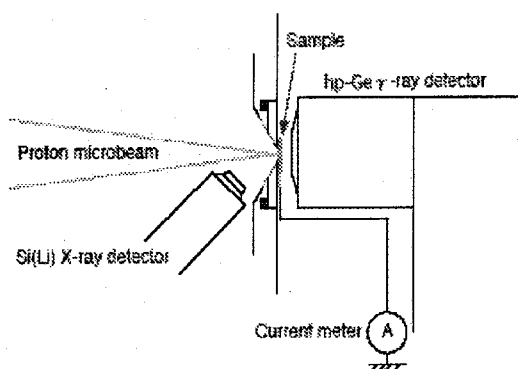
Fig.1 Schematic view of experimental setup for measurements of micro-PIGE and PIXE.

chamber. As this setting disturbs X-ray measurement, simultaneous measurements of light and heavy elements will become impossible. Steel sample is attached on each annular disk sample holder made by acrylic resin which has a tapered hole with a 1mm diameter on the atmospheric side. Up to six holders can be mounted on the revolving stage. The vacuum of the chamber in front of a sample was kept to be $\sim 1 \times 10^{-3}$ Pa. Beam currents from the sample were monitored in experiments.

A typical current of several pA at the beam diameter of about 1μm was used for mapping area of 20 μm x 20 μm. The overall resolution of the proton beam can be kept nearly 1μm.

3. Results and discussion

Several types of steel specimens containing boron were prepared for microanalysis, which is described in Table 1. These steel samples divided in two categories. B type samples contain trace amounts of C, Si, Mn, P, S N and B and A type samples contain these

trace elements and rather rich amounts of Cr, W, Co, V. The samples containing the same boron concentration in two categories could not be prepared this time. So steel specimens containing 100 ppm (A1), 50 ppm (A2), 40 ppm (B1), 20 ppm (B2) boron have been bombarded by 1.7 MeV proton microbeam for γ-ray detection and compared to the appearance of boron distribution. X-rays from the same samples were also measured simultaneously for heavier elemental analysis.

Observed typical γ-ray spectrum is shown in Fig.2. Broad γ-ray spectrum located at 428keV was emitted from ^{10}B (p, α'γ) ^{7}Be reaction. The steel sample containing 100 ppm boron was bombarded by 1.7 MeV proton microbeam (~ 1.5 μm x 3 μm) with the beam currents of ~ 1.6 nA for 2 hours.

If steel contains sodium and magnesium, the intense 440 keV γ-rays appear and also manganese appears at 411.5keV with the intense peak[9]. These lines affect the boron line
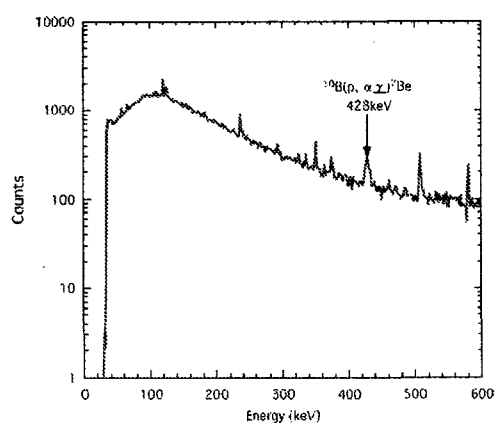
Fig.2 Typical γ-ray spectrum emitted from an iron sample containing 100 ppm boron bombarded by 1.7 MeV proton microbeam.

Table 1 Ingredients in weight % in steel specimens used for microanalysis of boron

	C	Si	Mn	P	S	Cr	W	Co	V	N	B
A1	0.10	≦0.01	≦0.01	≦0.003	≦0.003	9.0	3.0	3.0	0.20	0.06	0.0100
A2	0.10	≦0.01	≦0.01	≦0.003	≦0.003	9.0	3.0	3.0	0.20	0.06	0.0050
B1	0.05	0.25	3.00	≦0.005	≦0.003	—	—	—	—	0.0020	0.0040
B2	0.05	0.25	3.00	≦0.005	≦0.003	—	—	—	—	0.0020	0.0020

as contaminants sometimes. These contaminants in steel sample can be also detected by PIXE measurement, which is simultaneously registered as well as PIGE measurement. These contaminants could not be observed in any steel sample except manganese.

The image of boron is obtained by gating to 428 keV γ-ray signals and typical image of boron is shown in Fig.3. This figure is obtained from the A2 sample in table 1. This steel sample contains 50 ppm boron and heavier metal elements. Scan area is 200 μm x 200μm mapped by using ~1.5 μm x 3.0 μm proton beam (left hand side) and 50 μm x 50 μm scanned by ~1μmφ beam (right hand side).

In Fig.3 many blocks of boron are observed. These blocks are produced by segregation of boron atoms doped in steel materials. This segregation is said to be appeared along with iron grain boundaries. Sizes of these blocks are from several μm to 10 μm in diameter. In this study, any grains cannot be imaged, therefore, the locations of these blocks cannot be determined. As intensities of γ-rays also does not calibrate to the absolute value of boron density, the concentration of boron in a block does not clear. The segregation of boron can be seen in A1 and A2 samples which contain heavy elements, Cr, W, Co and V, on the other hand B1 and B2 samples show uniform distribution. We can conject that heavier elements of Cr, W, Co and V affect the process of segregation of boron.

X-rays from steel sample were also
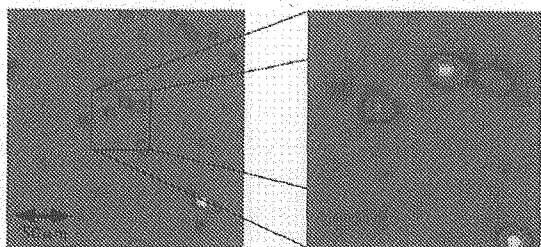
Fig.3 Typical γ-ray imaging of 50 ppm boron contained in an iron specimen.

measured, and lines of ingredients, such as Cr,

W, Co, V, etc. were observed. Images of these elements show uniform distributions.

4. Summary

The imaging technique of trace amount of boron (several tens ppm) by detecting gamma ray emitted from ^{10}B (p, α'γ) ^{7}Be nuclear reaction has been developed by using MeV proton microbeams irradiation system of TIARA single-ended accelerator.

Many blocks of boron are observed in the imaging of γ-ray from boron. These blocks are produced by segregation of boron atoms doped in steel materials. Sizes of these blocks are from several μm to 10 μm in diameter. This segregation is observed only for steel containing heavy elements, such as Cr, W, Co and V.

In PIXE measurement only uniform distribution could be observed.

Acknoledgements

References

1) T.Sakai, T.Kamiya, M.Oikawa, T.Sato, A.Tanaka, K.Ishi, Nucl. Instrum. Meth. B 190 (2002) 271.
2) G.Demortier, Nucl. Instrum. Meth. B 104 (1995) 244.
3) K.A.Sjöland, P.Kristiansson, P.Tallone, Nucl. Instrum. Meth. B 104 (1995) 255.
4) W.J.Trompetter, A.G.Reyes, I.C.Vickridge, A.Markwitz, Nucl. Instrum. Meth. B158 (1999) 568.
5) P.Krisriansson, U.Halenius, H.Skogby, M.Elfman, K.Malmqvist, J.Pallon, Nucl. Instrum. Meth. B 158 (1999) 562.
6) P.Berger, E.Tominetz, C.Godart, E.Allno, L.Daudun, and J.-P.Gallien, J. Solid State Chem. 154 (2000) 301.
7) J.Liu, X.Lu, X.Wang, W.Chu, Nucl. Instrum. Meth. B 190 (2002) 107.
8) T.Kamiya, T.Suda and R.Tanaka, Nucl. Instrum. Meth. B 104 (1995) 43.
9) C.Oliver, H.A.Ras, M.Peisach, J. Radioanal. Chem. 70 (1982) 311.

7.6 Measurement of Thickness of Samples by STIM for PIXE Analysis

T. Satoh, T. Sakai and M. Oikawa

Advanced Radiation Technology Center, JAERI

1. Introduction

An in-air micro-PIXE (Particle Induced X-ray Emission) analysis system was developed by Japan Atomic Energy Research Institute in 2000[1]. Two dimensional distributions of some trace elements in a single biological cell were successfully measured with spatial resolution of $1\mu m$. However, the X-ray yields are not uniform due to X-ray production cross sections and linear attenuation coefficients when thick samples are analyzed with the micro-PIXE system. To compensate the reduction of X-ray yields, thickness of a sample must be taken accurately with spatial resolution of a few microns but it is difficult to measure them by micro-PIXE analysis. Therefore, we use STIM (Scanning Transmission Ion Microscopy)[2]. Furthermore, we developed a computer software code to correct the X-ray yields. An actual shape of a sample is calculated from STIM data in the program. By using the calculated shape and experimental conditions such as an angle of detector, change of X-ray production cross sections accompanied by decrease of incident particle's energy and attenuation of X-rays in the sample can be simulated. As a result, correction values of X-ray yields can be estimated. To confirm validity of our method, ion exchange resins, which are similar to biological cells in size, were used as a test sample.

2. Calculation of detected intensities of X-rays

Figure 1 shows the method of calculation on detected intensity of X-rays. E_0, the initial energy of proton microbeam, is 3 MeV. The energy decreases to E_1 (2.86 MeV) after the projectile passes through a $5\mu m$ thick polycarbonate film, which supports samples.

Ion beams Detected yield of x-rays

X, Y $E_0 = 3 MeV$ $I_1 = I_0 \exp[-(\mu_{sample} l_0 + \mu_{polycarbonate} l_1)]$

Z l_1: Path length in support film of polycarbonate

$E_1 = 2.86 MeV$

l_0: Path length in a sample

Intensity of characteristic x-rays

$I_0(x, y, z) \approx const \cdot E^4$

$E = E_1 - \int \frac{dE}{dz}(x, y, z)dz$
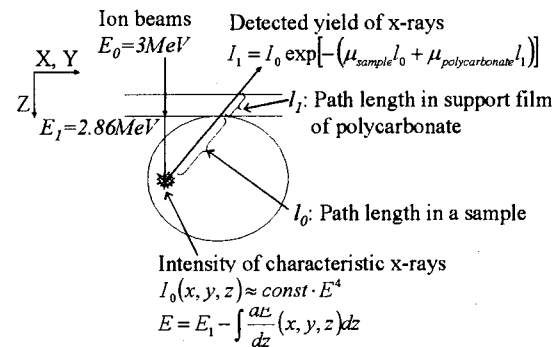
Correction coefficient$(x, y) = \int_{z_{min}}^{z_{max}} I_1 dz$

Fig. 1 Schematic diagram of calculation.

Since I_0, the fluorescence intensity of a characteristic X-ray, is in proportion to the fourth power of the projectile's energy, I_0 is expressed by,

$$I_0(x, y, z) \approx const \cdot E^4 \qquad (1)$$

where E is the projectile energy in a sample. It is given by

$$E(x, y, z) = E_1 - \int_{z_{min}}^{z} \frac{dE}{dz}(x, y, z')dz' . \qquad (2)$$

The X-rays are gradually attenuated while passing through the sample. Detected intensity of X-rays is expressed

as follows;

$$I_1 = I_0 \exp[-(\mu_{sample}l_0 + \mu_{polycarbonate}l_1)], \quad (3)$$

where μ_{sample} and $\mu_{polycarbonate}$ are the linear attenuation coefficients of the sample and the polycarbonate film, respectively. l_0 and l_1 are the path length in the sample and the film, respectively. After all, the correction coefficient of X-ray yields is expressed by

$$C(x,y) = \int_{z_{min}}^{z_{max}} I_1 dz. \quad (4)$$

Those calculations are done in every position, and measured intensity of the X-ray is normalized by the coefficient as follows;

$$N_c(x,y) = N_m(x,y)/C(x,y), \quad (5)$$

where N_m and N_c are measured and corrected counts of the X-rays, respectively.

3. Experiment

A schematic diagram of our experimental apparatuses is shown in Fig. 2.
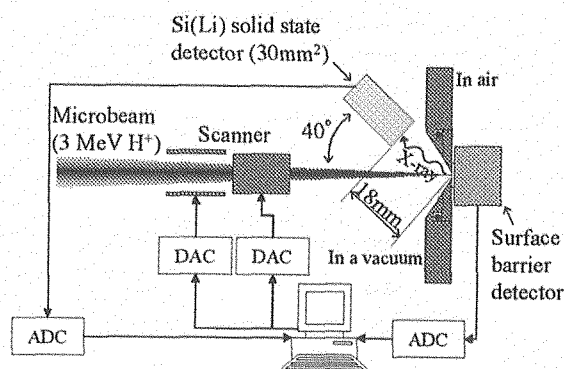
Fig. 2 Experimental setup for micro-PIXE and STIM.

The beam scanners, which are controlled by a personal computer through DACs (Digital-to-Analog Converter), deflect 3MeV proton microbeams. For STIM, a surface barrier detector is placed on the back of a sample. In the case of micro-PIXE, a faraday cup is set instead of the detector. The distance and the angle of Si(Li) X-ray detector are 18 mm and 40°, respectively. Energy values measured by those detectors are recorded in the personal computer through ADCs (Analog-to-Digital Converter) with information about irradiated position.

Figure 3 is photograph of the ion exchange resins through a microscope.
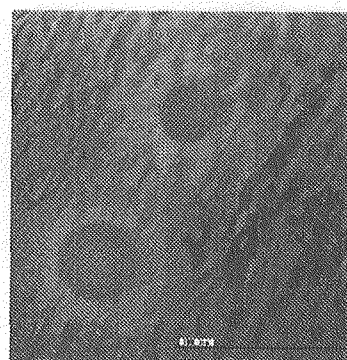
Fig. 3 Optical microscope image of grains of ion exchange resin. The main component is polystyrene. The grain diameter is from 30μm to 50μm.

4. Results and Discussion

The thickness of the sample can be estimated at each position by STIM as in Fig. 4. The shape of the sample was assumed in a computer from the results. The energy of projectile and the attenuation of X-rays at every position in the sample was simulated with the computer by using Eqs. (1), (2), (3) and (4). We used the linear attenuation coefficients from Ref. 3 in the

simulation.
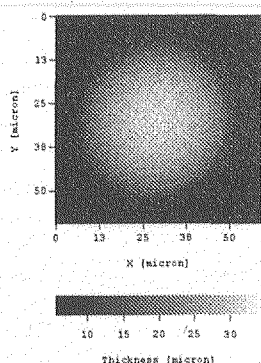
Fig. 4 The thickness of a grain of ion exchange resin estimated from the data of STIM.
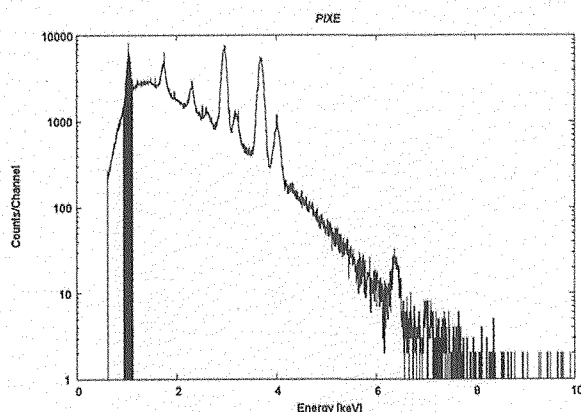
Fig. 5 PIXE spectrum induced by 3.0 MeV protons from the ion exchange resin. The peak painted black is Kα X-ray of sodium.

The PIXE spectrum of the ion exchange resin is shown in Fig. 5. The peak painted black in Fig. 5 is Kα X-ray of sodium. From the data corresponding to the peak, the distribution of sodium can be obtained as in Fig. 6. The left picture shows a result without correction of X-ray attenuation. There seems to be a low yield of characteristic X-rays at the left side of the resin because of self-absorption. By normalization of Eq. (5), the outline of the sample became

clear as in the right picture. That correction took about 2 days on PC (Intel Celeron CPU 2.80GHz).
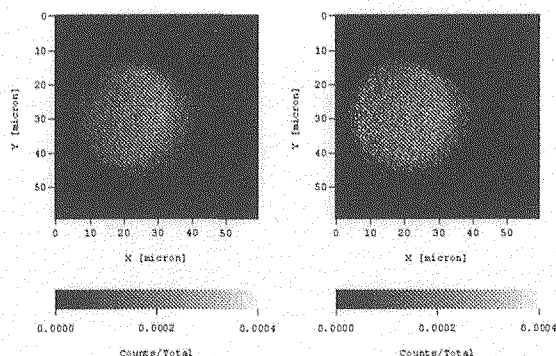
Fig. 6 Distribution of sodium obtained by using micro-PIXE system. The right picture is a corrected result from the left one.

5. Conclusion

The correction method and simulation code of X-ray attenuation in a sample whose thickness is not uniform was developed. We confirmed its validity through experiments by using the ion exchange resin as a test sample. Since this computer program code is very slow, optimization corresponding to the shape of a sample is necessary.

Acknowledgement

References

1) T. Sakai, T. Kamiya, M. Oikawa, T. Sato, A. Tanaka, K. Ishii, Int. J. PIXE Vol. 10 Nos. 3 & 4 (2000) 91.

2) J.C. Overley, R.M.S. Schofield, J.D. Macdonald, H.W. Lefevre, Nucl. Instr. and Meth. B30 (1988) 337.

3) B.L. Henke, P. Lee, T.J. Tanaka, R.L. Shimabukuro, B.L. Fujikawa, Atomic Data and Nuclear Data Tables 27 (1982) 1.

7.7 Transient Current Induced in Silicon Carbide Diode by Oxygen Ion Microbeams

T. Ohshima*, T. Satoh**, M. Oikawa**, S. Onoda*, T. Hirao* and H. Itoh*

Department of Material Development, JAERI*

Advanced Radiation Technology Center, JAERI**

1. Introduction

Silicon carbide (SiC) is regarded as a strong candidate for high-power and high-frequency devices because of its excellent physical and thermal properties[1,2]. In addition, since SiC shows high radiation resistance[3], particle detectors used in severe radiation environments are thought to be one of the interesting applications. For the development of particle detectors, the evaluation of charge generated in detectors by particle irradiation is very important. In previous studies[4, 5], the charge collected in SiC detectors was evaluated with ion beam induced charge (IBIC) using alpha particles. It was reported from IBIC measurements using alpha particles that 4H-SiC Schottky diodes showed a charge collection efficiency (CCE) of 100%, and the efficiency did not decrease after gamma-ray irradiation at 0.40 MGy[5]. These results imply high radiation resistance of SiC detectors.

For applying SiC to particle detectors, it is also necessary to study the CCE using wide variety of particles. However, in almost all previous studies for developing SiC detectors, the CCE of SiC diodes was evaluated using alpha particles. Only a few studies were reported on charge generated in SiC diodes by heavy ion irradiation[6]. Besides, the degradation of the CCE in IBIC measurements should be considered because severe radiation damage was introduced in the samples by irradiation of a number of incident ions during the measurements[7]. Single-ion hit Transient Ion Beam Induced Current (TIBIC) is a very useful tool for measuring ion induced current in diodes with minimizing the influence of damage.

In this study, we measured current generated in SiC n$^+$p diodes by oxygen ion irradiation using the TIBIC technique and evaluated the CCE.

2. Experimental procedures

The n$^+$p diodes used in this study were fabricated on p-type 6H-SiC epitaxial layers (10 μm thick) grown on p-type 6H-SiC substrates (3.5° off, Si-face, Cree inc.). The net acceptor concentration of the epitaxial layers was 3.5×10^{15} /cm^3. Three-fold implantation (60, 90, 140 keV) of phosphorus ions at 800 °C and subsequent annealing at 1650 °C for 3 min in argon (Ar) were performed to form n$^+$ region. The aluminum (Al) electrodes (25 nm thick) were formed using lift-off technique on the n$^+$ region. For backside, Al electrodes onto p-type substrates were sintered at 850 °C for 5 min in Ar, and Al with a thickness of 70 nm was re-evaporated onto the sintered areas. The diodes were irradiated with 15 MeV-oxygen (O^{4+}) microbeams under applied biases up to 150V, and transient current generated by irradiation of 15 MeV-O^{4+} was measured using the TIBIC collection system. In the TIBIC collection system, a single event triggering system in combination with a fast switch beam shutter system was installed. The transient current
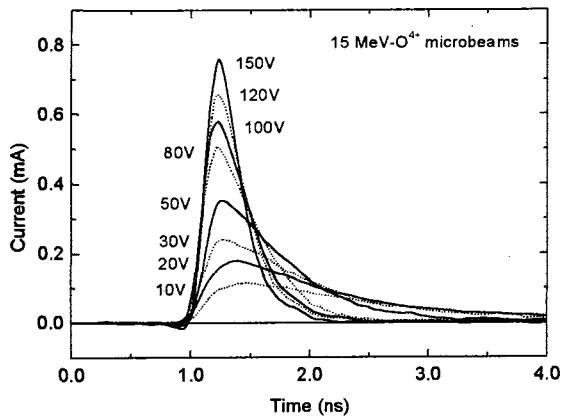
Fig. 1 Transient current for n^+p SiC diodes irradiated with a 15MeV-O^{4+} microbeam. The values of the applied reverse bias are described in the figure.

Fig. 2 charge collected by n^+p 6H-SiC diodes irradiated with 15 MeV-O^{4+} microbeams as a function of applied reverse biases.

signals were measured using a 3 GHz Tektronix TDS694C oscilloscope, and the data were collected in real time. Details of the TIBIC collection system are described in ref. 8.

3. Results and Discussion

Figure 1 shows the transient current observed for the n^+p SiC diodes. The values of applied reverse bias are represented in the figure. The peak current of the transient signal increases with increasing applied bias. The fall-time, which is defined as the time from 90 % to 10 % of the transient current peak, becomes shorter with increasing applied reverse bias. These results can be interpreted by the fact that the electric field increases and the depletion layer becomes longer with increasing applied bias.

Figure 2 shows charge collected in the n^+p 6H-SiC diodes irradiated with 15 MeV-O^{4+} microbeams as a function of applied reverse biases. The values of collected charge are obtained by the integration of current transient signals. The values normalized by the result obtained at reverse bias of 150V are plotted in the

figure. The estimated values of charge generated in the depletion layer are also depicted as broken line in the figure. In the estimation, ionizing energies deposited from 15 MeV-O^{4+} into SiC are calculated by Monte Carlo simulation code SRIM2003[9]. The energy for the generation of an electron-hole (e-h) pair in 6H-SiC is assumed to be 7.8 eV (= 2.8E_g), which is an empirical formula, because the value of the energy for 6H-SiC has not yet been determined. The collected charge increases with increasing applied reverse bias up to 90 V, and the saturation of the collected charge is observed at applied biases above 100 V. As for the comparison between the collected charge experimentally obtained in this study and that estimated using ionizing energy deposited in the depletion layer, the experimentally obtained value is larger than that derived theoretically at biases below 110 V. It indicates that large amounts of charge generated in deeper region than the depletion layer are collected although no electric field is built in such a deeper region. This behavior cannot be attributed to the contribution of a diffusion component. Similar results were reported for GaAs

diodes irradiated with 15MeV-O^{4+} microbeams[10]. The transient extension of the electric field from the depletion region occurs by the generation of high dense e-h pairs due to the introduction of swift heavy ions, and as a result, charge can be collected by the extended electric field ("funneling effect")[11, 12]. Therefore, the result obtained at biases below 110V can be interpreted in terms of the contribution of the funneling effect. On the other hand, at biases above 120 V, charge observed in this study is the same as the value estimated using ionizing energy in the depletion layer. Since at a bias of 120V the depletion layer length becomes comparable to the ion range of 15 MeV-O^{4+}, almost all charge generated by 15 MeV-O^{4+} is collected by an electric field in the depletion layer of the n^+p SiC diode, and thus, the CCE is considered almost 100 %.

4. Summary

The transient current generated in the n^+p SiC diodes by irradiation of 15 MeV O^{4+} microbeams was measured using the TIBIC collection system. With increasing applied reverse bias, the signal peak of the transient current increases and the fall-time decreases. The charge collected by the n^+p SiC diodes was evaluated from the integration of TIBIC signals. The value of collected charge increases with increasing applied reverse bias up to 90 V, and the saturation of the collected charge is observed at reverse biases above 100 V. At reverse biases below 110 V, the charge generated in deeper region than the depletion layer is collected by the n^+p SiC diodes due to the funneling effect. Almost all charge generated in SiC by 15 MeV-O^{4+} irradiation is collected by the n^+p SiC diodes at biases above 100 V.

References

1) *"Properties of Silicon Carbide"* Edited by G. L. Harris, EMIS Datareviews Series No. 13, an INSPEC publication, the Institution of Electrical Engineers, London, United Kingdom (1995).

2) H. Daimon, M. Yamanaka, M. Shibahara, E. Sakuma, S. Misawa, K. Endo and S. Yoshida: Appl. Phys. Lett. **51**, 2106 (1987).

3) T. Ohshima, M. Yoshikawa, H. Itoh, Y. Aoki, I. Nashiyama, Mater. Sci. & Engineer. B **61-62** (1999) 480.

4) W. Cunningham, A. Gouldwell, G. Lamb, J. Scott, K. Mathieson, P. Roy, R. Bates, P. Thornton, K. M. Smith, R. Cusco, M. Glaser, M. Rahman, Nucl. Instr. and Meth. A **487** (2002) 33.

5) F. Nava, E. Vittone, P. Vanni, G. Verzellesi, P. G. Fuochi, C. Lanzieri, M. Glaser, Nucl. Instr. and Meth. A **505** (2003) 645.

6) For example, T. Ohshima, K. K. Lee, S. Onoda, T. Kamiya, M. Oikawa, J. S. Laird, T. Hirao, H. Itoh, Nucl. Instr. and Meth. B **206** (2003) 979.

7) T. Hirao, I. Nashiyama, T. Kamiya, T. Nishijima, Nucl. Instr. and Meth. B **104** (1995) 508.

8) J. S. Laird, T. Hirao, H. Mori, S. Onoda, T. Kamiya, H. Itoh, Nucl. Instr. and Meth. B **181** (2001) 87.

9) J. F. Ziegler, *Handbook of Ion Implantation Technology*, Elssevier Science Publishers B.V., The Netherland (1992) pp.1-68.

10) T. Hirao, H. Itoh, S. Okada, I. Nashiyama, Rad. Phys. and Chemi. **60** (2001) 269.

11) G. C. Messenger, IEEE Trans. Nucl. Sci. NS-29 (1982) 2024.

12) H. L. Grubin, IEEE Trans. Nucl. Sci. NS-31 (1984) 1161.

JP0650261

7.8 Time Dependence on Fluorine Distribution in the Tooth

H. Yamamoto*, M. Nomachi**, K. Yasuda***, Y. Iwami*, S. Ebisu*,
H. Komatsu****, Y. Sugaya**, T. Sakai*****, M. Oikawa*****,
T. Satoh***** and M. Fukuda*****
Graduate school of Dentistry, Osaka University*,
Graduate school of Science, Osaka University**,
Wakasa wan Energy Research Center***,
Graduate school of Dentistry, Hokkaido University****
Advanced Radiation Technology Center, JAERI*****

1. Introduction

For the quantitative evaluation of cariostatic property of fluorine (F), it is important to study the fluorine (F) penetration into the tooth at the condition of F containing atmosphere. We have reported previously the penetration of F at the several conditions using PIGE method which we have developed at TIARA.[1,2] In those studies, we have reported the dependence of penetration aspect on the kind or the mechanism of F-releasing materials. The clinical treatment also induced the different aspect of F penetration mode[3-5].

In this study, we report the time dependence on the F distribution in the human tooth, using the PIGE method.

2. Experimental procedure

2. 1 Experimental set-up

The experimental facility of the 1.7 MeV proton beam accelerated by the TIARA single-ended accelerator at JAERI-Takasaki, was used for this work. Precise conditions of the measurement were already reported in the previous paper [1,2].

2.2 Specimens

Human teeth, extracted for the reason of the periodontitis and orthodontics at the Osaka University dental hospital in the six months, were used as the specimens. The crown of the tooth was cut perpendicular to the axis of the tooth with 2mm in width. Four kinds of dental materials were used as the source of F-releasing material (Beautifil; SHOFU, Unifil S; GC, F2000; 3M, Clearseal F;Kuraray). The disk (φ10mm×2mm) of each material was prepared. The plane surface of the disk was attached to the cut surface of the tooth with the wax. Whole surface of the tooth and attached materials was covered with varnish except

the window of 3mm in width at the side. The specimens were immersed in the physiological saline solution at 37 ℃. After one month (1M) and six months (6M) of the immersion, the specimens were cut perpendicular to the interface of tooth and material. The concentration of F and Calcium (Ca) on the cut surface was measured.

The precise pre-treatment of the specimens for the measurement was the same as previous experiments and precisely described in the previous reports [1,2].

2.3 Measurement

The size of measurement areas were about 140 μm x 280μm. F and Ca concentration around the interface was measured. The obtained raw data were calibrated by the reference materials $Ca_{10}(PO_4)_6(OH)_{2-2x}F_{2x}$ (x=0, 0.1, 0.5, 1.0). The maximum value of the F concentration penetrated into the tooth and the depth of F penetration were compared among the materials.

For the estimation of values, the Kruskal-Wallis test was used.

3. Results and Discussion

Figure 1 (A)-(D) shows the parts of obtained results as the 2D mapping form. In all specimens, the F penetration into the tooth was observed both after 1M and 6M. Fig2 (A)-(D) shows the maximum values of the F concentration penetrated into the tooth and the depth of F penetration in each material. In the tooth with material "Beautiful", the significant difference in the F concentration and depth between 1M and 6M was both observed. In the tooth with the material "F2000", the significant difference in the depth between 1M and 6M was recognized. In the tooth with the material "Clearseal

F" which showed no significant difference between 1M and 6M, the penetration depth after 1M was significantly larger than the other materials, but the maximum
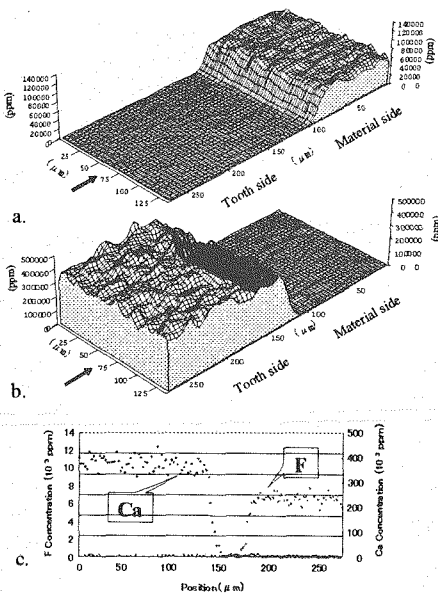
A. Distribution of F and Ca in the tooth with Beautifil after 1M
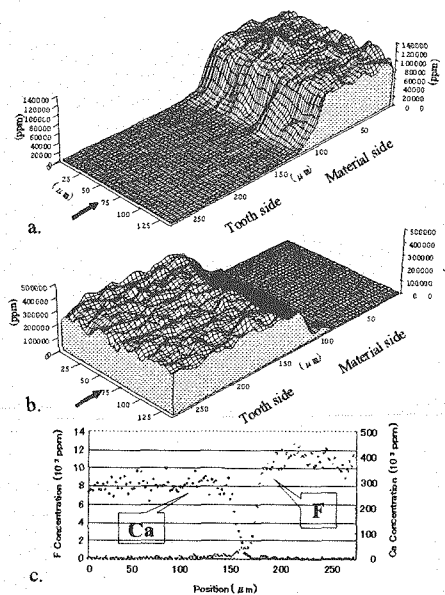
B. Distribution of F and Ca in the tooth with Beautifil after 6M
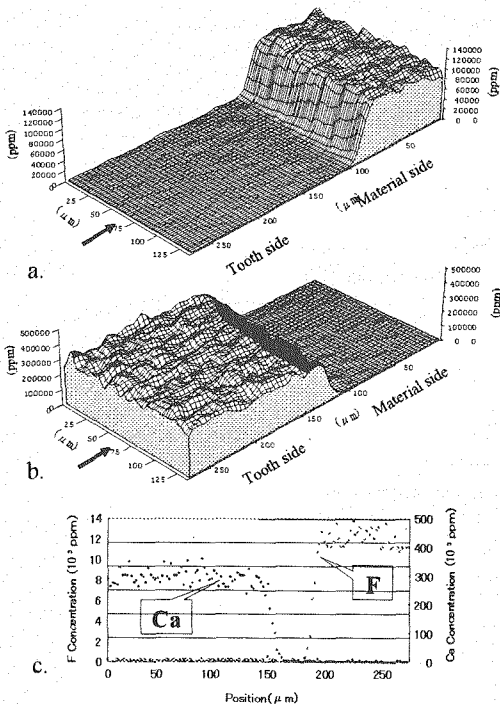
C. Distribution of F and Ca in the tooth with F2000 after 1M
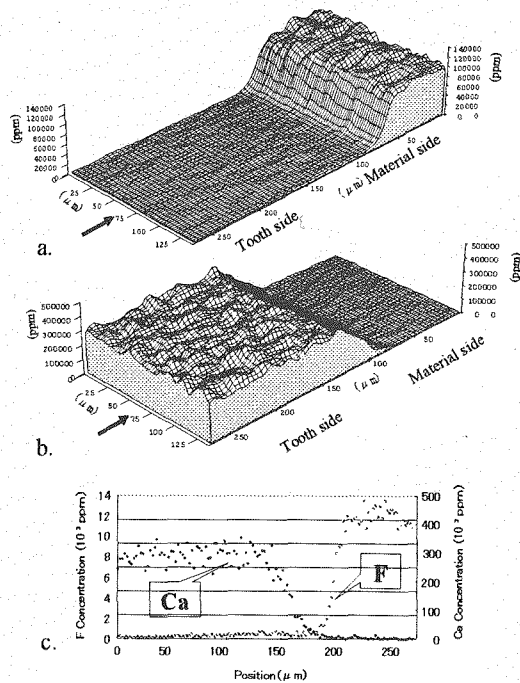
D. Distribution of F and Ca in the tooth with F2000 after 6M

Fig.1 F and Ca concentration around the interface of material and tooth after 1M(A,C) and 6M (B,D)
(a) F 2D distribution map.   (b) Ca 2D distribution map.   (c) Concentration of F and Ca at the cut face along the arrow in (a) and (b).
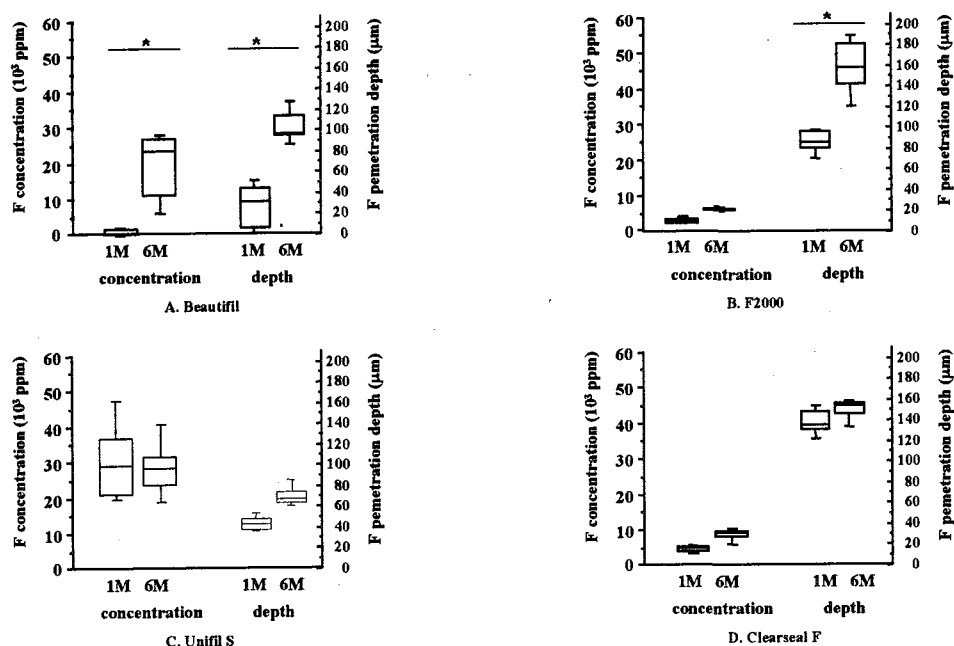
Fig.2 The maximum F concentration penetrated into the tooth and penetrated depth in each material
___*___ ; shows significant difference (p<0.05).
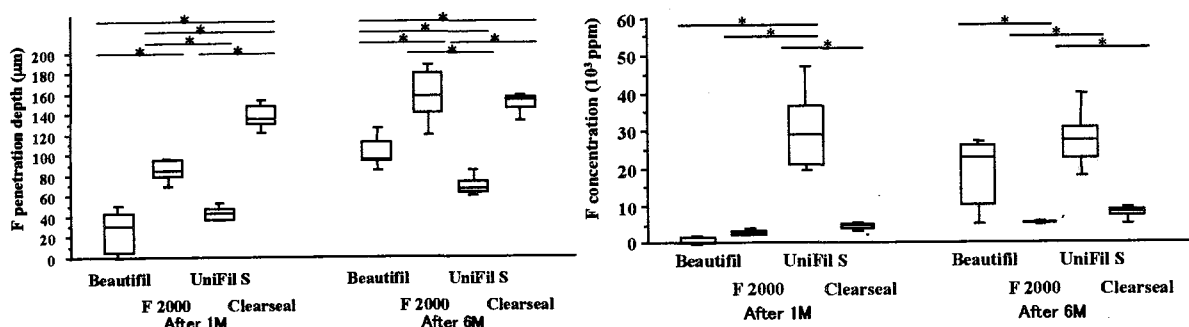
Fig3 F penetration depth into the tooth
___*___ ; shows significant difference (p<0.05).

Fig4 Maximum F concentration penetrated into the tooth
___*___ ; shows significant difference (p<0.05).

concentration was low. In the tooth with the material "Unifil S" which showed also no time dependence, the maximum concentration both after 1M and 6M was significantly higher than the other materials, but the penetration depth was shallow (Fig.3,4).

The time dependence of the F maximum concentration penetrated into the tooth and the penetration depth showed the characteristic behavior of each F-releasing materials. It is necessary to investigate how to affect the type of distribution on the prevention for the caries.

4. Acknowledgements
We would like to thank members of

TIARA, JAERI TAKASAKI for operating the accelerator facility.

References
1) M. Nomachi et al., TIARA Ann. Rep. 2000, AERI-Review 2001-039 (2001) 244-246.
2) T. Sakai et al., Nucl. Instr. And Meth. B190 (2002) 271-275.
3) H.Yamamoto et al., Nucl. Instr. and Meth. B210 (2003) 388-394.
4) H.Yamamoto et al., TIARA Ann. Rep. 2000, AERI-Review 2004-025 (2004) 267-269.
5) H.Yamamoto et al., Nucle Instr and Meth B231 (2005), 300-307

JP0650262

7.9 Intracellular Changes of Zinc and Bromine by Interferon and Zinc

T. Nagamine*, T. Kusakabe*, H.Takada*,K. Nakazato*, H.D. Moon*,
T. Satoh**, M. Oikawa**, T. Sakai** and K. Arakawa**
School of health Science, Gunma University *
Advanced Radiation Technology Center, JAERI**

1. Introduction

Our studies indicated the usefulness of combination therapy with interferon (IFN) and zinc (Zn) for chronic hepatitis C[1), 2)]. We postulate that the zinc induced by IFN will combine with metallothionein (MT), move to intranuclear, and be used for synthesis of zinc-finger protein or NF-κB[3),4)]. By epidermal growth factor or insulin stimulus, MT moves to intranuclear from cytoplasm. However, shift of MT is not achieved by tumor necrotic factor, and the effect of IFN on translation of MT remains largely unknown.

By focusing the beam spot within 1 μm (micro-beam) and scanning the samples, the elemental distributions in the sample are observed. In-air micro-PIXE is a convenient and useful apparatus for examining metabolic mechanism in the organ tissues and cell cultures[5)]. Using in-air micro PIXE, we investigate the influence of zinc concentration on the intracellular induction of zinc by IFN and the transportation of zinc from cytoplasm to a nuclear.

2. Experimental procedure

2.1 Cell culture

Human hepatocellular carcinoma cell line (HepG2 cell) was cultured with DMEM medium added 10%FBS, which contains Cu 2μg/dl, Zn 16μg/dl and Fe 13μg/dl, under 5%CO_2 air at 37 °C.

2.2 Preparation of sample for in-air micro PIXE analysis

HepG2 cells adjusted 5×10^5 cells/ml were incubated using Mayler membrane over night. Medium was replaced with 1ml of medium which contained 100μM of BrdU, and incubated for 24 h. Then the medium was exchanged with IFN and Zn-contained medium as follow; IFN 0+Zn100μM, IFN25IU+Zn100μM, IFN100IU+Zn100μM, IFN100IU+Zn0, IFN0+Zn0(Control). Six h later, the cells were rinsed seven times with TAM solution and fixed on the plastic holder. Finally the cells were cryofixed instantaneously with liquid nitrogen and dried in a vacuum.

The 2.6 MeV proton beam, 1 μm of beam spot size, accelerated by the TIARA single-ended accelerator at JAERI-Takasaki was used for intracellular elemental distribution in the cell samples. Precise conditions of measurement were reported previously[5)]. Net count of each element was calculated by PC soft ware program. As Sulfur(S) value is representative of the whole cell counts, the ratio of Zn to S value was evaluated.

3 Results and discussion

1) Intracellular induction of Zn by IFN according to zinc concentration (Table)

Intracellular Zn value is similar between the IFN 100 IU sample and the control, and

the Zn 100μM samples shows higher Zn value than the control or IFN alone. Comparison among the IFN + Zn samples, the intracellular Zn value reaches peak at IFN 25 IU/mL, then decreased at IFN 100 IU/mL.

Table : Intracellular Zn value

IFN(IU)	Zn(μM)	Zn/S(%)
0	0	3.1
0	100	4.8
100	0	2.3
25	100	34.5
100	100	5.4

2) Relationship between Zn and bromine

In the control cells, Zn was distributed diffusely in the cytoplasm and nucleus. The accumulation of bromine (Br) into nucleus was thinly shown, and Br map consisted partially with the Zn (Fig. 1(a), Fig. 2, Fig. 4(a))

Increased intensity of Zn was observed in the Zn-added cells, and the accumulation of Br into nucleus was unchanged.

Zn image became faintly in the 100 IU of IFN-treated cells. Br was obviously accumulated in the nuclei.

In the IFN100+Zn100μM-treated cells, Zn was thickly distributed and the number of Br-positive nucleus was increased (Fig. 1(b), Fig. 3). Br map showed good consistency with the distribution of Zn, and the accumulation of Zn into the Br-positive nucleus was also observed (Fig. 4(b)).

In IFN25IU+Zn100uμM cell, Zn was mainly localized in the nuclei.

(a)   (b)
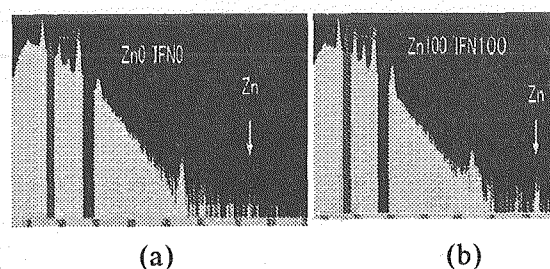
Fig. 1 In air micro-PIXE spectrum obtained from HepG2 cell
(a) Zn 0 μM + IFN 0 IU/ml (control)
(b) Zn 100 μM + IFN 100 IU/ml

Br   Zn   P
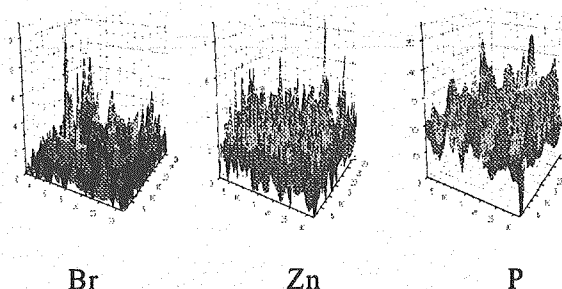
Fig. 2 Three dimensions elemental map of HepG2 cells; Control .
Scanning area:135×135μm ^{2}

Br   Zn   P
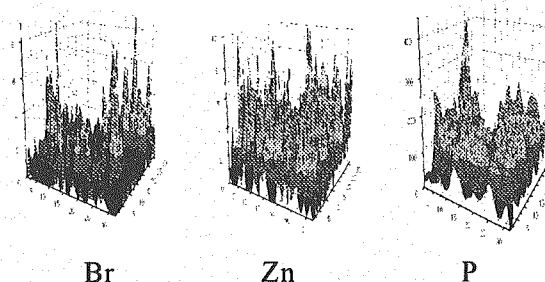
Fig. 3 Three dimensions elemental map of HepG2 cells treated with IFN100U/mL+ Zn100μM
Scanning area:135×135μm ^{2}

4.Conclusion

1. In zinc deficiency, Zn is not translated into the liver cells by IFN.

2. Zn is translated from Zn-sufficient medium into liver cells by IFN; which peak at 25 IU of IFN.

3. By concomitance with IFN and Zn, Br-positive nucleus is increased and Zn is tended to accumulate into the Br-positive ones.

(a)   (b)
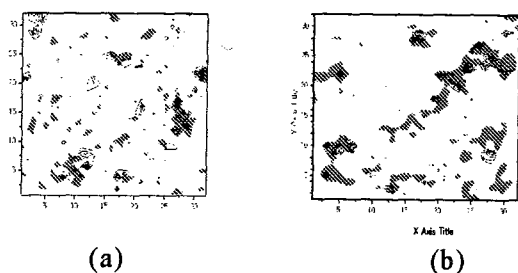
Fig. 4   Correlation of Zn map to Br map.
   (a) In control , counter plot of Br was
   partially   fitted with Zn map.
   (b) In HepG2   cells treated with
   IFN100U/mL +   Zn100μM, counter
   plot of Br   was   showed   good
   consistency with Zn map.

References

1) T,Nagamine , H.Takagi, H. Takayama, et
   al. Trace Element Res 75 (2000) 53-63

2) T,Nagamine, K.Suzuki, H.Kondo, et al
   Canadian J Gastroenterology (in press)

3) M.Sato, J.Yamaki, T.Oguro, et al.
   Tohoku J Exp med 178 (1996) 241-250.

4) A Sakurai, S.Hara, N.Okano, et al. FEBS
   Lett 455 (1999) 55-58

5) T.Sakai, T.Kamiya, M.Oikawa, et al.Nucl
   Instr Meth B190 (2002) 271

JP0650263

7.10 Analysis of Intracellular Distribution of Boron and Gadolinium in 9L Sarcoma Cells using a Single-ended Accelerator (Micro PIXE)

K. Endo*, K. Nakai*, T. Yamamoto*, Y. Shibata*, A. Matsumura*,

K. Ishii**, T. Sakai***, T. Satoh***, M. Oikawa***, Y. Ohara***,

H. Kumada**** and K. Yamamoto****

Department of Neurosurgery, Institute of clinical medicine, University of Tsukuba*

Department of Engineering, University of Tohoku**

Advanced Radiation Technology Center, JAERI***

Department of Research Reactor, JAERI****

1. Introduction

As the therapy for the patients with malignant brain tumor, we neurosurgeon usually first excise as much of the tumor mass as possible and then prepare the patient for radiation therapy and / or chemotherapy to eliminate tumor cells that might remain diffusely distributed in normal brain tissue. This therapeutic strategy has not brought complete cure so far, thus we have been investigating usefulness of Boron Neutron Capture Therapy (BNCT). And we have been investigating effectiveness of Boron and gadolinium (Gd) as elements to capture neutrons. The objective of this study was to investigate the movement and distribution of these two elements in the 9L sarcoma cells. We also discuss the possibility of using gadolinium for clinical neutron capture therapy[1),2),3)].

2. Material and methods

9L sarcoma cells were cultured on Mylar film fixed with ring in minimum essential medium (MEM) at 37°C until they form a monolayer. Next we add the Gadobenate dimeglumine (Gd-BOPTA) or sodium borocaptate (BSH) into the culture medium and incubate the cells for 24~72 hours at 37°C. We used the JAERI single-ended accelerator for micro-PIXE (micro Particle-Induced X-ray Emission Spectrometry) to analyze intracellular distribution of Boron and Gd with the technique of multi parameter analyzing system.

3. Results and Discussion

Figure 1 and 2 shows almost same distribution of boron and Gd in cells. This indicated the affinity of tumor cells and these elements. In other words, the possibility to use Gd as neutron-capture supplmentary element was suggested. But we observed the distribution of Boron and Gd around the cells too. This indicated that we could not measure clearly where these elements were there. We do not know whether they adhered on the cell membrane surface or captured inside of the cells. Also, when captured inside the cells,

we thought that it wasn't possible to measure about the existence part in the cells. The reasons are the problem of the sample adjustment or the cell damage in case of irradiation and so on.

We have some plans to analyze movement of Gd using different culture times in vitro and in vivo study using tumor implant model in animals. These experiments to measure element distribution in tumor cells will be useful to understand clinical condition.

In the future, we hope to be able to analyze the intracellular distribution of Boron and Gd more in details, and get information about quantitative measurement of Boron and Gd. Then we hope to apply these two elements as a more effective clinical BNCT.

References

1) Matsumura A, et al., Monduzzi Editore, Bologna, 1073-1078, 2002.

2) Tian Zhang, et al., AJNR 23:15-18, January 2002.

3) Gelsomina De Stasio, et al., CANCER RESEARCH 61, 4272-4277, May 15, 2001
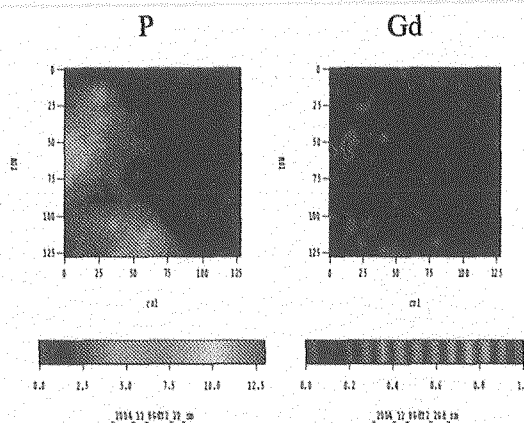
Fig. 1 Distribution of phosphorus, indicating 9L sarcoma cells, and gadolinium.
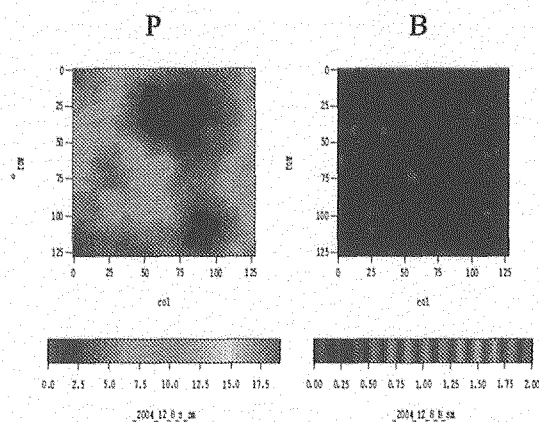
Fig. 2 Distribution of phosphorus, indicating 9L sarcoma cells, and boron.

7.11   Target Chemotherapy by Radiation

S. Harada*, S. Ehara*, K. Ishii **, H. Yamazaki**, S. Matsuyama**,
M. Fukuda***, T. Sakai***, T. Satoh*** and M. Oikawa***
Department of Radiology, Iwate Medical University*
Department of Quantum Science and Engineering, Tohoku University**
Advanced Radiation Technology Center, JAERI ***

1. Introduction

The technical advance of radiotherapy enabled us to optimize the radiation field to the tumor at our will. If the uptake of anticancer medicine is facilitated by radiation, or the capsule that emits its contents (anticancer medicine, radiosensitizer, etc) by radiation is innovated, the optimized radiation field will localize the anticancer medicine to the tumor. In this way, we will be able to target the localization of the anticancer medicine to the tumor by optimizing the radiation field. In biochemistry, it was made evident that the carboplatin[1] (antitumor reagents) is transported from outside to inside of the cell by human transporting protein I (hCTR-1)[1-4], and the hCTR-1 is activated by the low dose irradiation[4]. It is considered that the low dose radiation activates the hCTR-1 and facilitates transport of the carboplatin from outside to inside of the cell, which leads to the increased delivery of carboplatin to the cell. As for the capsules, the alginate is used to make the liquid core capsules and hyaluronic acid is easily decomposed by the irradiation[5]. The mixture of alginate and hyaluronic acid may discomposed by the irradiation. In this study, the target-chemotherapy was tested by the two method: 1) the low dose radiation with carboplatin; and 2) the alginate liquid core capsules.

2. Experimental procedure

2.1 Test for the alteration of carboplatin by low dose irradiation in human leukemic cell

On our before irradiation, 4 μmol of carboplatin was added to the medium, which contained the Human leukemic cell (OCI/M2), and then the radiation was given. Radiation was performed using ^{60}Co γ - ray by a single dose of 0.5 Gy. After 6 hour radiation, cells were harvested by a centrifuge of 1000 rpm/5min. The harvested cells were washed by 0.1 mmol THAM buffer for three times under the centrifuge of 1000 rpm/5min. The 200 μ litter of the suspension of washed cells was dropped onto the mylar film that was cooled by liquid nitrogen through isopentane. The mylar film was freeze-dried at 10^{-4} Torr for 96 hours, then used as targets for the Micro PIXE imaging. Micro PIXE imaging was performed using 2.0 MeV proton beam of 10 μm diameter. Carboplatin was detected by means of the X-rays emitted from Pt.

2.2.Test for the hyaluronic acid-alginate liquie core capsule

The mixture of 3.0 % hyaluronic acid and 2.0 % alginate, supplemented with 0.2 mmol of carboplatin was prepared. The capsules were generated by spraying the mixture into 0.34 mol/l of CaCl2., using micro atomizer. The capsules were washed by 0.1mol/l tris buffer (pH 7.4) for 3 times, and placed on the mylar film. After that, the capsules were irradiated. The radiation was performed by a single dose of 0.5 Gy, using

^{60}Co γ-ray irradiator. Immediately after radiation, the capsules attached on mylar film was freeze-dried by the same way described in 2.1. The kinetics of carboplatin was observed by detecting the X-rays from Pt and imaged using the micro PIXE camera.

3. Results and Discussion

3.1 Kinetic of carboplatin (Pt) and Cu under the low dose radiation

The kinetics of the carboplatin is shown in Fig. 1. In cells treated by the carboplatin only, there was a little uptake of carboplatin (Pt), instead, relative high content of Cu was observed. With the low dose irradiation of 0.5 Gy of ^{60}Co γ-ray, the increased uptakes of both carboplatin (Pt) and Cu were observed. It is suggested that: the common pathway may exist for carboplatin and Cu uptake; and the pathway is facilitated by irradiation.

3.2 The emission of carboplatin from capsules by radiation

The image of the platinum was shown in Fig. 2. A capsule, which was described as a round shaped accumulation of Pt (within circle), emitted the carboplatin that was circumscribed by the dashed line. It is considered that: the hyaluronic acid- alginate liquid core capsule emit its core by irradiation.

In the cancer therapy, radiation has been used for only to treat the cancer. But its easy manipulation of the dose distribution, it is considered that the radiation may be suitable for localize the distribution of chemotherapeutic reagents. The increased uptake of carboplatin by irradiation, can increase the distribution of carboplatin. The capsules that is decomposed radiation is considered to enable to localize the distribution of the chemotherapeutic reagents.
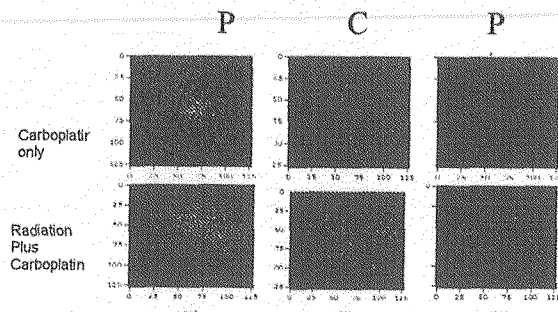
Fig.1 The kinetics of Pt as carboplatin and Cu.
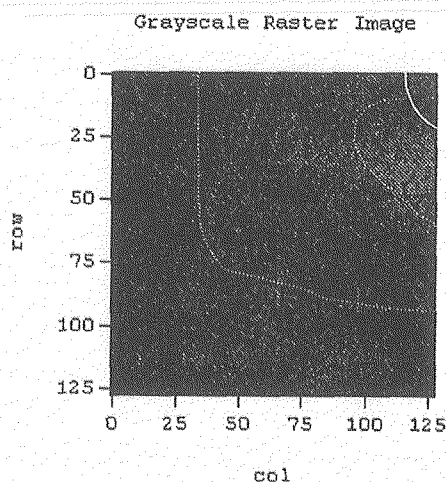
Fig. 2 The carboplatin emitted from capsule by radiation. Dashed line; Emitted carboplatin. Circle: capsule

References
1) Loehera, P. J. and Einhorn L.H. Ann Intern. Med. (1984)100 704-713
2) Seiko Ishida, Jaekwon Lee, Dennis J. Thiele et. Al. PNAS 99 (22) 14298-14302 (2002).
3) Yakovlev AG. Wang G. Stoica BA. Nucleic Acids Research. (1999) 27(9) 1999-2005
4) Molteni A. Ward WF. Kim YT et al. Advances in Experimental Medicine & Biology. (1989)258 273-85,
5) A. Wyss, N. Cordents, U. von Stocker, I.W. Marison.Biotech.Bioenge.(2004).87(6), 734-742

JP0650265

7.12 Standard Reference Material for Micro Beam PIXE Made of Macroporous Ion Exchange Resin

Y. Iwata[*], K. Ishii[**], T. Kamiya[***], T. Sakai[***], T. Satoh[***] and M. Oikawa[***]

Department of Chemistry, Faculty of Education and Human Studies,
Akita University[*]
Department of Quantum Science and Engineering, Graduate School of Engineering,
Tohoku University[**]
Advanced Radiation Technology Center, JAERI[***]

1. Introduction

Standard Reference Material (SRM) is indispensable to the calibration of apparatus and the evaluation of the accuracy and precision of analytical technique. A lot of SRMs have been prepared and issued. Conventional SRMs are suitable for bulky samples in liquid or solid form and they are applied to many kinds of analytical technique such as spectrophotometric analysis, mass spectrometric analysis and activation analysis[1].

Particle Induced X-ray Emission (PIXE) is a powerful tool for multi-element analysis of biological and environmental samples[2,3]. The highest sensitivity is obtained by 2-3 MeV proton bombardment, and the sensitivities for most essential and toxic elements of organisms are 0.1 - 4 ng / cm^2. PIXE is well suited for trace analysis of a small, <0.5 mg or thin, <1 mg/cm^2 target on a thin film support with organic specimens. PIXE has so unique and particular suitability to properties of analytical sample. Nowadays new SRMs are necessary for PIXE analysis, especially for micro beam PIXE.

In previous work, we investigated utilities of three types of SRM for PIXE, i.e. Spot Sample, Vapor Coating Sample and Particle Sample by 3 MeV proton bombardment from micro beam system of TIARA[4]. Then, it was found advantages for Particle Sample made by adsorption of metal ions on ion exchange resin. Particle Sample is similar to biological cell because it is spherical in shape and its matrix elements are carbon, oxygen and hydrogen. Particle Sample has a possibility for use as pseudo-biological SRM.

On the other hand, several unsuitable character for SRM were found by imaging of Particle Sample, ununiform distribution of Cu in the resin and shadow caused by self-shielding of characteristic X-ray.

In this work, we made SRM for PIXE by smaller ion exchange resins than previous work. These resins are macroporous type. We expected uniform distribution of elements in the resin because the ion exchange sites located throughout the matrix.

2. Experimental
2.1 Preparation of Particle SRM

Two kinds of ion-exchange resin, Macro-Prep 50CM and Macro-Prep 25S (Bio-rad) were washed with Millie-Q water. Ion-exchange resin (ca. 12.5 ml) was suspended in water and transferred to a 25 ml measuring cylinder. This suspension was allowed to stand for over night and volume of

the resin was measured. This suspension was transferred to a 25 ml volumetric flask and made its volume to 25 ml by water. 1 ml of this suspension containing 0.5 ml of ion exchange resin was added to a 10 ml sample glass bottle stand and mixed with 2-3 ml of metal standard solutions in 0.01 M HNO₃. This mixture was shaken gently for overnight.

Concentration of elements in the resin was given by volumetric concentration such as ppmv (part per million in volume), and concentration of Ca in resin was 400 ppmv and other metals were 10-100 ppmv.

2.2 Preparation of Irradiation Target

About 1/4 drop of the suspension containing the ion exchange resin with interesting elements was attached to 5 μm Mylar film on the target holder. Fluid of the suspension was removed by paper string and resins were attached shatteringly on the film by a toothpick under a microscope. This target was subjected to 3 MeV proton bombardments by micro beam system of TIARA.

3. Results and Discussion
3.1 Macro-Prep 50CM

Macro-Prep 50CM has high selectivity for transition elements because its functional group of ion exchange is carboxyl group. This character will be advantage of this resin but size of this resin (50 μmϕ) is over size for micro beam PIXE. In the imaging for Ca distribution in the resin, the shadow caused by self-shielding of characteristic X-ray was observed in counter side to the face of Si(Li) detector. Macro-Prep 50CM was often decomposed and shrank by heat of irradiation. We wish that smaller resin would be on the

market soon.

3.2 Macro-Prep 25S

Particle size of Macro-Prep 25S is 25 μmϕ and functional group of ion exchange is sulfonic grope. Sulfonic grope has lower selectivity for transition elements
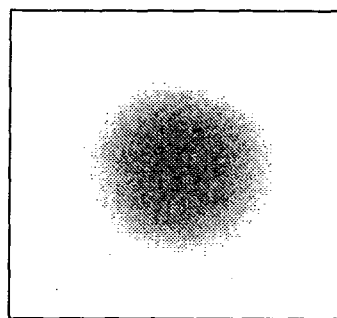
Fig. 1 PIXE image for S in Macro-Prep 25S by Micro Beam System
Scan area: 30 μm x 30 μm
Charge: 190 nC
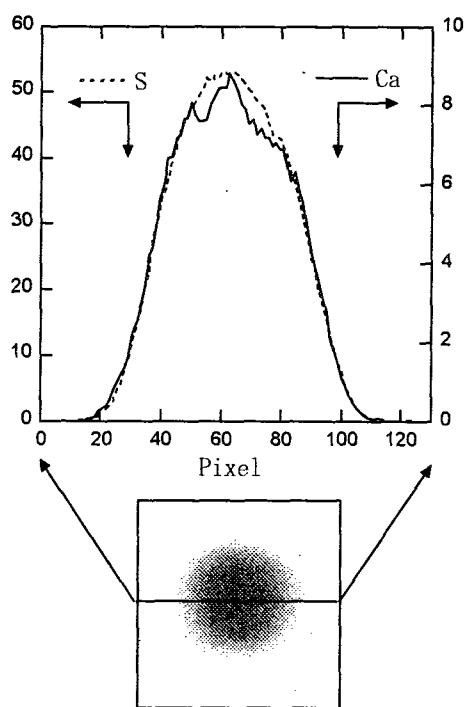
Fig. 2 Distribution of S and Ca in Macro-Prep 25S
[Ca²⁺] = 400 ppmv

than that of carboxyl group but it has enough stability for divalent and trivalent cations. Figure 1 shows PIXE image for sulfur in Macro-Prep 25A by micro beam system of TIARA. The shadow caused by self-shielding of characteristic X-ray was not observed in the image of sulfur.

Figure 2 shows the distribution of S and Ca in Macro-Prep 25S contains 400 ppmv of Ca^{2+}. It was found the macroporous nature of the resin (pore size; 72.5nm) allows cations to access the exchange sites located throughout the matrix. SRM made of macro porous resin has a possibility for use as pseudo-biological SRM for micro beam PIXE.

References

1) Y. Iwata and N. Suzuki, J. Radioanal. Nucl. Chem., 233 (1998) 49-53

2) K. Saitoh, Y. Iwata, K. Sera, K. Hirano, Intern. J. PIXE, 13 (2003) 51-64

3) Y. Iwata, A. Satoh, Y. Sasaki, R. Ito, K. Kuramachi, J. Radioanal. Nucl. Chem., 264 (2005) 295-301

4) Y. Iwata, K. Ishizawa, T. Sakai, T, Satoh, M. Oikawa, JAERI-Review, 2004-25, 278-279

JP0650266

7.13 Development of Support Software for Micro-PIXE Analysis

S. Abe*, K. Ishii*, K. Inomata*, H. Yamazaki*, S. Matsuyama*,
E. Sakurai**, K. Yanai**, T. Kamiya***, T. Sakai***, T. Satoh***,
M. Oikawa*** and K. Arakawa***

Department of Quantum Science and Energy Engineering, Tohoku University*
Department of Pharmacology, Tohoku University School of Medicine**
Advanced Radiation Technology Center, JAERI***

1. Introduction

PIXE (Particle Induced X-ray Emission) is a powerful method for the analysis of trace elements. Micro-PIXE is capable of providing spatial distributions of elements on the micron scale by focusing the beam spot to within $1\mu m$. In-Air Micro-PIXE was developed at the Takasaki Ion Accelerators for Advanced Radiation Application (TIARA) facility in the Japan Atomic Energy Research Institute (JAERI).

Micro-PIXE analysis has been widely applied to biology and medicine, and it allows performing a quantitative elemental analysis on each cell. However, the available quantitative Micro-PIXE data do not include the information of individual cells, thus a data base constructed in such viewpoint is needed. Since quantitative calculations are time consuming, it is necessary to facilitate analysis. Moreover, living body samples such as cells require a statistical analysis due to a natural spread of elemental abundance. Therefore, we aimed to develop analytical support software with such characteristics.

2. Analytical method

We analyzed Rat basophilic leukemia cells (RBL-2H3) using Micro-PIXE. The RBL cell is used as an experimental model for the allergy function. We prepared four kinds of cellular samples (cells stimulated with an antigen(vitamin D-binding protein-human serum albumin), non-stimulated cells, cells stimulated with the antigen and iron ion and cells stimulated with the antigen and olopatadine) and measured the elemental distribution and quantified the elements. The elemental distributions of stimulated cells and antigen + olopatadine stimulated cells are shown in Fig.1 and 2.

Since, as shown in Fig.2, Na and Ca are not observed, the symptom that shows the allergic reaction by olopatadine stimulation cannot be confirmed. It seems that an effect of suppressing stimulation is functioning in the case of antigen + olopatadine stimulated cells. The fixed quantity calculation of four kinds of samples is carried out by using a developed software. The distribution image of phosphorus (P) is specified to speculate a shape of cell, and based on a contour of P-distribution the image data is transferred to a binary image data to distinguish mathematically each cell. By calculating the elemental amount for each cell, the frequency distribution for each elemental amount can be obtained. If the cells take the element with a probability in their cycle, the frequency distribution coincides with binomial distribution, the Poisson distribution, or normal distribution.
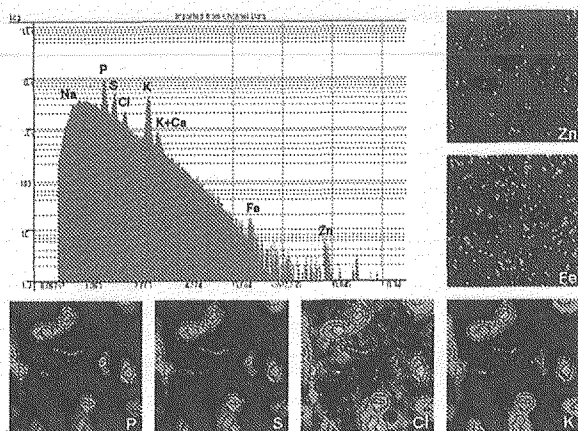
Fig.1 Element distribution of stimulated cells.
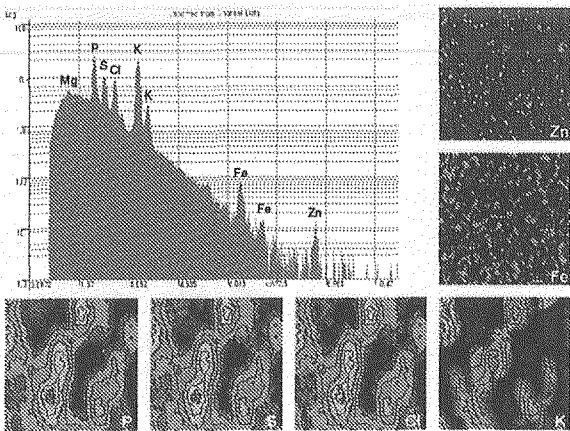
Fig.2 Element distribution of cells stimulated with an atigen and olopatadine.

3. Result

We developed an analytical support software including the functions of quantitative calculation for each cell and statistical analysis, and analyzed the experiments. We derived the frequency distributions of phosphorus, sulfur, chlorine, and potassium contained in all samples from the quantitative calculations, and compared them with probability distributions (normal distribution, binomial distribution, and Poisson distribution). Figure 3 shows the comparison of the result between the frequency distribution of P in the stimulated cells and the Poisson distribution. The frequency distribution of phosphorus coincides with the Poisson distribution, that is, it is assumed that the probability of taking the element into the cell is very small and the element is taken through the numerous cycle frequency compared with the prediction of binominal distribution. The similar tendency was obtained for four kinds of samples analyzed. The frequency distributions of sulfur and potassium coincide with both of the binominal distribution and the Poisson
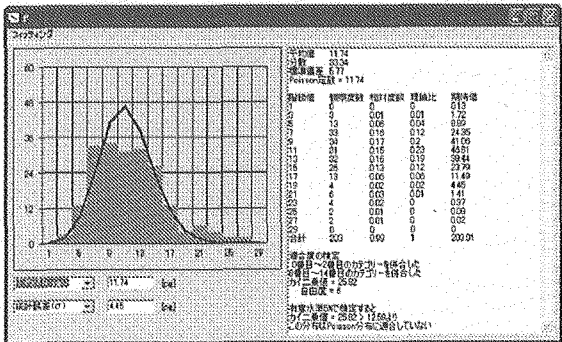
Fig.3 Comparison between the frequency distribution of phosphorus amount per cell and the Poisson distribution.

distribution. This reason is considered to be due to small population rate of cells. The distribution of chlorine showed the binomial distribution. In addition, we obtained the mean value and the standard deviation of elemental amount for each sample as basic data of the RBL cells.

4. Conclusion

The developed software facilitates the quantitative calculations and statistical analysis for Micro-PIXE cellular data, however, improvement of spectral analysis technique for K and Ca is desired.

JP0650267

7.14 Energy Spectra of Cluster-induced Electrons Emitted from Solids: Nonlinear Atomic Collisions in Condensed Matter

H. Kudo*, R. Uchiyama*, M. Furutani*, H. Wakamatsu*, S. Tomita*,
K. Shima**, K. Sasa**, S. Ishii**, Y. Saitoh***, S. Yamamoto****,
K. Narumi***** and H. Naramoto*****

Institute of Applied Physics, University of Tsukuba*
UTTAC, University of Tsukuba**
Advanced Radiation Technology Center, JAERI***
Department of Material Development, JAERI****
Advanced Science Research Center, JAERI*****

1. Introduction

For incidence of MeV atom clusters on solids, the collision-induced phenomena associated with electronic stopping are known to be sub-linear with respect to the number of constituent atoms in the cluster n.[1-3] This is contrast to the super-linear character of the phenomena closely related to nuclear stopping, such as sputtering or collision-induced damage. While an appreciable number of observations for the sub-linear cluster effect have been reported, its physical explanation has yet been an open question.

A typical electronic-collision phenomenon, i.e., electron emission from solids bombarded by fast atom clusters is a key phenomenon for the study of nonlinear inelastic effects characteristic of the cluster-solid interactions. Therefore, we have carried out measurements of n dependence of the energy spectra of electrons induced by MeV cluster impacts, which might allow essential understanding of the sublinear electronic processes .

2. Experiment

The beams of C_n^+, Al_n^+, and Au_n^+ (typically, n=1~3) were obtained from the 3MV tandem accelerator at JAERI-Takasaki and from the 1MV Tandetron accelerator at UTTAC. They were incident on the samples of chemically cleaned Si and highly-oriented pyrolytic graphite (HOPG) with a cleaved (0001) surface. The surface of the Si sample was cut ~2.5° off from the (100) surface so that the ions suffer no channeling effect under incidence in the normal direction of the surface. The experiments were carried out at room temperature under a pressure of ~5×10⁻⁶ Pa.

The emitted electrons from the bombarded targets were measured at 180° with respect to the beam direction, using a 45° parallel-plate electrostatic spectrometer of the double-deflection type.

3. Results and discussion

Figures 1 and 2 show the ratios the cluster-induced spectra to that for n=1, obtained from measurements for HOPG targets bombarded by 1.17 MeV/atom Al_n^+ and 1.67 MeV/atom Au_n^+, respectively. The ratios take minimum values at ~0 eV, increase with increasing the electron energy, and become ~1.0 at energies typically higher than 30 eV. The absence of the cluster effect for the high-energy electrons stems from the fact that these electrons are originated from close encounter between the cluster atoms and the target electrons.

In contrast, the yield ratios near zero electron energy stem mainly from the distant collisions between the cluster and the target atoms near the

surface layer. The ratios of the spectra can therefore be interpreted in terms of the amount of energy transfer to the target electron, which can be associated with the classical impact parameter.
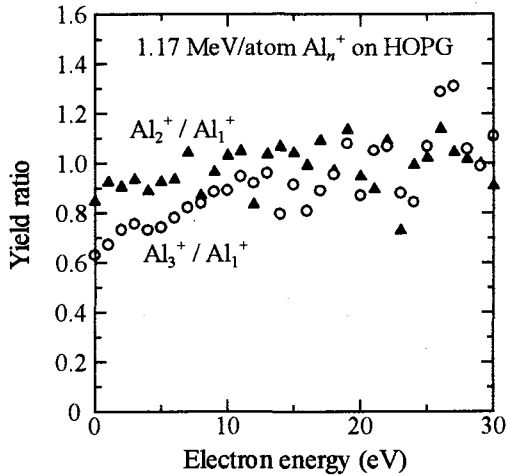
Fig. 1 Ratios of the spectra for HOPG bombarded by 1.17 MeV/atom Al_n^+ ($n=$ 1~3).
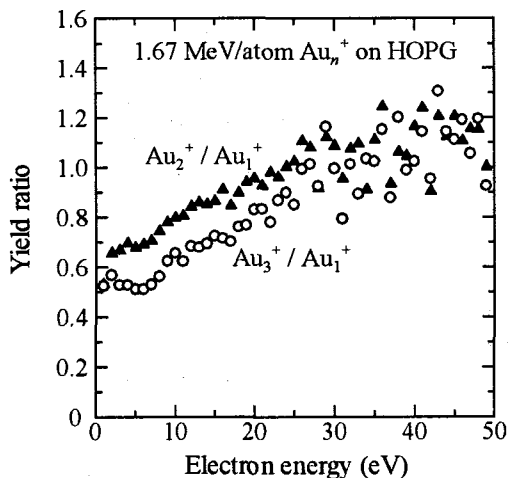
Fig. 2 Ratios of the spectra for HOPG bombarded by 1.67 MeV/atom Au_n^+ ($n=$ 1~3).

The escape length of electrons emitted at ~0 eV energy is a measure of the thickness of the surface layer of interest, where the observed nonlinear electron emission mainly occurs. Since the surface potential barriers (work functions) for HOPG, Si, and Au are equal to ~5 eV, the electrons that are released from the surface at ~0 eV energy should have a kinetic

energy of ~5 eV above the Fermi level in the target. According to the theoretical estimate and the compiled experimental data, the mean free path for electron inelastic scattering in Si is 60~80 Å for electrons of 5 eV energy above the Fermi level. Since the mean free path does not sensitively depend on solid material, the similar value as the mean free path for Si may be assumed for HOPG.

The electrons produced with energies higher than ~5 eV above the Fermi level can also be emitted with ~0 eV energy after losing their kinetic energies in the outgoing paths. To estimate such an energy loss effect, the behavior of electrons of the most probable energy in the target, corresponding to the peak energy of ~4 eV is considered. The peak yields are mainly due to the electrons of 4+5=9 eV energy just before escape through the surface barrier to the vacuum. The energy loss of electrons at 9 eV above the Fermi level in Si, for example, is 0.20 eV/Å in the continuous slowing-down description, which is a factor of 4 greater than at 5 eV and, accordingly, the energy loss effect increases the escape length only by 4/0.20=20 Å.

Evidently, the energy loss effect for higher-energy electrons is unimportant because of the drastically decreased number of the produced electrons relative to the 0~10 eV electrons. It follows that the escape length of the ~0 eV electron yield can be estimated roughly as 100 Å (60~80 Å plus 20 Å). This implies that the observed nonlinearity results from the cluster-solid interaction in the surface layer of ~100 Å thickness.

The integrated yield, i.e., the area under the spectrum, can be used to discuss the nonlinearity since the area is determined mainly from the electron yield around the spectrum peak (0~10 eV range). Figure 3 shows the integrated yields Y_n per Al_n cluster for (a) HOPG and (b) Si targets. The results shows linear increase of Y_n

with increasing n, as are typically seen for the 0.24 MeV/atom case, although the slopes are smaller than for the case of no cluster effect (dashed lines). Also, for projectiles of higher velocity the slopes become larger, corresponding to less sub-linear emission of the electrons.
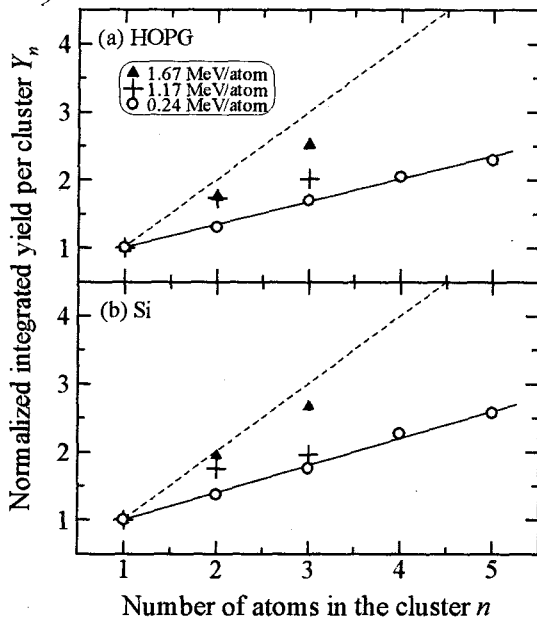
Fig. 3 Integrated electron yield Y_n per Al_n cluster, normalized to the case of $n=1$, for (a) HOPG and (b) Si targets. The symbols used are indicated representatively in (a). The estimated uncertainty in the values of Y_n is $\pm5\%$. The dashed lines indicate the linear dependence, i.e., $Y_n \propto n$, while the solid lines were drawn to guide the eye.

It is of fundamental interest to investigate the correlation of the cluster effect with the electronic stopping power of the projectile S_e. For HOPG and Si targets, the values of S_e for 1.67 MeV Al are greater than for 0.24 MeV Al by a factor of ~3. Accordingly, the experimental results noted earlier indicate weaker cluster effect for higher electronic stopping powers, i.e., stronger electronic interaction with solids. This can hardly be accounted for by the electron-sweep model of the cluster-induced electron emission, which predicts stronger cluster effect for higher electronic stopping

powers. At present, there is no applicable model for the present experimental results. For comparison of three-atom clusters ($n=3$), we have obtained the value of $Y_3=1.50\pm0.07$ for 0.5 MeV/atom C_3 incident on HOPG. This value is smaller than $Y_3=2.02\pm0.10$ for 1.17 MeV Al incident on HOPG. As the velocities of these projectiles are approximately equal, the same ionization mechanism, i.e., mainly the binary-encounter process, is expected to occur. This allows direct comparison of the cluster effect for these projectiles. Indeed, the stronger cluster effect for C_3^+ than for Al_3^+ is probably due to the shorter interatomic spacing of 1.3Å than 2.6 Å of Al_n, which is estimated from the specific weight.

4. Conclusion remarks

The reduced emission of the cluster-induced electrons with increasing the number of cluster atoms has been studied with the backward electron spectroscopy. The reduced emission is pronounced for 0~10 eV electrons which escape mainly from the surface layer of ~100 Å thickness, while the reduced electron emission disappears with increasing the observed electron energy. At present, there is no suitable model of the cluster-induced electron emission that can explain the present experimental results. Further experimental as well as theoretical studies, including not only the production but also the transport processes of the electrons, are required for a better understanding of the cluster-solid electronic interactions.

References

1) For recent review of cluster-induced phenomena, see, Jacquet, Y. Le Beyec, Nucl. Instrum. Methods B 193 (2002) 227-239.

2) E. Parilis, Nucl. Instrum. Methods B 193 (2002) 240-247.

3) The present work has recently been submitted to NIM-B.

This is a blank page.

8. Radiation Shielding for Accelerator Facilities

This is a blank page.

8.1 Characterization of ^{38}Cl and ^{39}Cl Formed by High-energy Proton Irradiation

S. Yokoyama[*], H. Noguchi[*], K. Sato[*], Su. Tanaka[**], Y. Oki[***], N. Osada[***],
Y. Kanda[****], T. Iida[*****] and H. Kaneko[******]
Department of Health Physics, JAERI[*],
Nippon Advanced Technology Co., LTD.[**],
Research Reactor Institute, Kyoto University[***],
Radiation Science Center, High-energy Accelerator Research Organization[****],
Graduate School of Engineering, Nagoya University[*****],
Advanced Radiation Technology Center, JAERI[******]

1. Introduction

In high-energy accelerator facilities, various radioactive aerosols and gases were produced by the spallation reaction of the nuclei of nitrogen, oxygen, argon and others with secondary high-energy particles generated in the accelerator rooms[1]. Radiolytic products such as nitric acid are also generated in the air of the high-energy proton fields[2]. These materials may influence the formation of the radioactive aerosols and gases. To estimate internal doses due to inhalation of these radioactive materials, the physicochemical characteristics of radioactive aerosols and gases, in particular, the particle size of aerosols and the chemical form of gases, are very important. However, there is not enough information of the particle size and chemical form of gases for radioactive chlorine which is formed from argon gas in the air by the nuclear spallation reaction.

Thus we have measured the ratios of radioactive chlorine aerosols and gases which are formed by irradiating highly-purified air or argon gas-added air with high-energy protons at TIARA. In addition, the particle size distribution and chemical form of non-radioactive aerosol produced simultaneously were examined.

2. Experimental methods

The proton irradiation experiment was carried out using HB course of TIARA. The schematic diagram of experimental apparatus is shown in Fig.

1. An irradiation chamber (diameter 10 cm and length about 80 cm) was set on the beam axis. The irradiation chamber was filled with highly-purified air (CO: <1 ppm, CO_2: < 1 ppm, total hydrocarbons: < 1 ppm and H_2O (dew point): <-70°C) or highly-purified air containing highly-purified argon gas (> 99.995 %) and moisture (RH: about 40%). These gases were irradiated with a 50 MeV proton beam. A proton fluence rate was 1.6×10^{10} s^{-1}. To examine the ratio of radioactive chlorine aerosols and gases generated by the proton irradiation, the radioactive chlorine produced in the air containing argon gas (Ar gas: 50 % and Air: 50 %) by the proton irradiation for 10 min was collected using a aerosol and gas sampler at a flow rate of 10 l min^{-1}. The sampler consists of a particulate filter (Cellulose membrane filter, filter type: AA, pore size: 0.8μm, Millipore Co.), Na_2CO_3-impregnated filters, which can concentrate acidic gas (2 stages), activated carbon fiber (ACF) filters (3 stages), which can trap gases passed through the Na_2CO_3-impregnated filters, and an activated charcoal cartridge (about 20 g) using as a back-up filter. The gas collected on the ACF filters is hereafter referred to as non-acidic gas. The γ-spectrum of the radioactive materials collected on the filters was measured by a germanium semi-conductor detector. The particle size distribution of non-radioactive aerosols formed in the moist air containing argon gas (Ar gas: 20 %, Air: 80 %) was measured using a scanning mobility particle sizer (Model 3936, TSI Inc.) for 5-min

irradiation. Non-radioactive aerosols generated in the purity air irradiated with the protons for 10 min were collected on a polytetrafluoroethylene (PTFE) membrane filter (pore size: 0.5μm, ADVANTEC Co.) at a flow rate of 10 l min⁻¹. In our previous proton irradiation experiment, nitric acid was detected from an inside wall of a glass vessel filled with the room air[3]. However, it is not found whether the aerosols are formed from nitric acid in the vessel. Thus the PTEF membrane filter that the particles were collected on was soaked in 10 ml of ultrapure water in a plastic vessel and was put in an ultrasonic bath for more than 30 min. The determination of nitrate in the extract was performed by a flow injection analysis method and the successive detection of nitric oxide by a chemiluminescence nitrogen oxide monitor[4]. The concentration of nitric acid in a blank PTFE membrane filter was also measured.

3. Results and Discussion

Figure 2 shows the distribution of radioactivity of the particles and gases collected on the particulate filter, Na_2CO_3-impregnated filters and ACF filters. The activity of ^{38}Cl and ^{39}Cl collected on the particulate filter is the highest. The second highest activity was detected on the ACF filter. The activity of ^{38}Cl and ^{39}Cl trapped on the Na_2CO_3-impregnated filters is lower than that of the ACF filters. Most of radioactive chlorine trapped on the Na_2CO_3- impregnated filters was detected on the first stage. Radioactive chlorine was not detected on the second and third stages of ACF filters. The activity of ^{38}Cl and ^{39}Cl in the charcoal cartridge is less than a detection limit. The percentages of radioactive chlorine aerosols and gases are about 80 and 20 %, respectively. In total radioactive chlorine collected on the filters, about 30 and 70 % are acidic and non-acidic gases, respectively. There is no significant difference in the radioactivity distribution between ^{38}Cl and ^{39}Cl.

Consequently, ^{38}Cl and ^{39}Cl formed from argon

gas exist as aerosol, acidic gas and non-acidic gas. In addition, the physicochemical properties of ^{38}Cl and ^{39}Cl formed in a proton irradiation field would be similar. Doses due to inhalation of acidic or non-acidic ^{38}Cl and ^{39}Cl gases cannot be estimated because of the lack of dose coefficients for gaseous ^{38}Cl and ^{39}Cl[5, 6]. Thus there is a large uncertainty in an estimated dose due to the inhalation of radioactive chlorine including gases.

The particle size distributions of non-radioactive aerosol produced by the proton irradiation are shown in Fig. 3. The aerosol concentration has a peak at an aerodynamic diameter of 20 nm immediately after the start of the irradiation. After 80 s, the highest concentration of aerosols appears at a diameter of about 40 nm. The total concentration decreases and the peak of aerosol concentration more than 20 nm has a tendency to shift to the large particle size side with time. However, there is not a significant decrease in the particle concentration less than 20 nm during a period of 80 to 280 s. The time variation of particle size distribution is probably attributed to coagulation of particles. The generated small particles coagulate to form larger size particles and then attach to the large particles. The result suggests that the dose due to inhalation of aerosols generated in accelerator facilities is not properly evaluated if the dose coefficient for 1 or 5 μm diameter particles provided by ICRP is used.

The amount of nitric acid detected from the PTFE membrane filters is listed in Table 1. The amount of nitric acid in the PTFE filter that particles were collected on is about two times as high as that in the blank filter. Thus the chemical form of aerosol generated from the purified air by the proton irradiation is nitric acid formed from nitrogen, oxygen and a small amount of water remained in the irradiation chamber.

4. Summary

The characteristics of airborne ^{38}Cl and ^{39}Cl and

non-radioactive aerosol produced by the 50 MeV proton irradiation at TIARA were examined. It was found that ^{38}Cl and ^{39}Cl exist as aerosol, acidic gas and non-acidic gas. The activity of ^{38}Cl and ^{39}Cl aerosols was higher than that of the gases under this experimental condition. However, the gaseous ^{38}Cl and ^{39}Cl will not be ignored in the dose assessment for the inhalation of radioactive chlorine.

The non-radioactive aerosol formed by the proton irradiation of the purified air containing argon gas was very small particles in the early irradiation period. The non-radioactive aerosol concentration dropped with time after the start of irradiation. The particle size of non-radioactive aerosol shifted to larger with time. As a result of chemical form analysis of non-radioactive aerosol generated by proton irradiation, nitric acid was detected from the particles collected on the PTFE membrane filter.

These results will be very useful data to evaluate the dose due to inhalation in the high-energy accelerator facilities.

References
1) H. Muramatsu, et al., Appl. Radiat. Isot., 39 (5) (1988) 413-419.
2) Y. Kanda, et al., J. Radioanal. Nucl. Chem. 247(1) (2001) 25-31.
3) Y. Kanda, et al.., JAERI-Review 2004-025 (2004) 289-290.
4) Y. Kanda, and Y. Taira, , Anal. Sci. 19 (2003) 695-699.
5) ICRP Publ. 68, Ann. ICRP 28 (4) (1994) ; Pergamon.
6) ICRP Publ. 72, Ann. ICRP 26 (1) (1996) ; Pergamon.

Table 1   Measurement of the amount of nitric acid detected from PTFE membrane filter.

	Nitric acid (mol)	
Blank filter	Particles collected on a filter	
1.6×10^{-8}	3.3×10^{-8}	
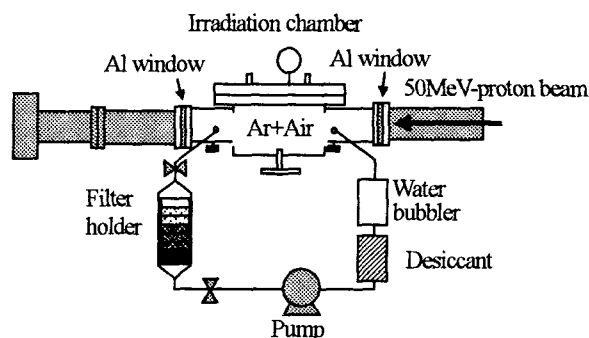
Fig.1 Schematic diagram of experimental apparatus on discrimination of radioactive chlorine aerosols and gases.
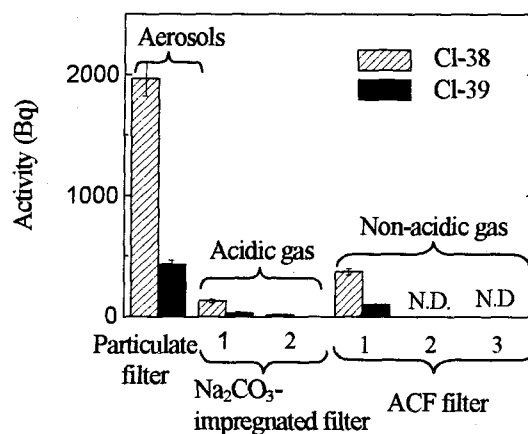
Fig. 2 Distribution of ^{38}Cl and ^{39}Cl activity on the filters (Ar 50% + Air 50%, RH: about 40%).
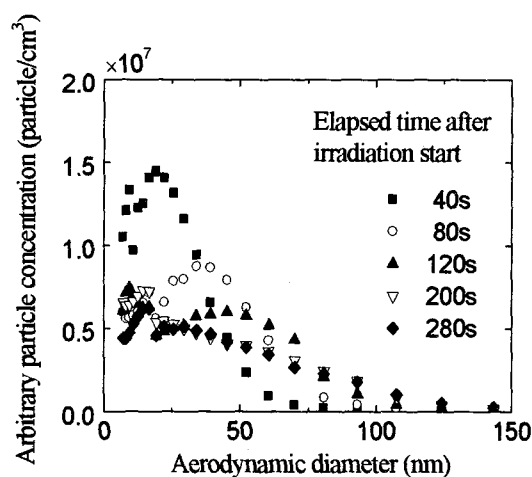
Fig. 3 Particle size distribution of non-radioactive aerosol generated by proton irradiation.

JP0650269

8.2 Measurement of Secondary Heavy Charged Particle Spectrum Produced by Tens of MeV Neutron Induced Reactions
(Measurement of Basic Data for Evaluation of External Dosimetry)

M.Hagiwara*, T.Sanami**, T.Ohishi*, M.Baba*, Y.Iwamoto***,
H.Nakashima*** and Su.Tanaka****

Cyclotron Radioisotope Center, Tohoku University*

Radiation Science Center, High Energy Accelerator Research Organization**

Center for Proton Accelerator Facilities, JAERI***

Advanced Radiation Technology Center, JAERI****

1. Introduction

To estimate neutron-induced irradiation effects for human and instruments, energy and angular distribution data for secondary charged particles produced by nuclear reaction with neutron are indispensable. Data for fragments which are particles heavier than helium particularly attract much attention on field of the space technology in recent years. Fragments are less produced than lighter particles, but cause the large local ionization in a micro-meter region because of the high LET. The local induced charge results in peculiar effects such as single event upsets (SEU) which become serious problem in space as well as on the ground level. For the evaluation of SEU, the energy and angular spectrum data which are known as double differential cross sections (DDX) for fragment production are required. The data also are important for human dose estimation.

Up to now, however, the data of the fragment production are very scarce except for the data by activation method that did not provide energy and angle information of the fragments. The reason of this fact originates in experimental difficulties for direct fragment detection, i.e., low yield, large energy loss in samples. Furthermore, theoretical calculations treating the fragment production are very few and uncertain. Therefore, it is important to develop an experimental method suitable for the fragment measurement and to accumulate reliable experimental data.

Our group has developed the method using Bragg curve spectrometer (BCS)[2,3] to measure fragments. In the previous report, we designed a prototype BCS with special care to apply to neutron beam which is unique in the world and resulted in success to identify the fragments by neutron-induced reactions.

In this study, an anode electrode with a segment pattern was adopted to the Bragg curve spectrometer (BCS) to overcome the problem for uncertainty of the detector solid angle. The BCS was tested using a mixed α-source and fragments produced by 75 MeV quasi-monoenergitc neutron source at TIARA[1]. Besides, the solid angle obtained with the segmented anode was compared with calculation based on energy-range relationship. Using a calibrated α-source, good agreement among experimental and calculation for the detector efficiency was confirmed. The signal selection with the segment anode improves particle separation in lower energy region.

2. Bragg curve spectrometer

The outline of technique using BCS for neutron-induced reaction was described in the previous report. To enlarge the solid angle of

detector against very small yields of neutron-induced fragment, a sample is set on the cathode plate inside the BCS. The arrangement succeeded in the detection of fragment from thin sample (10 μm polypropylene) induced by 75 MeV neutrons. On the other hand, a problem arises in the detector solid angle determination because some fragment emitted with high energy or large angle escape to out of sensitive region of BCS. Moreover, such an escaped fragment makes the particle identification worse because the energy deposition does not show the Bragg curve. Therefore BCS should be improved to overcome the problem.

Figure 1 shows schematic view of the BCS with a segment anode electrode. The BCS is a cylindrical shaped grid ionization chamber (GIC)[4] filled with a low pressure Ar+10%CH4 gas. By the segment pattern, the anode electrode is divided into two parts. The center part is a 5 cm diameter circle (equivalent to sample diameter). The residual ring shape part is named an around part. The signal ratio of the center part to the around part denotes to fragment angle. Thus, we can reject the side escape particle based on the ratio. Rejecting fragments with large emission angle, the particle identification of the BCS will be improved. In addition, a sample changer which can change three samples remotely is newly installed for cathode electrode.

3. Experiments

The experiment was performed at LC3 course, TIARA. To learn the performance of the segmented anode, mixed α-source (^{241}Am, ^{244}Cm, ^{237}Np) and fragments produced from carbon sample (100 μm thickness) by 75 MeV quisi-monoenergitc neutron source was used. The detector is set at 5 m from the ^{7}Li(p,n) neutron production target.

4. Results and Discussion

4.1 Mixed α-source

Figure 2 shows a result obtained using a mixed α-source. The left figure which is a scatter plot with signals of center and around electrodes shows good liner relation. The event making large signal on around electrode corresponds to large emission angle. Thus, by choosing events with no around signal, we can pick up events which stop in effective volume of BCS. In the right figure, the improvement of the energy spectrum is shown by removing the events that gives the signal to the around electrode. By using the signal rejection based on the around signal, the effective volume of BCS is defined clearly and can be calculated as a function of fragment range. The comparison of detector solid angle by calculation and experiment is shown in Fig.3. These two results are in good agreement.

4.2 Fragments induced by 75 MeV neutrons

The anode signal is fed to two different shaping time amplifier to obtain the Bragg peak height and total energy of fragments. Figure 4 shows two-dimensional spectrum of short (0.04 μs) and long (6 μs) shaping time for 100 μm thickness carbon sample. Fragments are separated more clearly with segment selection. We can obtain energy spectrum of fragments from this scatter plot and the solid angle determined in previous section.

Reference

1) M.Baba et.al., *Nucl. Instrm. Meth.*, **A428** (1999) 454.

2) G.R.Gruhn, et.al., *Nucl. Instrm. Meth.*, **196** (1982) 33.

3) N.J.Shenhav and H.Stelzer, *Nucl. Instrm. Meth.*, **228** (1985) 359.

4) T.Sanami, M.Baba, K.Saito and N.Hirakawa, *Nucl. Instrm. Meth.*, **A440** (2000) 403.
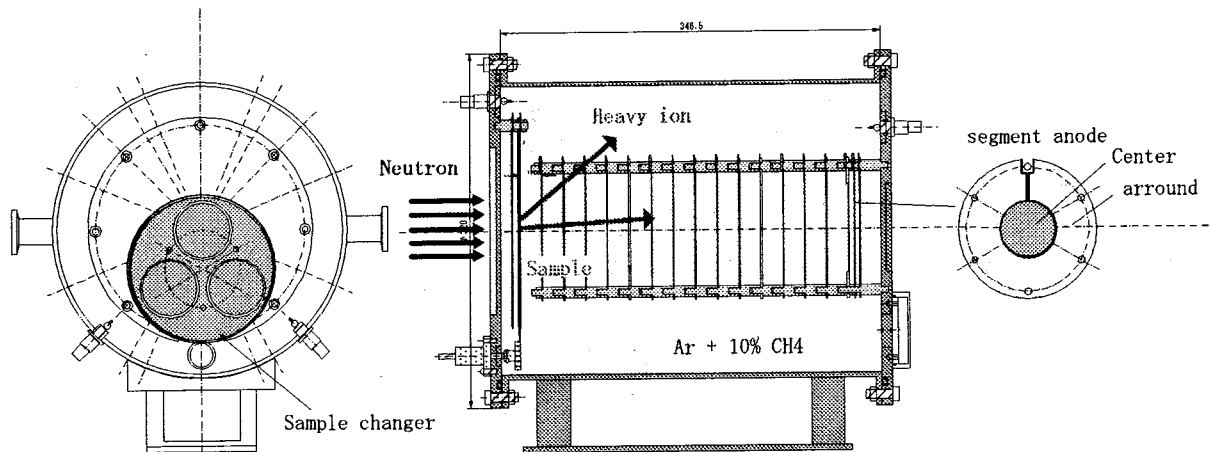
Fig.1 Schematic view of Bragg curve spectrometer, segment anode electrode and sample changer.
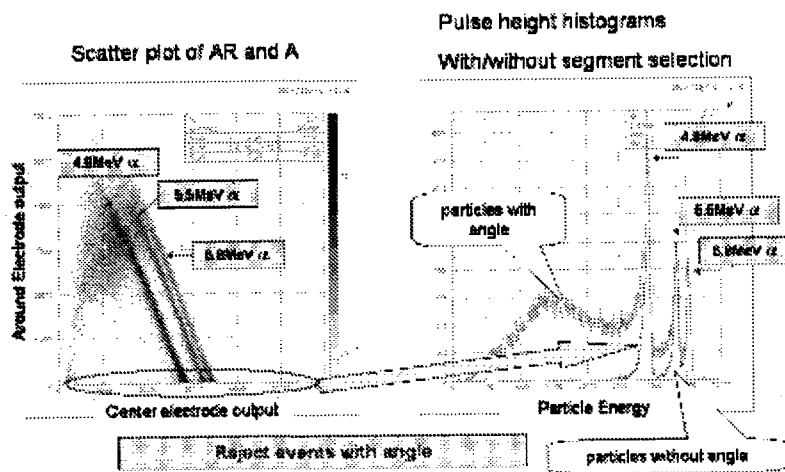
Fig.2 Scatter plot of signals from center and around electrodes, and energy spectrum with and without rejection for mixed α-source.
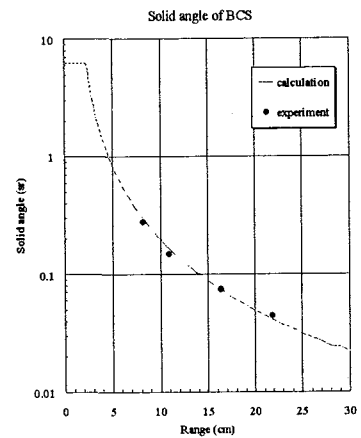
Fig.3 Results of solid angle as a function of fragment range.
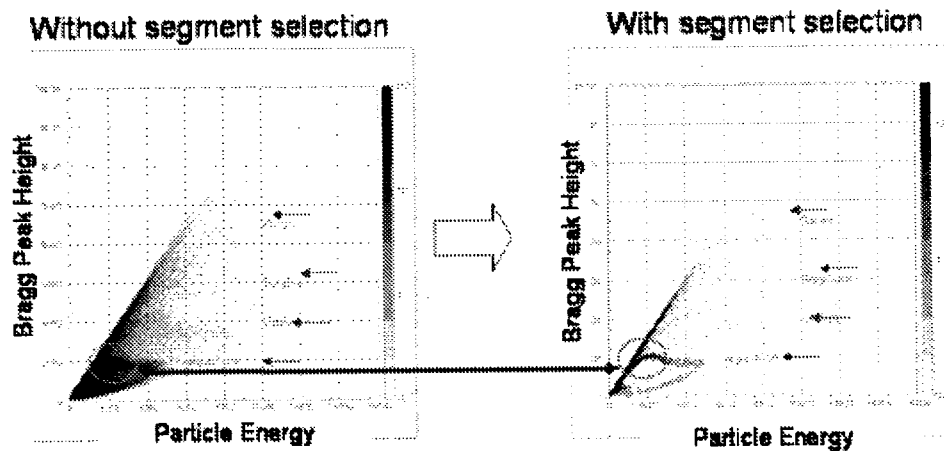
Fig.4 Demonstration of improvement for secondary fragment identification by event rejection with segmented electrode.

JP0650270

8.3 Evaluation of the Property for Quasi-monoenergetic Neutron Calibration Fields of High Energies at TIARA - Neutron Beam Profile Measurement -

Y. Shikaze*, Y. Tanimura*, Y. Uchita**, J. Saegusa* and Y. Yamaguchi*

Department of Health Physics, JAERI*, Institute of Radiation Measurements**

1. Introduction

In the facility of high energy proton accelerator, measurement of dose for high energy neutrons penetrating the shielding materials is important for the radiation management. For the precise measurement, appropriate calibration of the monitor and the dosimeter used there is necessary. As for the neutron energy more than 20 MeV, however, neutron calibration fields that take the international reliability of calibrated values into consideration are not established inside and outside the country. Moreover, the international standard of the calibration fields and techniques for such a high energy neutrons does not established. Therefore, by using the quasi-monoenergetic neutron irradiation field of 40-90 MeV at TIARA of JAERI Takasaki[1], we are developing the calibration field in order to use as the standard field. For the development, properties of the field must be well evaluated. In this year, since it was important for the calibration to know the spatial distribution and intensity of the irradiation field, we measured the neutron beam profile by using the imaging plates (IP) as the evaluation of the properties of the neutron field, where neutrons were produced in the nuclear reaction of the Li target with 45, 50 and 70 MeV protons.

2. Experimental procedure

2.1 Measurement by using the imaging plates

We measured the neutron beam profile in order to investigate spatial distribution and intensity of the irradiation field and their

variation as for the irradiated distance from the Li target. We used the IP (FUJI FILM, BAS-SR2025; for gamma-ray) set at the different position along the beam line. Schematic view of the neutron beam line and the neutron beam profile measurement was shown in Fig. 1. Since the IP had very low sensitivity for high energy neutron, we installed high density polyethylene as a converter and measured the neutron beam profile by measuring the recoil protons produced in the converter. Because the IP (BAS-ND) generally used for neutron measurement had high sensitivity only to the thermal neutron and the response of the IP (BAS-ND) for the scattering neutrons would relatively fade the response for high energy neutron of our interest, we applied the IP (BAS-SR) instead of the IP (BAS-ND).
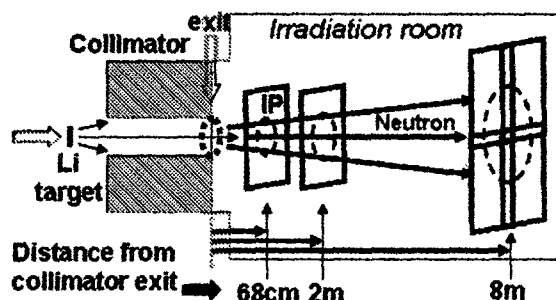
Fig. 1 Schematic view of the neutron beam line and the neutron beam profile measurement by using the IP for the irradiation field size and the neutron beam intensity measurement at different distance from the Li target.

2.2 Measurement of converter effect

In this measurement, we also investigated the influence of the converter on the resolution of

the irradiation field size measurement by changing the converter thickness with 0, 1, 3 and 5 cm. In this neutron calibration field, the shape of the neutron beam is circle since we use neutrons after passing through the collimator with a round hole as shown in Fig. 1. Therefore, we evaluated the resolution of the beam size measurement by using this diameter. In addition, the converter became radioactive by the nuclear reactions during the irradiation, and gamma-ray or beta-ray may affect the result of measurement. Therefore, we measured the radiation emitted from the converter after the irradiation by using the IP and the GM survey meter, and we estimated the type of the radiation components and their influence from the decay time obtained as the decreasing counting rate measured by the GM survey meter. Though the output intensity of the IP caused by the radiation from the converter can not be separated from the resultant output intensity of the IP during the irradiation, we can estimate it by using the calculated time variation of the radiation intensity from the converter. Since the IP measured the value correspond to the integrated counts of the radiation from the converter, we used the ratio of integrated counts before and after the irradiation calculated by the IRACM code[2]. The measurement period of the IP after the irradiation was same with that during irradiation.

3. Results and Discussion
3.1 Evaluation of converter effect

For the evaluation of the resolution of the irradiation field size measurement, we selected the thin strip area including the diameter and considered the FWHM of the intensity distribution in the area along the diameter direction as the beam diameter. Figure 2 shows the beam intensity distribution and the beam diameter obtained as FWHM for the converter thickness with 0 and 5cm. As a result, the

variation of the irradiation field size for different converter thickness was less than 0.2% of the beam diameter.
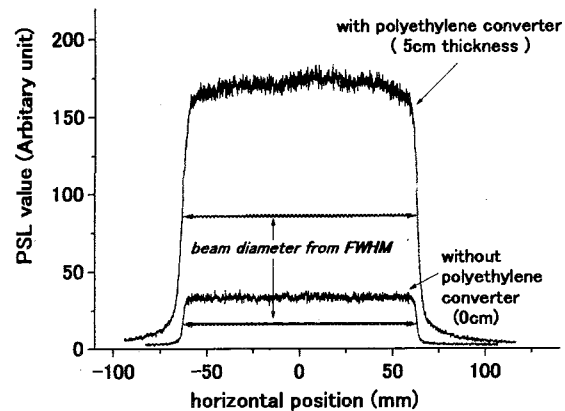
Fig. 2 Beam intensity distribution and the beam diameter obtained as FWHM for the converter thickness with 0 and 5cm.

In addition, as for the evaluation of the influence of the radiation from the converter, both from the decay time measurement by the GM survey meter and from the calculation results of IRACM code we confirmed that the radiation in the converter was mainly caused by ^{11}C generated by the $^{12}C(n,2n)$ reaction. Based on the intensity of the IP measured after the irradiation, considering the ratio in the calculation results before and after the irradiation, we estimated the intensity of the IP for the radiation from the converter during the irradiation. From the estimation, we found that the influence of the radiation from the converter during the irradiation period is negligibly small.

From the estimation about the thickness and the radiation of the converter, and from the improved S/N ratio that resulted from the increased sensitivity for the irradiation field as shown in Fig. 1, we confirmed that the measurement technique by using recoil proton from the polyethylene converter was effective for the measurement of high-energy neutron beam profile.

3.2 Results on the beam profile properties

By the technique mentioned above, the following measurement results were obtained. Figure 3 shows the average of the horizontal and vertical beam diameter obtained as FWHM as a function of the distance from the target for several beam energies. The arrows drawn vertically and horizontally indicate the distance of the collimator exit and collimator diameter, respectively. Since proton beam was actually incident on the target after adjusted its cross section to the area of 10mm in diameter, we also drew the lines of beam diameter calculated geometrically assuming the neutron generating area on the target as point, the area of 5mm and 10mm in diameter for comparison. The measured results seem almost consist with the actual proton beam size.
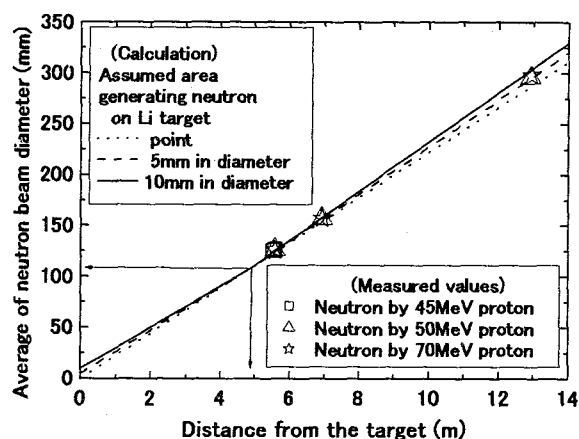
Fig. 3 Beam diameter obtained as FWHM of the IP data with the calculated results under the geometrical restriction as a function of the distance from the target for different beam energies.

Figure 4 shows the results of the relation between the beam intensity within irradiation field and the distance from the target. Here we take the value of the beam intensity within the irradiation field multiplied by the square of the distance from the target as vertical axis and the distance from the target as horizontal axis, and plot the results for different condition of beam

energy and converter thickness. The vertical axis value means the beam intensity per unit steradian, and the unevenness was within 5% from the mean value for each condition.
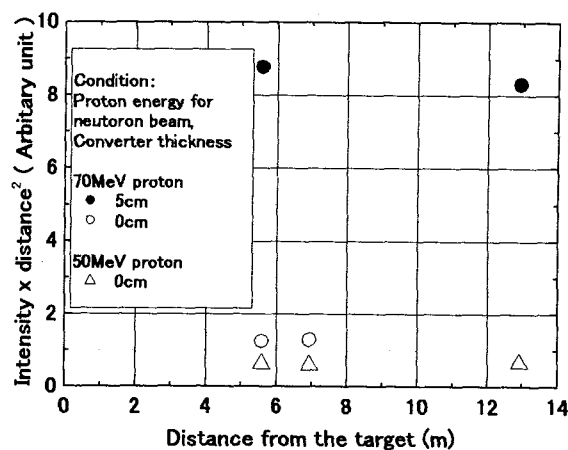
Fig. 4 Dependence of the beam intensity within the irradiation field area on the distance from the target for different conditions.

4. Summary

From the results in the previous chapter, we can summarize the properties of the high energy neutron calibration field at TIARA to the three points as follows: (1) Irradiation field area is fixed geometrically by the distance from the target and the diameter of the collimator exit; (2) The beam intensity within the irradiation field is in inverse proportion to the square of the distance from the target; (3) The fact, (1) and (2), do not depend on the beam energy.

References

1) M. Baba, Y. Nauchi, T. Iwasaki, T. Kiyosumi, M. Yoshioka, S. Matsuyama, N. Hiraoka, T. Nakamura, Su. Tanaka, S. Meigo, H. Nakashima, Sh. Tanaka and N. Nakao, Nucl. Instrum. Methods Phys. Res. A 428 (1999) 454-465.

2) S. Tanaka, M. Fukuda, K. Nishimura, H. Watanabe and N. Yamano, JAERI-Data/Code 97-019 (1997).

This is a blank page.

9. Accelerator Technology / TIARA General

This is a blank page.

9.1 Structure Analysis of Carbon Cluster Ion using Coulomb Explosion

A. Chiba[*], Y. Saitoh[*] and K. Narumi[**]

Advanced Radiation Technology Center, JAERI[*]

Advanced Science Research Center, JAERI[**]

1. Introduction

Recently, we have obtained interesting results on the interaction between a swift cluster ion and a solid in TIARA [1-3]. For the elucidation of the interactions and the physical effects, it is very important to grasp the structure of the cluster. For this purpose, a measurement system based on Coulomb explosion imaging (ECI) [4] for analyzing the structure of small carbon clusters has been developed. The ECI technique involves the foil-induced dissociation of a swift cluster by electron stripping. Using this technique, it has been demonstrated that it is possible to measure the nuclear density function for a broad variety of polyatomic molecules including the cluster. As our first step of the investigation on the carbon cluster structure, the preliminary experiment was carried out on the structure dependence of the average charge of atoms that composed a cluster passing through a thin foil.

2. Experiments

The experimental setup is shown in Fig.1 with a schematic view of a Coulomb explosion imaging system. A mass-selected cluster ion beam by the 90° analyzing magnet is chopped by the switching deflection plates and the aperture to produce beam pulses at a repetition rate of 10-800 Hz before injection into the tandem accelerator. The accelerated high energy pulsed cluster ions (1.0MeV/atom) are analyzed by the switching magnet and introduced into the high-vacuum chamber. The intensity of the beam is reduced by the attenuator to several ions per second. After passing through a thin carbon foil ($5\mu g/cm^2$), fragments of the incident cluster ions are detected with a luminous type multi-channel plate (MCP) to observe a projected pattern of the Coulomb explosion of the incident cluster ion by a CCD camera. Electrostatic horizontal deflection plates are placed between the foil and the MCP, and voltage up to $\pm 15kV$ is applied to each of the plates so that each of the fragments exiting through the thin carbon foil can be separated depending on its charge state.
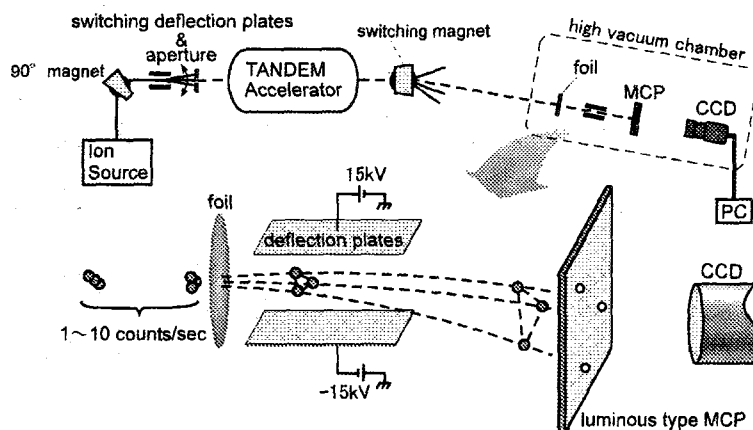
Fig.1. View of the experimental setup and schematic diagram of Coulomb explosion imaging.

3. Experimental results

Applying optimal voltage to the deflection plates, the charge state of the constituent atoms

of a swift carbon cluster (C_1-C_3, C_5, C_6) passing through the thin foil was defined. For each cluster, the distribution of accumulated luminance points on MCP is shown in Fig.2. For a given projectile, the rate of C^{2+} is the highest, and the rate of C^{3+} and C^{4+} decreases with the increasing cluster size.

In order to discuss the structure dependence of the average charge state, we checked the individual projected pattern of a set of luminance points. Projected Coulomb explosion patterns, which is equivalent to the patterns without the deflection voltage is considered to express the structure of the clusters before explosion. We calculated the projected Coulomb explosion patterns from the measured patterns using the deflection voltage and the charge state defined as described above. The corrected Coulomb explosion pattern of the C_3 projectile is shown in Fig.3. In Fig. 3-A, the geometry of the points shows a straight line, and the distances between the points are almost the same. We classified these cases into the linear-chain structure. The

Fig.2 Distribution of accumulated luminance points on MCP. The abscissa shows the position of the luminance points in the deflection direction and the unit is [mm]. The numerals describe the charge state.
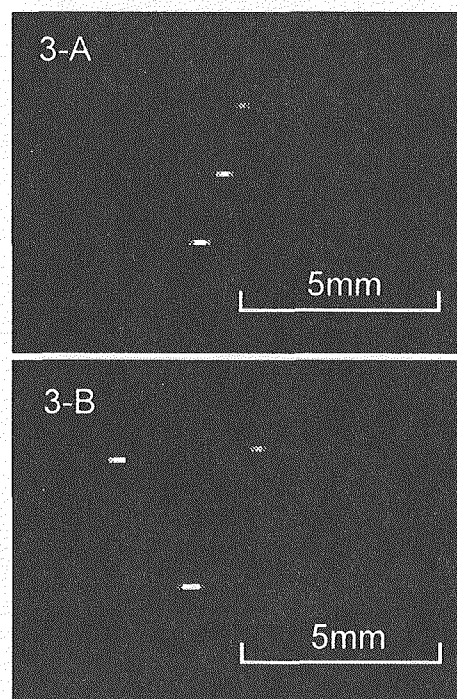
Fig.3 Projected Coulomb explosion patterns of C3, which calculated from the angle of constituent atoms deflected by the deflection voltage.

average charge state of the fragment ions for the carbon cluster of the linear-chain structure is 2.11. On the other hand, in Fig. 3-B, the geometry of the points shows a triangle, and the structure is classified into the ring structure. The average charge state which seems to be ring structure is 2.08. The result shows the same tendency as a calculated theoretical value [5].

4. Summary

The preliminary experiment which applied the Coulomb explosion imaging was capable of measuring the charge state of the constituent atoms of a swift carbon cluster after passing through a thin foil. And, we confirmed that the average charge state of the constituent atoms depended on the structure of clusters before explosion.

References

1) Y. Saitoh , A. Chiba, K. Arakawa, K. Narumi, K. Hirata, H. Shibata and A. Itoh, JAERI-Review 2003-033 (TIARA Annual report 2002) 300-302.

2) K. Hirata, Y. Saitoh, K. Narumi, Y. Kobayashi, Nucl. Instr. and Meth. B 206 (2003) 47-51.

3) K. Hirata, Y. Saitoh, A. Chiba, K. Narumi, Y. Kobayashi, K. Arakawa, Appl. Phys. Lett.83 (2003) 4872-4874.

4) Z. Vager, R. Naaman, E. P. Kanter, Science 244 (1989) 426.

5) T. Kaneko, Phys. Rev. A 66, (2002) 052901.

9.2 TOF Mass Spectrometry of Secondary Ions from HOPG Target Bombarded by Fast Cluster Ion Beams

H. Shibata*, H. Tuchida*, A. Itoh*, Y. Saitoh**, A. Chiba**, M. Fukuda**,
K. Arakawa**, Y. Ohara** and K. Narumi***
Graduate School of Engineering, Kyoto University*
Advanced Radiation Technology Center, JAERI**
Advanced Science Research Center, JAERI***

1. Introduction

Recently the interaction of fast (high energy) cluster ions with solids has attracted attention in basic physics and application fields[1-4]. As fast cluster ions can bombard a very small (atomic size) area of a solid surface by many atoms simultaneously and release large energy in a very short time (from femto- to pico-second region) [4]. This situation causes nonlinear effects or synergetic effects, which is unusual for single atom collision with solid targets.

Fast cluster ion beams used for the study of secondary ion emission processes were produced by the TIARA tandem accelerator. A time of flight (TOF) mass spectrometer combined with a pulsed cluster ion beam was used for a secondary ion measurement.

In this report we present some results of positive and negative secondary ion emission from a highly oriented pyrolytic graphite (HOPG) target bombarded by carbon cluster ions.

2. Experimental

The experimental system of TOF mass spectrometry was composed of a pulsed ion beam generating system and an ion flight time measuring system.

A chopper and two sets of slits installed in an injector beam line generated pulsed ion beams by chopping continuous cluster ion beams from an ion source. A square wave from a master pulse generator controlled a high voltage applied to parallel plate electrodes for chopping the beam. In this study pulsed cluster ion beams of 0.5 MeV/atom (~ 42 keV/amu) $C_1^+ \sim C_8^+$ ions were used. The interval and width of the pulsed beam used in this experiment were 125 μs and ~100 ns, respectively. C_4^+ and C_8^+ ions were produced in the ion source and C_1^+, C_2^+ and C_6^+ ions were fragments of C_8^+ ions after passing through charge stripper gas. As averaged beam currents of pulsed beams were too low to be measured, continuous beam currents were

measured before pulsing and were several pA for C_8^+ ions. The vacuum in a beam line and a chamber was kept at $\sim 10^{-7}$ Pa to prevent cluster ions from breaking.

A linear type TOF mass spectrometer and a TAC (Time to Amplitude Converter) system for time measurement were adopted as a secondary ion mass spectrometric system shown in Fig.1. The TOF mass spectrometer composed of an extractor, a drift tube (~50cm long), an acceleration electrode and a multichannel plate (MCP) detector. A TTL output from the pulse generator was used as a start pulse and a secondary ion signal from the MCP was used as a stop pulse of the TAC measurement system. Typical mass spectrum was accumulated for 30 minutes. Sheet shaped targets were used and bombarded at an incident angle of 45 degrees. The secondary ions were extracted to the normal direction from the target.
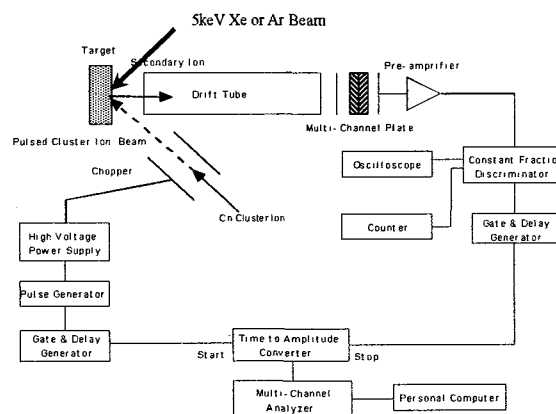
Fig.1 Schematic diagram of time of flight mass spectrometric system.

Targets having clean surface were prepared by bombarded with nA continuous cluster ion beams for one or two hours. However cleaning was still inadequate, so the target was bombarded by 5keV Xe or Ar ion beam from an ECR ion source for 10 ~ 20 minutes. Secondary ion spectrum was drastically changed in a large mass region by this cleaning method.

Some results of positive and negative secondary ion emission from a HOPG target bombarded by 0.5MeV/ atom C_1^+ ions, C_2^+, C_4^+ and C_8^+ cluster ions will be discussed.

3. Results and discussion

Mass spectra of secondary ions emitted from a HOPG target bombarded by C_1^+ ions and C_8^+ cluster ions are shown in Fig.2 and 3. The ordi

nate is the secondary ion yields normalized to the beam fluence in arbitrary units, and the abcissa is the channel number of multichannel analyzer, which corresponds to the flight time of ions (50 μs / 1024 ch). Secondary cluster or molecular ions are seen for any incident carbon cluster ion. And several dominant peaks of H^+, H_2^+, H_3^+, F^+, H^-, and F^- can also be seen. These
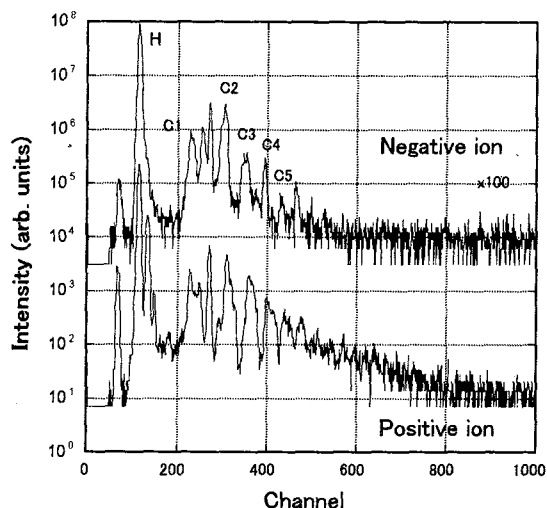
Fig.2 Mass spectra of positive and negative secondary ions emitted from a HOPG target bombarded by C_1^+ ions. Data were taken after bombardment of 5 keV Ar ion beams for 10 minutes.
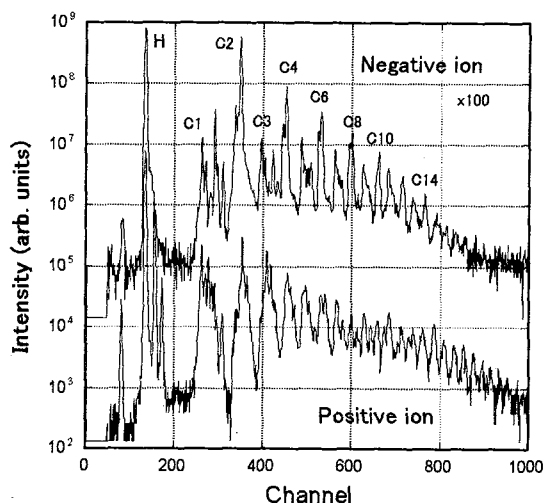
Fig.3 Mass spectra of positive and negative secondary ions emitted from a HOPG target bombarded by C_8^+ ions. Data were taken after bombardment of 5 keV Ar ion beams for 10 minutes.
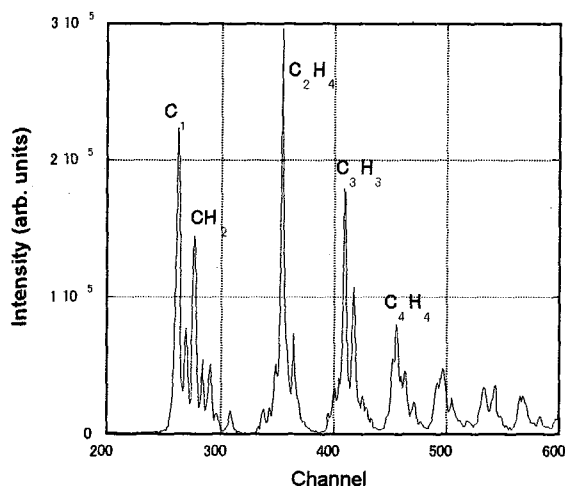
Fig.4 Positive secondary ion spectra emitted from HOPG target bombarded by C_8^+ ions (linear scale).
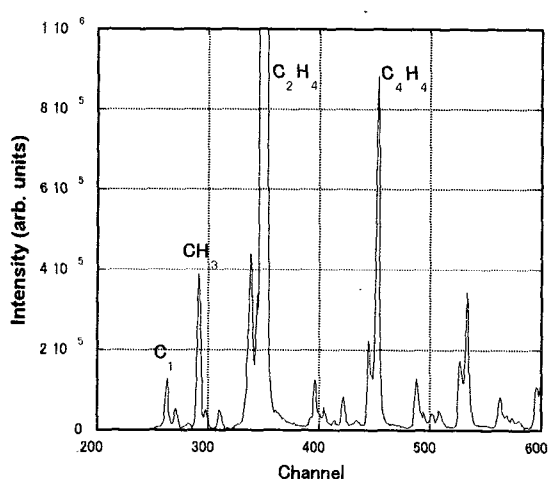
Fig.5 Negative secondary ion spectra emitted from HOPG target bombarded by C_8^+ ions (linear scale).

peaks are caused by surface contaminants.

Figure 2 shows typical mass spectra of positive and negative secondary ions, which were taken after bombardment of 5keV Ar ion beams for 10 minutes. The contaminants and

background signals remarkably diminished, and the secondary cluster or molecular ions appeared clearly, especially for C_8^+ ion bombardment shown in Fig.3.

In case of C_8^+ ion bombardment the emitted

positive secondary cluster or molecular ions related to C_m^+ (m = 1 - 21) can be seen and intensities of these peaks decay exponentially with m. Whereas for negative secondary ions, cluster ions related to odd numbers m of C_m have smaller intensities than cluster ions of even number m of C_m have. These peaks are composed of hydrocarbon molecules shown more precisely in Fig.4 and 5, which may be produced through chemical reaction, mainly ion-molecule reaction, on the target surface. Hirata et al. obtained similar results in cluster ion bombardment with polymer targets [5]. It is very interesting that the positive species of produced molecular ions on the target surface are different from the negative ones.

Figure 6 shows the ratios of yields of positive and negative secondary ions from HOPG target bombarded by $C_1^+ \sim C_8^+$ projectiles to the yield of positive ions for C_1^+ projectile. The yield of positive secondary ions for incident C_1^+ ions is unity. If the relation between the yield and cluster number n of incident carbon C_n is linear, the yield is n for C_n, which indicated by the solid curve in Fig.6. However, the value of yield ratio for each incident cluster ions C_n^+ is indicated by dots for positive secondary ions and triangles for negative ones in Fig. 6. The yields of negative secondary ions for all incident cluster ions C_n^+ are about twice of positive ion yields. The non-linear effect can be seen clearly.
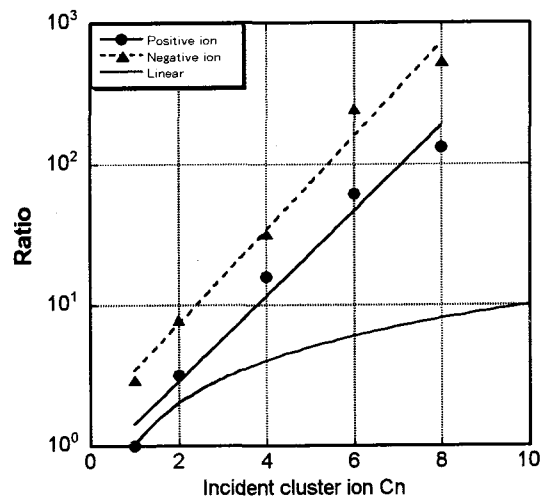
Fig.6 The ratio of yields of positive (▲) and negative secondary ions (●) emitted from HOPG target bombarded by $C_1^+ \sim C_8^+$ incident ions. The yield of positive secondary ions bombarded by C_1^+ ions is unity.

References
1) Y.Le Beyec, Int. J. Mass Spectrom. Ion Proc. **174** (1998) 101.
2) S.Della-Negra, et al., Nucl. Instrum. Meth. B**74** (1993) 453.
3) M.Döbeli et al., Phys. Rev. B **94** (1994) 388.
4) K.Boussofiane-Baudin et al., Int. J. Mass Spectrom. Ion Proc. **130** (1994) 73.
5) K.Hirata et al., Appl. Phys. Lett. **83** (2003) 4872.

JP0650273

9.3 Single-turn Extraction Technique for the JAERI AVF Cyclotron

S. Kurashima, N. Miyawaki, S. Okumura, I. Ishibori, K. Yoshida,
H. Kashiwagi, M. Fukuda, T. Nara, T. Agematsu and Y. Nakamura
Advanced Radiation Technology Center, JAERI

1. Introduction

A flat-top acceleration system using the fifth-harmonic frequency for the JAERI AVF cyclotron[1,2] was developed to reduce the energy spread of an ion beam mainly for microbeam formation with a spot size of 1 μm in diameter by focusing with a set of quadrupole magnets. A single-turn extraction is an indispensable condition to reduce the energy spread without significant beam loss by the flat-top acceleration. In order to save time for the single-turn extraction tuning over measuring time distribution of the beam bunch, a deflector probe has been developed to observe the turn separation and the radial beam width. As a result of beam developments using the deflector probe, the single-turn extraction can be observed in one or two hours and radioactivity of the deflector electrode can be also reduced in the acceleration of a high energy H^+ beam.

2. Development of a high resolution deflector probe

The flat-top acceleration using the fifth-harmonic frequency for an acceleration voltage is an excellent technique to reduce the beam energy spread. A radial spread of the beam bunch in the extraction region of the large scale AVF cyclotron is wider than the radial interval between the beam bunches when only the fundamental frequency is used. The energy spread of the beam bunch can be reduced by the flat-top acceleration owing to the uniformity of energy gain over a wide acceleration phase. In this case, the radial spread of the beam bunch can be narrowed than the interval between the bunches and all ions in the bunch can be extracted from the cyclotron at a time. This condition is
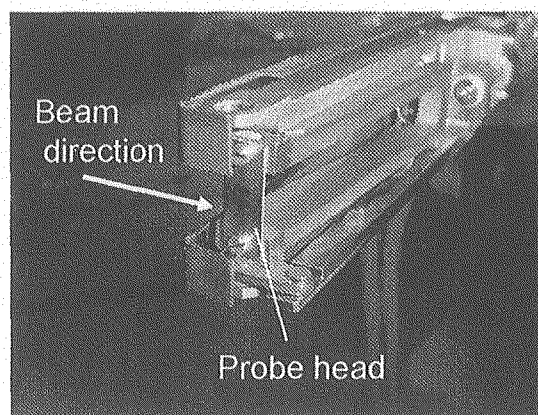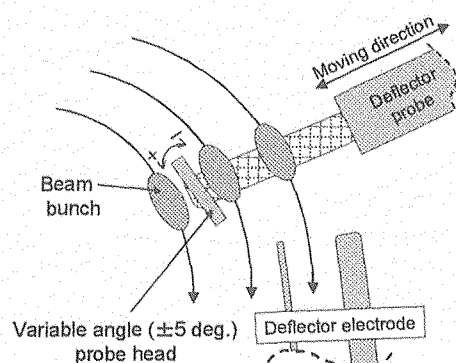
Fig. 1. Sketch of the measurement of the turn separation near the deflector electrode (upper) and picture of the probe head of the deflector probe (lower). Sheet tungsten is attached as the probe head. The angle of the probe head is changed from -5 to +5 degrees to observe a clear turn separation.

called a single-turn extraction. A current pattern observed by a thin wire probe in the extraction region shows separation of the beam bunches (turn separation) then. On the other hand, the condition that a beam bunch is extracted over several turns is called a multi-turn extraction.

The single-turn extraction is confirmed by observing that the number of the beam bunches extracted from the cyclotron is equal to the injected bunch number defined by the pulse beam chopping system in the injection line. This is a reliable method, however, it takes time to operate the chopping system and to measure time distribution of beam pulses after acceleration by a plastic scintillator.

Therefore, a high resolution deflector probe has been developed to confirm the single-turn extraction easily. Figure 1 shows a sketch of the measurement method of the turn separation near the deflector electrode and a picture of the probe head of the deflector probe. The probe head is a sheet of tungsten of 0.5 mm in thickness or a graphite rod of 0.5 mm in diameter. Since light ions like high energy H^+ penetrate the conventional thin wire probe, sensitivity

against beam current is low. The sheet tungsten head stops high energy light ions and the total beam current is measurable. As seen in Fig. 1, if the direction of the beam bunch is not parallel to the head, two beam bunches may be simultaneously picked up. Then, we cannot measure the real distribution of the beam. The angle of the probe head is remotely changed within ± 5 degrees to avoid this problem. Figure 2 shows the distributions of the beam current measured by the tungsten head. The angle of the head was changed to observe clearer beam pattern. A clearer turn separation was observed at +5 degrees than that at -5 degrees as shown in Fig. 2.

3. Beam development with the single-turn extraction

We have been developing a 260 MeV $^{20}Ne^{7+}$ beam with the flat-top acceleration system for experiments of microbeam formation[3]. The acceleration harmonics h = $f_{rf}/f_{particle}$ and the number of turns are 2 and 265, respectively. Operation parameters of the cyclotron, such as a ratio of the fundamental to the fifth-harmonic voltages, magnetic field, were optimized to observe a clear turn separation by using the deflector probe and the single-turn extraction was obtained. As a result of the single-turn extraction, the extraction efficiency was improved to more than 95 % (typically 60 % for the multi-turn extraction).

We also have started to develop a high energy H^+ beam which causes serious radioactivity at the deflector electrode. The acceleration harmonics of high energy H^+ beam equals 1. The number of turns at h = 1, 2 are 550 and 265, respectively. The interval between bunches is inversely proportional to the number of turns,
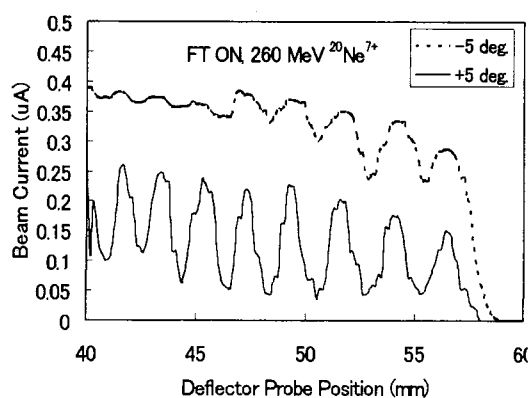
Fig. 2. Current distribution of 260 MeV $^{20}Ne^{7+}$ measured with the deflector probe.
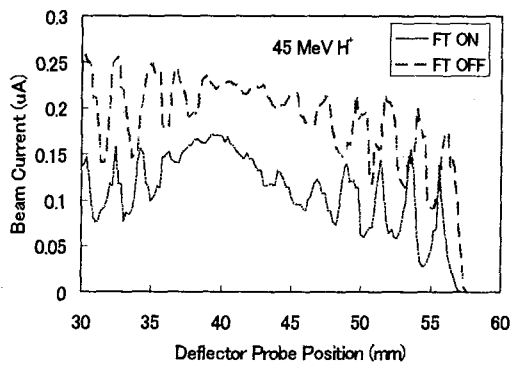
Fig. 3. Turn separation measured with the deflector probe. The angle of the probe head was fixed at +5 degrees. The accelerated ion beam was 45 MeV H^+. The acceleration harmonic and the number of turns are 1 and 550, respectively.
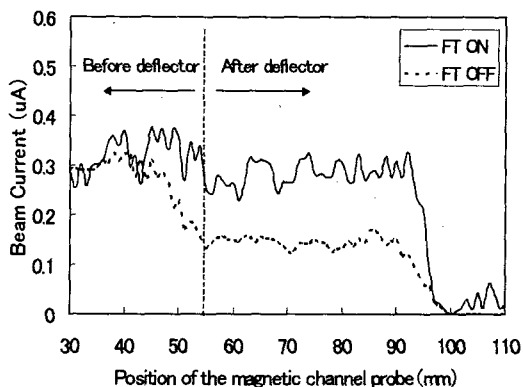
Fig. 4. Current distribution of 45 MeV H^+ measured with the magnetic channel probe. The extraction efficiencies are 86 % and 59 % for the flat-top ON and OFF, respectively. The efficiency is defined by the ratio of the beam current at the probe position of 80 mm to that of 40 mm.

therefore the single-turn extraction at h = 1 is more difficult than at h = 2. Figure 3 shows the distributions of the beam current of the 45 MeV H^+ measured by the deflector probe with the tungsten head. A clear turn separation in the beam pattern for the flat-top acceleration (FT ON) was observed, while weak separation was seen in the ordinary acceleration without flat-top (FT OFF). The extraction efficiencies are 86 % and 59 % for the flat-top ON and OFF, respectively as shown in Fig. 4. It has been confirmed that the single-turn extraction with the flat-top acceleration is very useful technique to improve the extraction efficiency and reduce the radioactivity for the large scale AVF cyclotron that has the number of turns over 500.

References

1) M. Fukuda, S. Kurashima, S. Okumura, N. Miyawaki, T. Agematsu, Y. Nakamura, T. Nara, I. Ishibori, K. Yoshida, W. Yokota, K. Arakawa, Rev. Sci. Instrum. 74 (2002) 2293-2299.

2) S. Kurashima, M. Fukuda, S. Okumura, N. Miyawaki, T. Nara, T. Agematsu, I. Ishibori, K. Yoshida, Y. Nakamura, K. Arakawa, JAERI-Review 2004-025 (2004) 313-315.

3) W. Yokota, T. Satoh, M. Oikawa, T. Sakai, S. Okumura, S. Kurashima, M. Miyawaki, H. Kashiwagi and M. Fukuda, this report

JP0650274

9.4　Measurement of Beam Energy Spread of the JAERI AVF Cyclotron

S. Okumura, N. Miyawaki, S. Kurashima, K. Yoshida, H. Kashiwagi,
M. Fukuda, I. Ishibori, T. Agematsu, T. Nara and Y. Nakamura
Advanced Radiation Technology Center, JAERI

1. Introduction

A focused heavy ion microbeam system using the JAERI AVF cyclotron beam is in development for research in biotechnology and materials science[1]. A beam focusing system with quadrupole magnets is adopted for the microbeam formation. In order to reduce the chromatic aberration in the quadrupole magnets for the beam size of 1 μm in diameter, the energy spread of the beam less than 0.02% is required. A flat-top acceleration system[2] is installed in the JAERI AVF cyclotron for reduction of the energy spread of the beam. We have developed a simple analyzing system to confirm reduction of the energy spread of the extracted beam using the disperse power of an existing deflecting magnet system in the transport line. We aim to achieve the high resolution of beam energy of the order of 0.001%. The new instruments have been installed to the existing beam diagnostic stations located at the object and image positions of the deflecting magnet system, which horizontally bends the beam trajectory. The beam energy spread can be determined by measuring the dispersed beam size at the image. Higher energy resolution can be
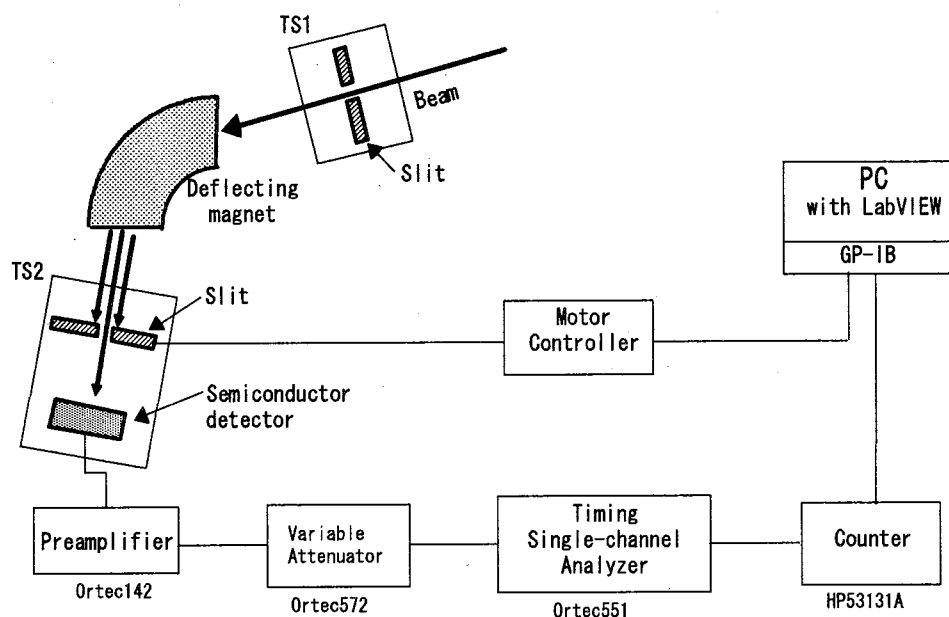
Fig. 1 Schematic diagram of the system for measurement of the beam energy spread. TS1 and TS2 are the existing beam diagnostic stations.
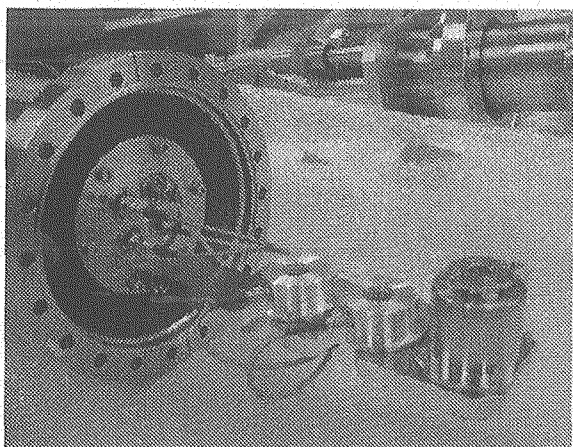
Fig. 2 Beam intensity monitor in the beam diagnostic station TS2. Two semiconductor detectors and a Faraday cup are mounted on the movable stage.

Fig. 3 Measured beam intensity distribution. The origin of the slit position is the center of the slit gap. A position difference of 1 mm corresponds to a relative energy deviation of 0.1 %.

obtained by decreasing the object beam size and determining the image beam size precisely[3]. For the analyzing power of this deflecting magnet system, a slit width of 0.01 mm is required to obtain an energy resolution of $\Delta E/E$ = 0.001%. The intensity distribution of the dispersed beam, which represents the energy spectrum, can be obtained by scanning the image slit position. While the beam intensity, which passes through the slit gap, can be measured with a Faraday cup at a slit width of more than 1 mm, lower intensity beam at a narrow slits width of less than 1 mm has to be measured with an ion detector, such as a semiconductor detector.

2. Measurement system

The system for measurement of the beam energy spread is shown in Figure 1. For definition of the beam size in horizontal direction, two sets of slits, which can be positioned with a

precision of the order of 1 μm, is mounted on the beam diagnostic stations, TS1 and TS2 at the object and the image points, respectively. In the station TS1, the beam is transported through the slit gap to define the object beam size. Then, the beam is dispersed in the deflecting magnet system. A portion of the beam, which passes through the image slit, is detected by a beam intensity monitor in the station TS2 (Fig. 2). The beam intensity monitor is equipped with two semiconductor detectors and a Faraday cup. We can choose an instrument according to the beam intensity by changing the stage position of the beam intensity monitor. The beam intensity distribution is obtained by moving the position of the image slit. This procedure is automatically executed with a personal computer, motor controller, and signal processing devices, as shown in Figure 1.

3. Results

The measurement with an energy resolution of 0.01% was carried out using a 260 MeV $20Ne^{7+}$ beam with the flat-top acceleration. The gap of 0.1 mm was applied to both the object and the image slits. The intensity of the beam passing through the image slit gap, was measured with the semiconductor detector and the beam intensity distribution was obtained by moving the position of the image slit in steps of 0.1 mm. Figure 3 shows an example of the beam intensity distribution. A fine structure of the beam energy distribution can be observed. This result shows that the system provided the expected energy resolution of 0.01%.

References

1) M.Oikawa, T. Kamiya, M. Fukuda, S. Okumura, H. Inoue, S. Masuno, S. Umemiya, Y. Oshiyama, Y. Taira, Nucl. Instr. and Meth. B 210 (2003) 54-58.

2) M. Fukuda, S. Kurashima, S. Okumura, N. Miyawaki, T. Agematsu, Y. Nakamura, T. Nara, I. Ishibori, K. Yoshida, W. Yokota, and K. Arakawa, Rev. Sci. Instrum. 74 (4) (2003) 2293-2299.

3) F. Hinterberger, P. v. Rossen, R. Jahn and B. Schüller, Nucl. Instr. and Meth. 130 (1975) 347-352.

JP0650275

9.5 Use of GAF-film and PC-scanner for Easy High-resolution Measurement of Ion Beam Fluence Distribution

T. Agematsu and H. Hanaya
Advanced Radiation Technology Center, JAERI

1. Introduction

Various type of film dosimeters are used to measure two-dimensional (2-D) fluence distribution of wide area ion beam irradiation. The CTA[1,2] film dosimeter is a typical film dosimeter which has high spatial resolution. However, a special spectrum photometer is necessary to measure 2-D optical density distribution of CTA film, for example CS-9000 (Shimadzu Co.), which is expensive, difficult to handle and takes a long time to complete measurement.

We examined a combination of Gaf-chromic film dosimeter (GAF film) and an image scanner for a personal computer (PC-scanner) as a 2-D densitometer which is cheap, easy to use and allows speedy measurement with high spatial resolution. There are reports[3,4] of the gamer-ray dose distribution measurement using GAF film and a PC-scanner for medical use. We applied this technique to measurement of the 2-D distribution of ion beam fluence.

2. Merit of GAF film and PC-scanner

The technique using a fluorescent screen and a CCD camera is sometimes used to measure ion beam 2-D distribution because it permits easy real-time measurement. However there are some problems such as a) spatial limit in setting position and angle of camera, b) luminosity decrease due to coloring of the screen by ion beam irradiation damage, c) short exposure time of a usual CCD camera, which is not applicable to long irradiation such as raster scanning type wide area irradiation. At the JAERI AVF cyclotron, several minutes are taken for wide area irradiation made by scanning ion beam two-dimensionally more than ten times.

On the other hand, integral type film dosimeter with high spatial resolution is useful. We selected GAF film HD-810 (nominal dose range 10-400Gy) in this study, because GAF film can be found on the market more easily than CTA film, radio-activation is lower compared to CTA film (nominal dose range 10k-160kGy) because high sensitivity, the available dose range of GAF film meets the ion beam irradiation of the bio-technology, for example, ion beam breeding of plant for new mutant production performed at the HY scanning beam line. Furthermore, it is merit that we can observe coloring of GAF film in real-time by irradiation.
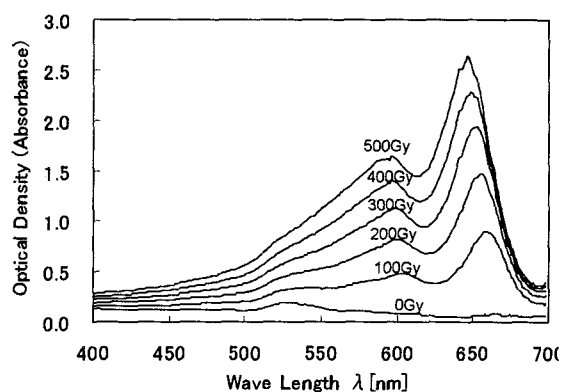
Fig. 1 Optical density spectrum of GAF film irradiated by 2MeV electron beam measured with spectrum photometer CS-9000.

2.1 Linearity of dose response

We made sure that the dose response linearity of the GAF film and a PC-scanner was

satisfactory by comparing to CS-9000. The GAF film irradiated with 2MeV electron beam, which is expected to give the film a similar dose response to ion beam irradiation[5]. We took at first the optical density spectrum of the irradiated film with CS-9000 in order to check the dose response. Figure 1 shows the measured spectrum. The dose response at 580nm wave-length, where the signal strength is large enough, is described in Fig. 2 and the linearity is good.

We used LiDE50 (Cannon) as a PC-scanner in this study. The dose response measured with the PC-scanner for the same irradiated GAF film is shown in Fig. 2. We see linearity as good as with CS-9000 up to 200Gy for R(red), 300Gy for G(green) and 500Gy for B(blue) component. We can use the PC-scanner in wide dose range by selecting the component.
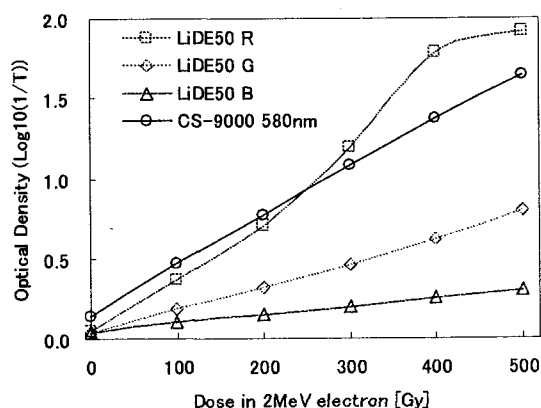
Fig. 2 Dose response of GAF HD-810 with CS-9000 (580nm) and with a PC-scanner with RGB component for 2MeV electron beam.

2.2 Data processing

We obtained a 2-D optical density map of the GAF film according to the following process. The first step is image scanning of the GAF film using a PC-scanner. The 2nd step is a translating scanner data to numerical value of RGB component with the free-software BMP2CSV. The 3rd step is calculating the

optical density (O.D.), O.D. = $Log_{10}(1/Transmition) = Log_{10}(2^8/value\ of\ RGB)$, with the software MS-Excel. The 4th step is drawing a 2-D map with calculated O.D. data with the free-software GraphR161.

3. Example of measurement

There are the ion beam scanners of raster scanning type for large area and high uniformity irradiation at the beam lines of the JAERI AVF cyclotron. We sometimes measured low uniformity in 2-D fluence distribution which showed clear lines in the beam scanning trajectory as seen in Fig. 3.

We supposed that the low uniformity was caused by a sharp peak of fluence in a beam spot. Then we used LiDE50 PC-scanner and GAF film to prove it by measuring a 2-D fluence distribution of a 320MeV $^{12}C^{6+}$ beam spot with high spatial resolution. The measured data are shown in Fig. 4 comparing the 2-D distributions obtained with CS-9000 (580nm) and LiDE50. The spatial resolution of CS-9000 is 0.4mm and that of LiDE50 is 0.021mm (1200dpi). The LiDE50 clarified that there was a very sharp concentration of fluence in a beam spot and it caused the low uniformity.
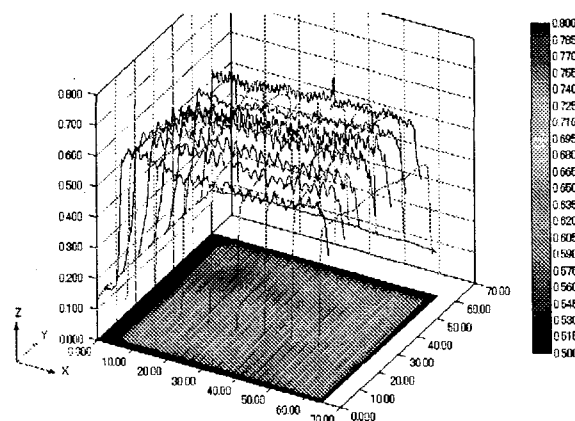
Fig.3 Two dimensional optical density distribution of GAF film. The film was irradiated by $^{12}C^{6+}$ 320MeV ion beam at HY scanning beam line.

4. Summary

Everyone can measure high resolution 2-D distribution of ion beam fluence by using GAF film and a PC-scanner without special 2-D spectrum photometer. The detail of specification of a PC-scanner, wave-length and spectrum of lamp for example, how to separate to RGB component and how to calculate RGB value by the software are often unknown. They depend on a model of a PC-scanner. But this problem can be solved by measuring the linearity of a PS-scanner using irradiated GAF film. If we use an up-to-date model PC-scanner or a PC-scanner for 35mm-film, higher spatial resolution than LiDE50 is available. The highest spatial resolution of GAF film is reported to be 1μm[5].

The MD-55 GAF film is good for lower fluence beam. If ion beam energy is enough high to have a long range in GAF film, we can use multi-layer stack GAF film for low fluence.

It is known that GAF film[6] has dependence of dose response linearity on temperature and humidity. Therefore, we need to study the dependence for precise measurement.

References

1) T. Agematsu, S. Okumura and K. Arakawa, JAERI-Conf 95-003 (1995) 467-471

2) R. Tanaka, S. Mitomo, H. Sunaga, K. Matsuda and N. Tamura, JAERI-M 82-033 (1982)

3) Slobodan Devic, J. Seuntjens, G. Hegyi and E. B. Podgorsak, Med. Phys. 31(9) (2004) 2392-2401.

4) M. A. Stevens, J. R. Turner, R. P. Hugtenburg and P. H. Butler, Phys. Med. Biol. 41 (1996) 2357-2365.

5) T. Kojima, H. Sunaga, H. Takizawa, H. Hanaya and H. Tachibana, Radiat. Phys. Chem. Vol. 68 (2003) 975-980.

6) Zhongying Li, Dezhi Wen, Dahua Chen, Shouyong Peng, Lu Zhang and Kequin Shin, Radiat. Phys. Chem. Vol. 57 (2000) 103-113.
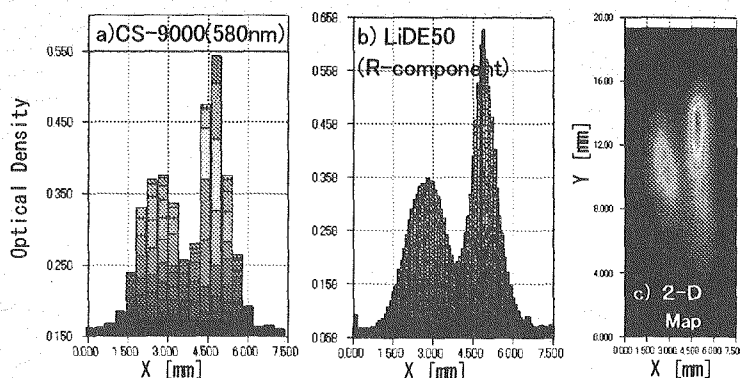
Fig. 4   Example for measurement of 320MeV $^{12}C^{6+}$ beam spot. a) obtained with CS-9000, b) with the PC-scanner plotted at 0.1mm resolution, c) 2-D map of the beam spot with the PC-scanner.

JP0650276

9.6 Development of Beam Generation and Irradiation Technology for Electrostatic Accelerators

A. Chiba, S. Uno, K. Ohkoshi, K. Yamada, Y. Saitoh,

Y. Ishii, T. Sakai, T. Satoh and K. Mizuhashi

Advanced Radiation Technology Center, JAERI

1. Development of beam current stabilization system

A stabilization system of beam current using a wire type beam attenuator was developed in order to keep the on-target beam current constant during an experiment[1]. The conventional system is controlled with referencing the target current, but it is not available for some experiment in which the on-target current can not be measured. Therefore, the new system is equipped with a mesh (93.7% permeability) type beam current monitor which is installed between the attenuator and the target. The schematic picture of the system is shown in Fig.1.
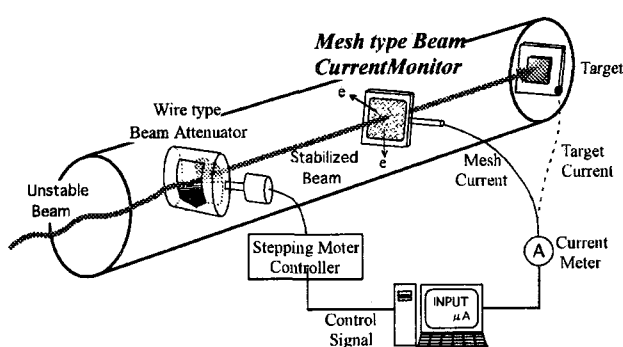
Fig.1 Schematic picture of beam current stabilization system.

The linearity of the current from the mesh was measured as follows. The mesh type beam monitor was installed in front of a Faraday cup (FC) in the beam line of the Ion Implanter, and

the current from the mesh was measured for the H^+ and Ar^+ beam with the FC. Figure.2 shows the measured current with the mesh as a function of that with the FC. Although the current measured with the mesh is different by energy and ion species, but the linearity is good enough for the beam current stabilization. The target current is controlled with the fluctuation of several % by this system.
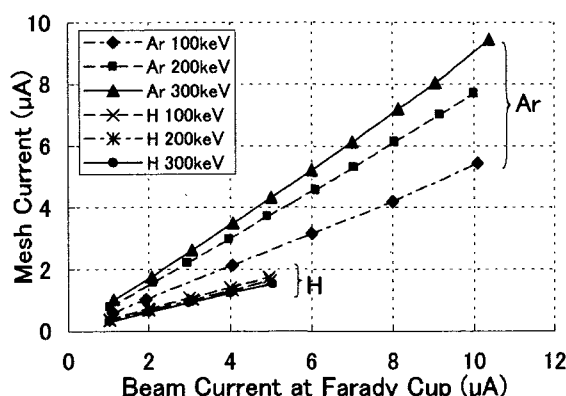
Fig.2 Relationship between FC current and mesh current.

2. Multiply charged metallic ion production for ion implanter

To increase maximum beam energy to higher than 1MeV for the ion implanter, we have installed the compact ECR ion source (ECRIS) in the implanter, which was developed at TIARA to produce multiply charged ions from gaseous samples (e.g. He, N, O, Ne, Ar, and Xe). At

present, irradiation of those ion beams in MeV energy region is possible with the implanter. In order to expand available ion species, we tried producing multiply charged metallic ions with the ECRIS using the MIVOC method [2]. In the MIVOC method, vapors of volatile compounds including metallic atoms are used to release metallic elements into plasma. In this time, we used ferrocene ($Fe(C_5H_5)_2$) to generate iron ion, which is useful for surface modification of ceramics. Ferrocene was placed in a separate vacuum chamber connected to the plasma chamber. The vapor of the compounds diffuses into the chamber at room temperatures. The schematic picture of the MIVOC method is shown in Fig.3. The vapor flow rate was controlled by a variable leak valve and optimized for each charge state of iron ions. As a result, we obtained iron ion beams more than $1e\mu A$ for up to 6+ with the microwave power of 10 W. Table 1 shows the obtained current of iron beam accelerated by the voltage of 350kV.

3. Voltage calibration of the 3MV single-ended accelerator after replaced the voltage measurement resistance

The 3 MV single-ended accelerator was designed to achieve the high voltage stability of $\pm 1 \times 10^{-5}$ using a symmetrical Shenkel circuit. The stability is inevitable for the formation of a submicron size beam. Production of ion beam with high position stability and narrow energy spread is necessary to form the micro-beam using a magnetic focusing lens system. In order to obtain the high voltage stability, the high voltage needs to be measured at the high accuracy with the highly-precise resistance. The resistances are, however, often damaged by terminal discharges, so that their resistance values are changed. Therefore various resistances were tested to develop a discharge tolerant resistance (Fig.4). The non-inductive $120M\Omega$ resistances with the accuracy and temperature coefficient of 1% and 25 ppm/°C, respectively, were developed and were substituted for the old resistance. The acceleration voltage of up to 3MV is measured with 220 resistances connected in series (26.4GΩ).

Fe(C$_5$H$_5$)$_2$

Micro-wave

Fe

Variable Leak Valve

ECR Ion Source

Room Temperature

Formula Weight : 186.04g/mol
Melting Point : 174-176°C
Boiling Point : 249°C

Fig.3 Schematic picture of the MIVOC method.
Table 1 Beam intensity of Fe^n obtained with the ECRIS.

	Fe^{1+}	Fe^{3+}	Fe^{5+}	Fe^{6+}
Beam intensity (eμA)	2.2	1.7	2.4	3.6
Beam energy (MeV)	0.35	1.05	1.75	2.1
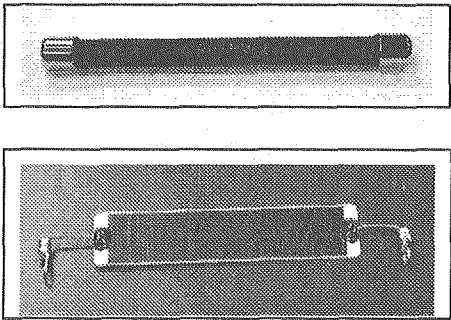
Fig. 4 The resistances used for the high voltage measurement. The top is the previous resistance and the bottom is the developed resistance.

The measured voltage with the new resistance was calibrated using a nuclear resonance reaction of Al(p,γ)Si with the resonance width of 100eV, after the 220 resistances were replaced. The ratio of accelerator controller indication voltage to the nuclear resonance reaction energy of 992keV was 100.35% from the measurement results. The beam energy spreads at the reaction energy was 4.3×10^{-4}.

These values are equal to the ones before the measurement resistances were replaced. The accelerator is more stably operated than before the resistances were replaced.

4. Improvement on micro-beam scanning systems for beam writing applications

At TIARA electrostatic accelerators facility, two scanning ion micro-beam systems have been operated for various applications. The light ion micro-beam system is mainly used for elemental analysis by PIXE and PIGE techniques. On the other hand, the heavy ion system, combined with a single ion irradiation technique, is a unique tool for single event study on semiconductor devices. In both systems, micro-beam scanning is controlled by PC-based systems. Main functions of the PC systems are secondary electron imaging for focusing-parameter tuning, uniform and spot

irradiation, such as micro-PIXE technique for elemental analysis and/or studies for single event effects in semiconductor devices. Figure 5 illustrates schematic diagram of the micro-beam scanning system.

Recently, a beam writing function, that enables preset pattern irradiation onto the sample, has been combined with the beam scanning systems. One of the promising applications is micro-machining fabrication technique[3]. Preliminary study for micro-machining has been started and first maskless lithographic experiments succeeded.
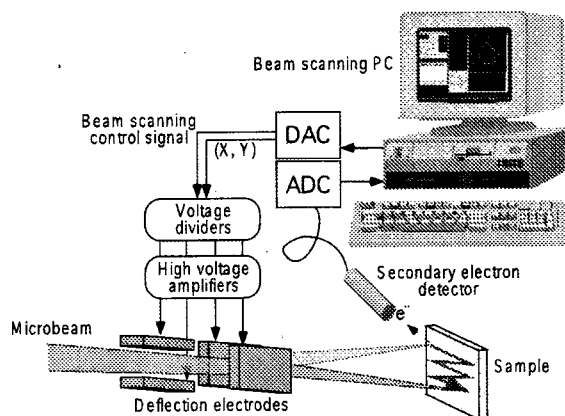
Fig. 5 Schematic diagram of the ion micro-beam scanning system.

Reference

1) K. Ohkoshi, A. Chiba, K. Mizuhashi, W. Yokota, JAERI-Review 2004-025, 324-325

2) H.Koivisto, J.Ärje and M.Nurmia, Nucl. Instr. and Meth. B94 (1994) 291

3) J. L. Sanchez, J. A. van Kan, T. Osipowicz, S. V. Springham and F. Watt, Nucl. Instr. and Meth. B136-138 (1998) 385-389.

JP0650277

9.7   Power Consumption of Cyclotron System and Takasaki Site

Y. Nakamura*, S. Kurashima*, W. Yokota*, T. Nara*, K. Takano**,
H. Takada** and J. Yoshii***
Advanced Radiation Technology Center, JAERI*,
Beam Operation Service, Co., Ltd. **,
Utilities and Maintenance Division, JAERI***

1.   Introduction

Especially in recent years, many environmental subjects, such as reducing the discharge of carbon dioxide, saving electric power and paper resources, have been pointed out from the viewpoint of global aspects. In Japan, the Ministry of Economy, Trade and Industry guides that more than 1 % of consumed electric power should be reduced every year, and the ISO14001 at Takasaki site has decided the 1 % reduction of power consumption per year. Now the Takasaki site, which has been designated to the energy control factory of first class, has begun to energetically make self-effort for the power saving in 2004.

2.   Electric power consumption

2.1   General consumption in Takasaki site

As shown in Table 1 for recent five years, the average yearly power consumption in the TIARA facility and the Takasaki site is 19.3 and 11.5 GWh, respectively. The power consumption appears to be very stable. The

Table 1   Power consumption in the TAIRA facility and Takasaki site.

Fiscal year (Jap.)	Takasaki	TIARA	Ratio	Remark
1999 (H11)	17.07	11.34	0.664	Unit : GWh
2000 (H12)	19.59	11.83	0.604	Venture building
2001 (H13)	19.64	11.60	0.591	
2002 (H14)	19.10	11.30	0.592	
2003 (H15)	19.01	11.24	0.591	
2004 (H16)	19.10	11.51	0.603	Power saving

TIARA facility accounts for the 60 % of total quantity in the Takasaki site.   The similar tendency in the power consumption between the Takasaki site and the TIARA facility is clearly shown in Fig. 1.   Furthermore in warm season, the similar tendency is also observed between the total power consumption in Takasaki site and the average atmospheric temperature at Maebashi next to Takasaki.

Therefore, we foresee that an empirical formula of the power consumption can be expressed by a function of average temperature
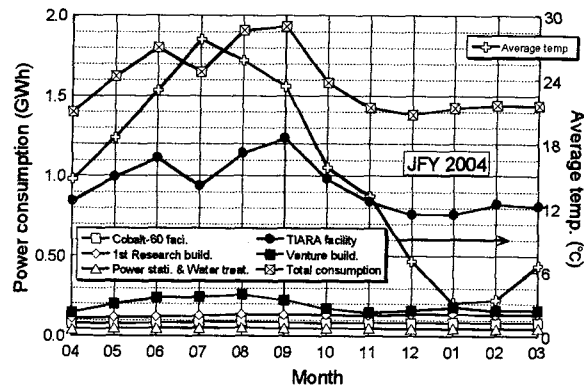
Fig. 1 Change of power consumption and average temperature through a year in the Takasaki site.

and the operation time of the cyclotron system[1-2]. In order to exactly estimate the effect of the electric power saving, a reliable formula is required to accurately predict the actual power consumption.

2.2   Power consumption through seasons

Based on the data from 2000 to 2003, the average power consumption in the TIARA facility during the operation of the cyclotron system needs to be estimated at first.   The relationship between monthly operation time of the cyclotron system and the power consumption in the TIARA facility is shown in Fig. 2.   The average consumed power in cool season from November to April is estimated at 852 kW under the cyclotron operation from this figure.   In actual operation of cyclotron
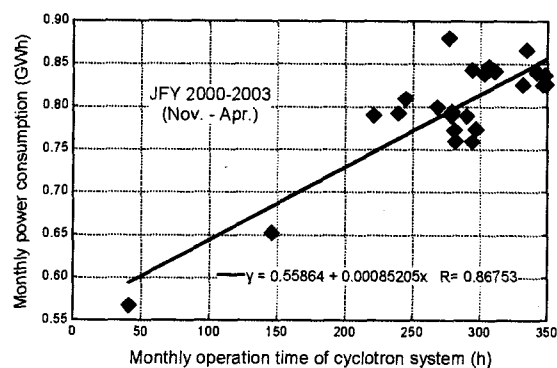
Fig. 2   Relationship between operation time of the cyclotron and the power consumption.

system, the power consumption strongly depends on the main coil current which roughly correlates to ion species as shown in Fig. 3. And the invariable base load of power consumption for one month was also calculated at 1.18 GWh based on the data through cool
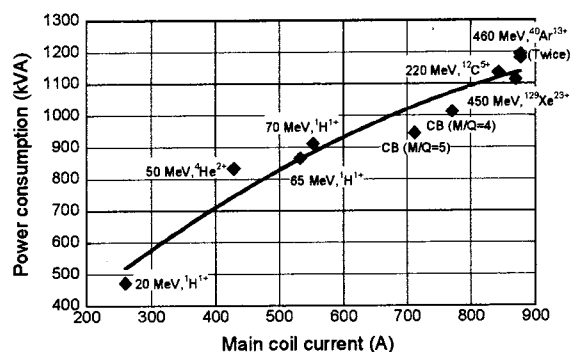
Fig. 3 Dependence of power consumption on the main coil current under cyclotron operation.

season in the Takasaki site.

On the other hand in warm season from May to October, the atmospheric temperature greatly affected the power consumption as shown in Fig. 4 because of the use of air conditioning devices. The quadratic formula was given from the relationship between the average temperature at Maebashi and the power consumption in Takasaki site.

2.3 Emprical formula

Finally, the empirical formulae to estimate the power consumption (P_m) in unit of GWh for one month are written in the following separate expression for cool and warm season,

$$P_m=8.52\times10^{-4}t_{CYC}+1.18 \quad \text{(Nov-Apr)},$$
$$P_m=2.50\times10^{-3}T^2-5.13\times10^{-2}T$$
$$+8.52\times10^{-4}t_{CYC}+1.46 \quad \text{(May-Oct)},$$

where T is average atmospheric temperature (°C), t_{CYC} is the operation time of cyclotron system (h), respectively. If the average temperature is 25 °C, the temperature coefficient is estimated at 73.7 MWh/°C as the derivative $(\partial P_m/\partial T)$ is expressed as $5.00\times10^{-3}T-5.13\times10^{-2}$.

2.4 Estimation of power saving in 2004

With a view to evaluating the effect of the power saving in 2004, Table 2 shows the average temperature at Maebashi, operation time of cyclotron system, actual and estimated power consumption of every month. The estimated values in Table 2 are given by the above mentioned formulae.

The total power consumption in 2004 is
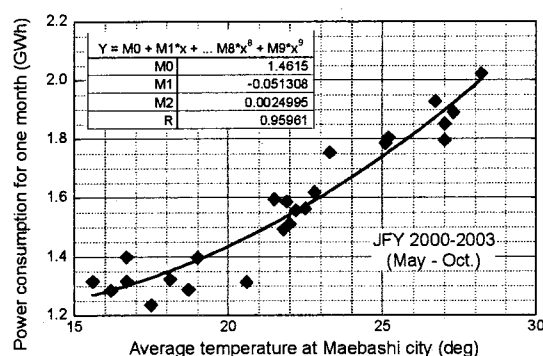
Fig. 4 Temperature dependence on monthly power consumption in Takasaki site.

estimated at 19.7 GWh unless the measures for the power saving are performed effectively. Our effort for power saving is estimated at 3 %, which is rather larger than our goal of 1 %.

An example of the comparison between 2003 and 2004 for the power consumption is described as follows. The total actual power consumption of 19.1 GWh in fiscal year 2004 is slightly greater than the amount of 19.0 GWh in 2003 as shown in Table 1. However, the average temperature at 22.4 °C through warm season from May to October was high 1.4°C which was equal to the power increment of 510 MWh. And yearly operation time of cyclotron system was also long 73.1 hours. Taking into account these conditions, the certain effect for the power saving in 2004 is clarified.

2.5 Power consumption of cyclotron system

Nine trunk power lines and their principal loads in the TIARA facility is listed in Table 3.

Table 2 Power consumption in the Takasaki site in fiscal year 2004.

Month	Ave.temp °C	Ope.time h	Power consumption (GWh) Actual	Power consumption (GWh) Estima	Power consumption (GWh) Ratio
Apr	14.7	297.2	1.373	1.43	1.04
May	18.6	331.6	1.641	1.65	1.01
Jun	23.0	314.8	1.880	1.87	1.00
Jul	27.8	214.0	1.941	2.15	1.11
Aug	25.8	179.3	1.863	1.95	1.05
Sep	23.4	345.1	1.890	1.92	1.02
Oct	15.8	286.1	1.514	1.52	1.00
Nov	13.1	314.6	1.423	1.45	1.02
Dec	7.0	269.6	1.380	1.41	1.02
Jan	3.1	288.3	1.387	1.42	1.03
Feb	3.4	364.9	1.409	1.49	1.06
Mar	6.6	249.6	1.398	1.39	1.00
Average	15.2	287.9	1.592	1.64	1.03
Total		3455.1	19.10	19.7	

Five lines of them from A to F line with the exception of B line feed the electricity to the cyclotron system.

Practically, it is rather difficult to exactly estimate the actual power consumption for the cyclotron system because many loads without the cyclotron system are connected to the same line. The power consumption through A line is the biggest part in the cyclotron system.

3. Power saving by ventilation system stop

An efficient power saving is to stop as long as possible the power devices which are operated continuously even on holidays, such as ventilation and air conditioning systems. The rooms for the power supplies and ion sources were chosen to examine the power saving. Many C-C thermocouples were put in the power supply boxes and at other places in both rooms. In the power supply boxes, the thermocouples were also set near the device controllers including many semiconductor elements which are highly sensitive against the temperature.

The temperature measurement was continued while the ventilation systems were stopped for several weekends. As a result, the temperature rise about 4-5°C in the boxes for the weekend was almost same as the maximum one during the cyclotron operation as shown in Fig. 6. For fiscal year 2004, we stopped simultaneously the ventilation systems in both rooms for 22 weekends. Total electric power and stopping time for these systems are 39 kW
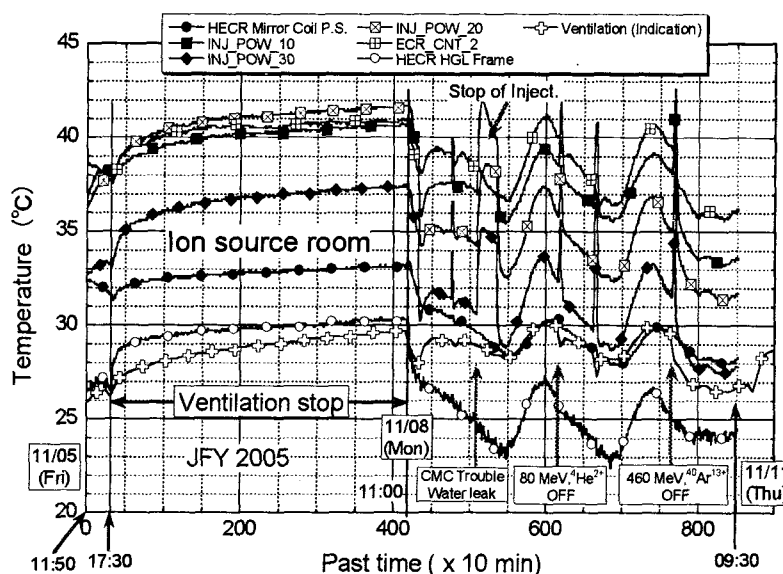
Fig. 6 An example of temperature measurement in ion source room.

and 1499.7 hours, respectively. The power saving by this measure was evaluated at 58.5 MWh which corresponds to 31 % of our goal for a year in Takasaki site.

Summary

The power consumption in the Takasaki site for one month was expressed first by the simple empirical formulae. As a result, we have made it possible to easily estimate the effect for the power saving and to predict the amount of the power consumption.

References

1) Y. Nakamura, T. Nara, T. Agematsu, *et al.*, TIARA Annual Report 2003 (JAERI -Review 2004-025) (2004) 310-312
2) Y. Nakamura, T. Nara, T. Agematsu *et al.*, Proc. 4th Int. Workshop on Accel. Opera., Kanagawa and Ibaraki, Japan (2003) 8-13
3) Y. Nakamura, W. Yokota, S. Okumura, *et al.*, JAERI-M 95-054 (1994) 61 pages.

Table 3 The content of principal electric loads connected from A to I lines.

Lines	A	B	C	D	E	F	G · H · I
Name of line	F2-03	F2-04	F2-05	F2-06	F2-07	F2-07	F2-08
Voltage (V)	420	420	210	210	210/105	210/105	420/210/105
Cyclotron system	Cyclotron		Ion source,Inject.	Vacuum	Control	Cont. rack	Door
	Beam transp.		Cooling (All)	(Cyclo., BT)		Cooling	
	HECR (Anal.,Glaz.)		HECR (Mirr. coil, Micro wave, Vac)	S-chopper		Ion source	Radia. monit.
				Beam scanner			
	Grad. Correct.		Cooling (Stabil.)				
Electrostatic Accelerator			Tandem accel.	Single-end accel.	Control (Tandem)	Contlol (Others)	Door
				Ion implanter			Radia. monit.
Ventilation & lighting		Ventil. Air-condit.	Distributor board	Distributor board	Distri. board	Distri. board	Emerg. light.
		Water cooling			Lighting	Lighting	Lighting
	Drainage	Drainage					Radia. monit.

This is a blank page.

10. Status of TIARA 2004

This is a blank page.

JP0650278

10.1   Utilization of TIARA Facilities

Su. Tanaka*, K. Nishimura*,Y. Nakamura*, H. Kaneko*, M. Hosono*,

H. Watanabe**, H. Tachibana**, S. Mochizuki**, S. Kaneya**,

K. Daikubara***, M. Kawabata** and M. Iijima**

Advanced Radiation Technology Center, JAERI*

Radiation Application Development Association**

Research Center for Nuclear Science and Technology, The University of Tokyo***

1. Introduction

TIARA is a center of the ion accelerator facilities composed of four ion accelerators, the AVF cyclotron, the 3MV tandem accelerator, the 3MV single-ended accelerator, and the 400kV ion implanter. These accelerators have been fully served for ion beam applications since January 1994.

2. Utilization system

TIARA is opened for public use: it receives applications of the experimental subjects in wide research field in Japan once a year from outside users as well as JAERI staffs. The subjects and the allocated beam time are approved after the official investigation by Subcommittee for TIARA under Advisory Council for JAERI's Research Facilities, which has been organized since 1999. To attain an effective outcome of the research program, the beam time of each accelerator is fairly allotted to the subjects three times in a year based on the approved beam time.

Charges for the utilization are remitted in the case that a contract of the joint research between JAERI and a university or a company or that of the projective joint research between JAERI and universities is made. However, the results of research have to be published at the TIARA Research Review Meeting and in the JAERI TIARA Annual Report. There is another system of joint-use with charges but

without the publication duty.

3. Experimental subject approved

The number of experimental subjects using cyclotron approved in FY2004 was 70 and the total number using three electrostatic accelerators was 59 as shown in Table 1. Table 2 shows the number allotted to users under various contracts.

Fig. 1 shows the change in the number of experimental subjects in various research fields from FY1991 to FY2004.

4. Allotted time to users

The cyclotron has been continuously operated from Monday to Friday. The utilization time for the cyclotron is allotted in units of an hour. In the case of the electrostatic accelerators, on the other hand, the utilization time is allotted by the day either from 9 a.m. to 7:30 p.m. (A mode), or from 9 a.m. to 10 p.m.(B mode).

As shown in Table 3   and Fig. 2, the cyclotron was used in the various research fields, while the electrostatic accelerators were mainly used in the field of inorganic materials and materials for fusion. The ratios of allotted time for JAERI staffs to total utilization time were 32% for the cyclotron and 41% for the electrostatic accelerators as shown in Table 4 and Fig. 3.

Table 1 Number of experimental subjects in FY2004 at various research fields.

Fields of research	Cyclotron	Electrostatic accelerators
Materials for space	7	8
Materials for fusion	0	6
Biotechnology	51	4
Inorganic material	0	23
RI & nuclear sci.	2	0
Organic material & Radiation chemistry	6	2
Basic technology	4	16
Total	70	59

Table 2 Number of experimental subjects in FY2004 at various relations with users.

Relations with users		Cyclotron	Electrostatic accelerators
JAERI only	Takasaki Establishment	15	11
	Others	1	7
Cooperative research with university		19	6
Joint research project		22	16
Joint research with private company or governmental institute		13	19
Total		70	59

Table 3 Utilization of the accelerators in FY2004 in various research fields.

Fields of research	Cyclotron (hours)				Tandem accelerator(days)				Single-ended accelerator(days)				Ion implanter (days)			
	04-1	04-2	04-3	total	04-1	04-2	04-3	total	04-1	04-2	04-3	total	04-1	04-2	04-3	total
Material for space	195	194	142	531	22	16	10	48	9	3	0	12	12	17	11	40
Material for fusion	0	0	0	0	7	10	7	24	6	8	7	21	6	4	4	14
Biotechnology	384.5	371.5	170	926	1	2	3	6	0	0	5	5	0	0	0	
Inorganic material	0	0	0	0	9	12	12	33	20	14	22	56	24	19	16	59
RI & nuclear science	18	14	10	42	0	0	0	0	0	0	0	0	0	0	0	0
Organic material & Radiation chemistry	90	88.5	54.5	233	2	3	3	8	0	0	0	0	0	0	1	1
Basic technology	77	121	73	271	12	8	6	26	14	29	12	55	5	0	0	5
Machine study	113	117.5	80	310.5	1	1	5	7	4	4	0	8	2	3	5	10
Joint-use	66	66.5	115.5	248	2	3	1	6	0	0	1	1	2	7	6	15
Total	943.5	973	645	2561.5	56	55	47	158	53	58	47	158	51	50	43	144

Table 4 Utilization of the accelerators in FY2004 in various relations to be various types of use.

Relation with users		Cyclotron (hours)				Tandem accelerator (days)				Single-ended accelerator(days)				Ion implanter (days)			
		04-1	04-2	04-3	total	04-1	04-2	04-3	total	04-1	04-2	04-3	total	04-1	04-2	04-3	total
JAERI Only	Takasaki Establishment	246	240.5	155.5	642	27	19	15	61	18	14	8	40	18	8	12	38
	others	3	0	12	15	3	0	2	5	6	5	3	14	4	3	2	9
Cooperative research with universities		160	191	80	430.5	5	8	6	66	6	3	14	23	12	12	11	35
Joint research project		198	183.5	130	511.5	4	7	5	16	3	3	5	11	4	12	2	18
Joint research with company or governmental institute		158	174	72	404	14	17	13	44	16	29	16	61	9	5	5	19
Machine study		113	117.5	80	310.5	1	1	5	7	4	4	0	8	2	3	5	10
Joint-use		66	66.5	115.5	248	2	3	1	6	0	0	1	1	2	7	6	15
Total		943.5	973	645	2561.5	56	55	47	158	53	58	47	158	51	50	43	144

Number of experimental subjects at various research fields
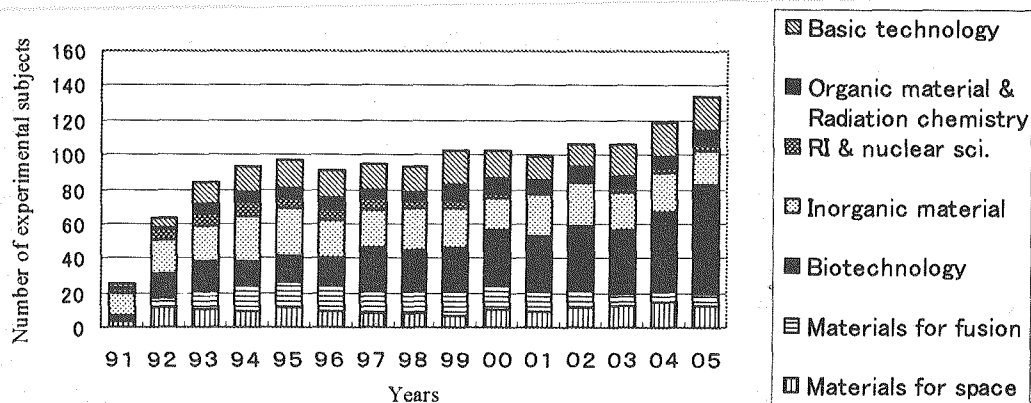
Fig. 1 The change of number of experimental subjects in various research fields.
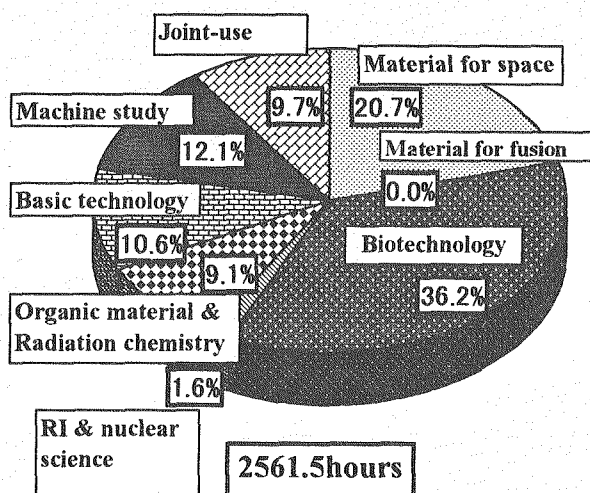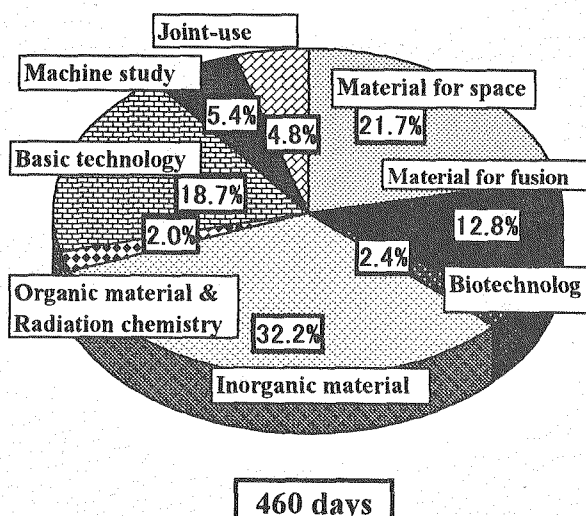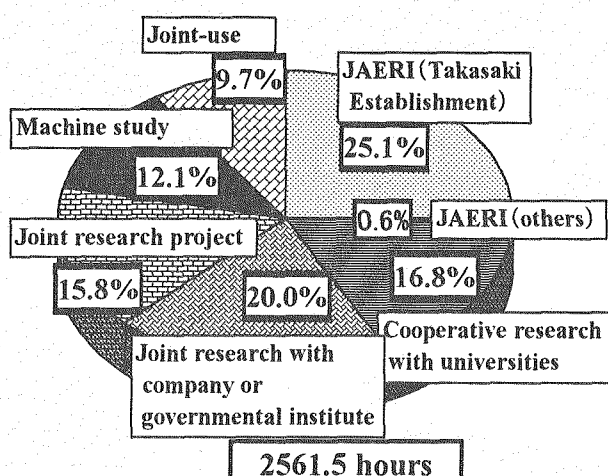
Fig. 2 Utilization of the accelerators in FY2004 in various research fields.
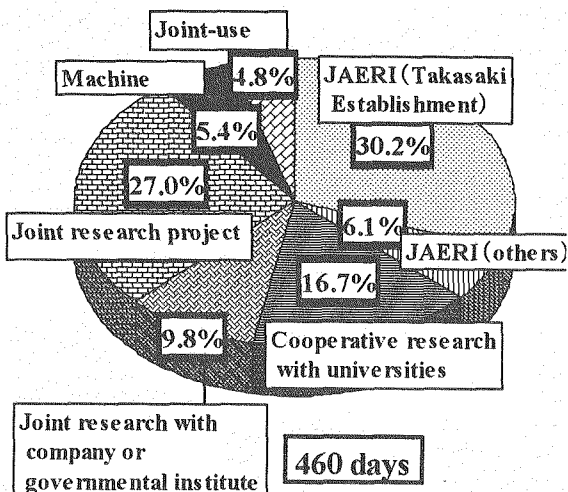
Fig. 3 Utilization of the accelerators in FY2004 in relation to the various types of user.

10.2　Operation of JAERI AVF Cyclotron System

T. Nara*, T. Agematsu*, I. Ishibori*, S. Kurashima*, K. Yoshida*,
M. Fukuda*, S. Okumura*, N. Miyawaki*, H. Kashiwagi*, Y. Nakamura*,
W. Yokota*,　K. Akaiwa**, To. Yoshida**, S. Ishiro**, Y. Arakawa**,
Tu. Yoshida**, S. Kanou**, A. Ihara** and K. Takano**

Advanced Radiation Technology Center, JAERI*
Beam Operation Service, Co., Ltd.**

The JAERI-AVF cyclotron system has been smoothly operated since the first beam extraction in March 1991. Figure 1 show the yearly operation time, which is increasing after 2001. The total operation time in FY 2004 amounted to 3455 hours which is the longest so far.
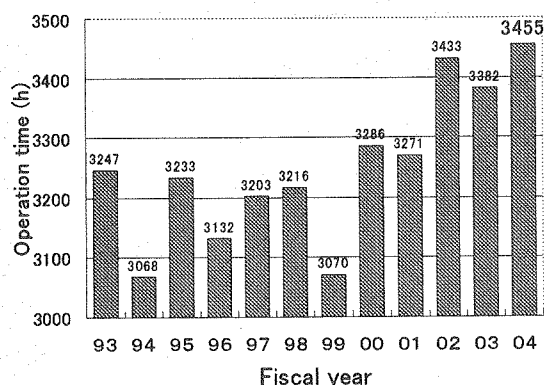
Fig. 1.　Yearly operation time since 1993.

The monthly operation time is shown in Fig. 2. The percentages of operation time of the year used for experiments, machine tuning, beam development, joint-use, and machine study were 62.8%, 18.9%, 1.4%, 7.1%, and 9.7%, respectively. Thirty-three kinds of ion species
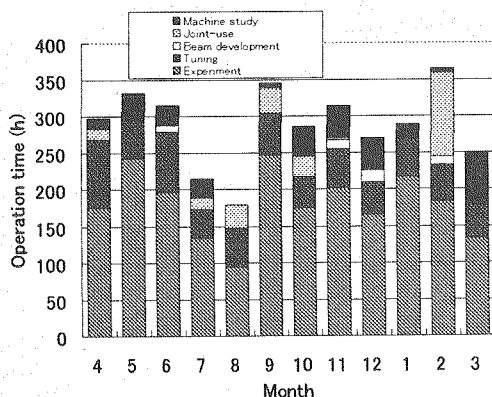
Fig. 2.　Monthly operation time in FY2004.

were delivered for various experiments.

Figure 3 shows beam time of major ions used for experiments. Heavy ions (including cocktail beams) accounted for 72.3 % of the total time.
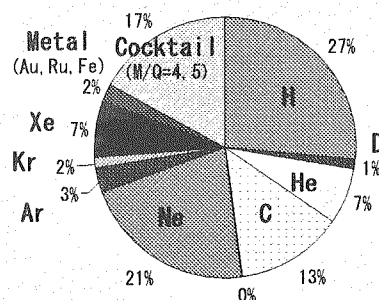
Fig. 3.　Percentages of accelerated ion species in FY2004.

The beam acceleration tests were carved out for 38MeV H^+, 454MeV $^{129}Xe^{25+}$ (cocktail M/Q=5 series) and 560MeV $^{129}Xe^{26+}$, and they were used for research experiment.

The regular yearly overhaul was carried out for four weeks in summer, and the routine maintenance of power supplies for a week in fall.

The sequence controllers for vacuum and the beam scanner in the first light ion room on the first floor were moved to the cable distribution area on the basement to reduce the radiation damage.

It was several magnets of the HX course in the 1st heavy ion room sinked at most 2mm below the cyclotron level. Their levels were corrected in order to allow rapid and precise beam transportation for micro-beam formation experiment.

JP0650280

10.3 Operation of the Electrostatic Accelerators

K.Mizuhashi*, S.Uno*, K.Ohkoshi*, A.Chiba*, K.Yamada, Y.Saitoh*, Y.Ishii*,
T.Sakai*, T.Satoh*, W.Yokota*, M. Ishii**, T.Orimo**, T.Takayama**, M.Kouka**,
A.Ohmae**,T.Kitano** and S.Kanai**
Advanced Radiation Technology Center, JAERI*
Beam Operation Service, Co., Ltd.**

1. Operation

Three electrostatic accelerators were operated smoothly for various experiments in FY 2004. The total operation time for each accelerator in the year amounts to 1,914.9 hours for the tandem accelerator, 2,490.7 hours for the single-ended accelerator and 1,844.9 hours for the 400kV ion implanter, respectively. Monthly operation time of each accelerator is shown in Fig.1. The rate of application number for offered machine-time number was 136% for the tandem, 123% for the single-ended and 151% for the ion implanter. And the rate of executed experiment for planned it was 96.4%, 96.3% and 101.4%, respectively.
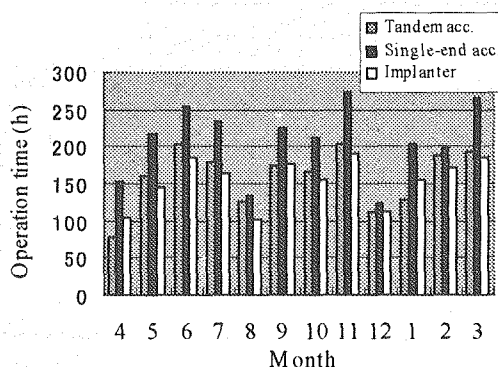
Fig.1 Monthly operation time in FY 2004

2. Maintenance

The SF_6 gas leakage of $28m^3$/year was found at the pressure tank of the tandem accelerator. The SF_6 gas is the global warming material and its warming coefficient is 23,000 times as large as that of the CO_2 gas. By replacing the feedthrough parts on the tank, the leakage was reduced to less than 1/3 (Fig.2). In addition, the SF_6 gas storage tank, the SF_6 gas circulation equipment and the Generating Volt Meter
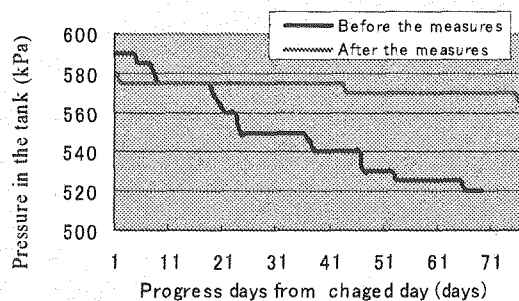
Fig.2 Decrease of the SF_6 gas pressure in the tank of accelerator due to leakage

(GVM) were maintained for the first time since the regular operation of accelerator started.

3. New beams

The beam of 1μ A Sn^- was newly accelerated with tandem accelerator and 4μ A of Li^+ beam generated from LiF was accelerated with the ion implanter for development of the P-type semiconductor.

4. Development

The voltage stability of the tandem accelerator has been improved by adjusting the pellet chain speed with an inverter[1] from dV/V $\geq 3 \times 10^{-4}$ to dV/V=1.2~2.4$\times 10^{-4}$. The stable operation of the single-ended accelerator at 3MV has become possible by replacing the inductive resistance to the non-inductive ones which have been newly developed by JAERI to measure the high voltage of terminal and the ensuring of the uniform voltage clamp between the acceleration tube retaining acrylic board and acceleration tube by the two point connection.

Reference
1. K.Mizuhashi, A.Chiba, M.Ishii, T.Kitano and S.Tajima JAERI-Review 2004-025 (2004) 321-32

JP0650281

10.4 Radiation Control & Radioactive Waste Management in TIARA

Safety Division & Utilities and Maintenance Division
Department of Administrative Services, JAERI

1. Radiation Control

1.1 Individual monitoring

(1) Individual monitoring for the radiation workers

Table 1 shows a distribution on effective dose of the radiation workers in FY 2004. The effective dose values of almost workers were less than 0.1 mSv (minimum detectable dose).

Maximum dose was 0.4 mSv/y due to the overhaul of the cyclotron.

(2) Individual monitoring for the visitors and others

Table 2 shows number of persons who temporally entered the radiation controlled areas. The effective dose of all persons was less than 0.1 mSv.

Table1. Distributions on the effective dose i n FY 2004.

Persons / Items Periods		Number of persons			
		1st quarter	2nd quarter	3rd quarter	4th quarter
Distribution range of effective dose HE: Effective dose [*1] (mSv)	HE < 0.1	496	554	549	627
	0.1 ≦ HE ≦ 1.0	4	3	0	4
	1.0 < HE ≦ 5.0	0	0	0	0
	5.0 < HE ≦ 50.0	0	0	0	0
	50.0 < HE	0	0	0	0
Number of persons under radiation control (A)		500	557	549	631
Exposure above 1mSv	Number of persons (B)	0	0	0	0
	(B)/(A) ×100(%)	0	0	0	0
Mass effective dose (Person·mSv)		0.6	0.7	0.0	0.6
Mean dose (mSv)		0.00	0.00	0.00	0.00
Maximum dose (mSv)		0.2	0.3	0.0	0.2

*1 Not detected by internal exposure measurement.

Table 2. Number of persons who temporary entered in the radiation controlled areas in FY 2004.

Persons \ Periods \ Number of persons	Number of persons				
	1st quarter	2nd quarter	3rd quarter	4th quarter	Total
	460	354	514	426	1754

1.2 Monitoring of radioactive gases

Table 3 shows the maximum radioactive concentrations and total activities for radioactive gases released from TIARA's stack, during each quarter of FY 2004.

Small amount of ^{41}Ar and ^{11}C were detected for some time during operation of the cyclotron, but the pulverized substance (^{65}Zn, etc) were not detected

Table 3. Monitoring results of released gaseous radioactivity in FY 2004.

Nuclide \ Items \ Periods	1st quarter	2nd quarter	3rd quarter	4th quarter	Total
^{41}Ar — Maximum concentration (Bq/cm^3)	$<1.4 \times 10^{-4}$	$<1.4 \times 10^{-4}$	$<1.4 \times 10^{-4}$	$<1.4 \times 10^{-4}$	$<1.4 \times 10^{-4}$
^{41}Ar — Activity (Bq)	3.4×10^8	1.3×10^7	6.3×10^8	1.1×10^9	2.1×10^9
^{11}C — Maximum concentration (Bq/cm^3)	$<1.4 \times 10^{-4}$	$<1.4 \times 10^{-4}$	$<1.4 \times 10^{-4}$	$<1.4 \times 10^{-4}$	$<1.4 \times 10^{-4}$
^{11}C — Activity (Bq)	8.1×10^6	2.0×10^7	8.5×10^7	2.3×10^8	3.4×10^8
^{65}Zn — Maximum concentration (Bq/cm^3)	$<6.3 \times 10^{-10}$	$<4.8 \times 10^{-10}$	$<4.0 \times 10^{-10}$	$<4.3 \times 10^{-10}$	$<6.3 \times 10^{-10}$
^{65}Zn — Activity (Bq)	0	0	0	0	0

1.3 Monitoring for external radiation and surface contamination

External radiation monitoring was routinely carried out in/around the radiation controlled areas and surface contamination monitoring was also carried out. Neither unusual value of dose equivalent rate nor surface contamination were detected.

Figure 1 displays a typical example of distribution of the dose equivalent rate at the radiation controlled area in the cyclotron building.
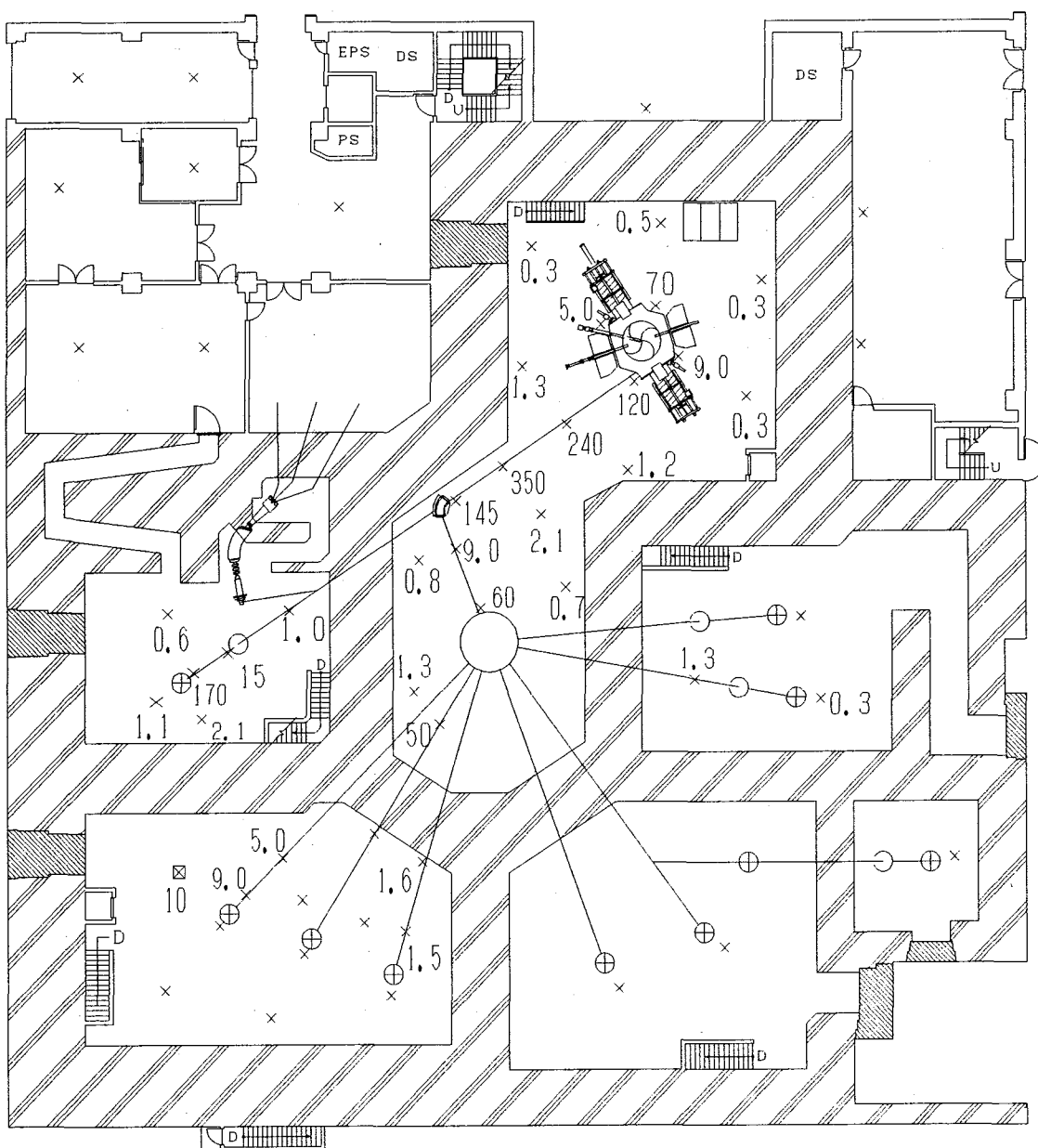
Fig.1 Dose rate distribution in the radiation controlled area in the cyclotron building.
　　　Date measured : March 29, 2005
　　　Measuring position : Indicated with ✕ 1m above floor
　　　Unit : μ Sv/h
　　　(the dose rates less than 0.2 μ Sv/h are not indicated)

2. Radioactive Waste Management

2.1 Solid wastes

Table 4 shows the amounts of solid wastes at various properties and kinds generated in each quarter of FY 2004. All wastes were combustible matter such as rubber gloves, compressible matter such as thin metals, and incompressible matter such as contaminated components. Compressible wastes were generated mainly by the cyclotron maintenance.

2.2 Liquid wastes

Liquid waste was almost waste water ("inorganic" in Table 5) generated with chemical experiments and operation of air conditioning units installed in each room of the first class radiation controlled area. Larger quantities of the wastewater in summer season (2nd quarter) are mainly due to condensed water, which is treated by evaporation, and condensed water is reused in the controlled area. Only small amounts of residue are generated by the evaporation because the waste quality is very pure.

Table 4. Radioactive solid wastes generated in FY 2004.

Amounts / Items	Amounts of generation in each periods (m^3)					Number of package /drum
	1st quarter	2nd quarter	3rd quarter	4th quarter	Total	
Category A*	0.62	0.48	0.74	0.59	2.43	
1)Combustible	0.42	0.42	0.62	0.40	1.86	11**
2)Incombustible	0.20	0.06	0.12	0.19	0.57	0
Compressible	0.20	0.06	0.12	0.08	0.46	3**
Filters	0	0	0	0.11	0.11	0
Incompressible	0	0	0	0	0	0
Ion exchange resin	0	0	0	0	0	0
(Cement solidify)	0	0	0	0	0	0
Category B*	0	0	0	0	0	0
1)Incombustible	0	0	0	0	0	0

* defined by dose at the outer surface of container : (A) < 2 mSv/h ≦ (B)
** 200-liter drum

Table 5. Radioactive liquid waste generated in FY 2004.

Amounts / Items	Amounts of generation in each periods (m^3)					Number of package /drum
	1st quarter	2nd quarter	3rd quarter	4th quarter	Total	
Category A*	8.24	14.16	8.04	5.66	36.10	
1)Inorganic	8.24	14.16	8.04	5.66	36.10	
2)Organic	0	0	0	0	0	0
Organic	0	0	0	0	0	0
Oil	0	0	0	0	0	0
3)Sludge	0	0	0	0	0	1
Category B*	0	0	0	0	0	0
1)Inorganic	0	0	0	0	0	0
2)Organic	0	0	0	0	0	0
Organic	0	0	0	0	0	0
Oil	0	0	0	0	0	0
3)Sludge	0	0	0	0	0	0
Evaporation residue	0	0	0	0	0	1

* defined by concentrations in Bq/cm^3(β,γ) : (A) < 3.7×10 ≦ (B) < 3.7×10^4

This is a blank page.

Appendix

This is a blank page.

Appendix 1. List of Publication

A. 1.1   Publications in Journal

14J01
M. Imaizumi, T. Sumita, S. Kawakita, K. Aoyama, O. Anzawa, T. Aburaya, T. Hisamatsu, S. Matsuda,
Results of flight demonstration of terrestrial solar cells in space,
Progress in Photovoltaics, Vol. 13, Iss. 2 (2005), pp. 93-102
CTI   SCS   41004, 42003

14J02
N. Chandrasekaran, T. Soga, Y. Inuzuka, H. Taguchi, M. Imaizumi, T. Ohshima, and T. Jimbo,
Low-Energy Proton Irradiation Effects on GaAs/Si Solar Cell,
Jpn.   J.   Appl.   Phys.   43   10A(2004) L1302-L1304.
CTI   SCS   41004, 42003   42005

14J03
A.   Khan,   S.   Marupaduga,   S.   S. Anandakrishnan, M. Alam, N. J. Ekins-Daukes, H. S. Lee, T. Sasaki, M. Yamaguchi, T. Takamoto, T. Agui, K. kamimura, M. Kaneiwa, and M. Imaizumi,
Radiation response analysis of wide-gap p-AlInGaP for superhigh-efficiency space photovoltaics,
Appl. Phys. Lett., 85 No.22 (2004) 5218-5220.
CTI   SCS   41004, 42003

14J04
N. J. Ekins-Daukes, H. S. Lee, T. Sasaki, M. Yamaguchi, A. Khan, T. Takamoto, T. Agui, K. kamimura, M. Kaneiwa, M. Imaizumi, T. Ohshima, and T. Kamiya,
Carrier removal in lattice-mismatched InGaP

solar cells under 1-MeV-electrron irradiation,
Appl. Phys. Lett., 85 No.13 (2004) 2511-2513.
CTI   SCS   41004, 42003   42005

14J05
J. S. Laird, T. Hirao, S. Onoda and T. Kamiya,
The role of high-injection effects on the transient ion beam induced current response of high-speed photodetectors,
Nucl. Instrum. Methods. B 219-220 (2004) 1015
T   SCS   42002

14J06
S. Onoda, T. Hirao, J. S. Laird, T. Wakasa, T. Yamakawa, T. Okamoto, Y. Koizumi, and T. Kamiya,
Development of Monte Carlo modeling for proton induced charge in Si pin photodiode,
IEEE Trans.
Nucl. Sci., NS-51, No.5, pp.2770 – 2775 (2004)
CT   SCS   41001

14J07
T. Ohshima, T. Satoh, M. Oikawa, T. Yamakawa, S. Onoda, T. Wakasa, J. S. Laird, T. Hirao, T. Kamiya, H. Itoh, A. Kinoshita, R. Tanaka, I. Nakano, M. Iwami, Y. Fukushima
Characterization of charge generated in silicon carbide n+p diodes using transient ion beam-induced current
Nucl. Instrum. Methods Phys. Res. A 541 (2005) pp.236-240.
T I   SCS   ACT   42004

14J08
A. Kinoshita, M. Iwami, K. Kobayashi, I.

Nakano, R. Tanaka, T. Kamiya, A. Ohi, T. Ohshima, Y. Fukushima
Radiation effect on pn-SiC diode as a detector
Nucl. Instrum. Methods Phys. Res. A 541 (2005) pp.213-220.
I SCS 42004

14J09
T. Ohshima, K. K. Lee, Y. Ishida, K. Kojima, Y. Tanaka, T. Takahashi, M. Yoshikawa, H. Okumura, K. Arai, and T. Kamiya
Relationship between the current direction in the inversion layer and the electrical characteristics of metal-oxide-semiconductor field effect transistors on 3C-SiC
Mater. Sci. Forum 457-460 (2004) P.P 1405-1408
I SCS 42004 42043

14J10
M. Laube, G. Pensl, K. K. Lee, and T. Ohshima
Comparison of the electrical channel properties between dry- and wet-oxidized 6H-SiC MOSFETs investigated by Hall effect
Mater. Sci. Forum 457-460 (2004) P.P 1381-1384.
I SCS 42004

14J11
A.Wakahara, T.Fujiwara, H.Okada, A.Yoshida, T.Ohshima, and H.Itho,
Energy-back-transfer process in rare-earth doped AlGaN,
MRS proceedings, in press
T SCS 42008

14J12
T.Fujiwara, A.Wakahara, Y.Nakanishi, H.Okada, A.Yoshida, T.Ohshima, and T.Kamiya,
Photoluminescence properties of Eu-implanted

$Al_xGa_{1-x}N(0 \leqq x \leqq 1)$,
Phys. Status Solidi (c), 2 (7), (2005) pp.2805-2808
T SCS 42008

14J13
A.Wakahara, Y.Nakanishi, T.Fujiwara, H.Okada, A.Yoshida, T.Ohshima, and T.Kamiya,
Enhancement of Tb-related cathodo luminescence in $Al_xGa_{1-x}N$ ($0 \leqq x \leqq 1$),
Phys. Status Solidi (a) 202 (5), (2005) pp.863-867
T SCS 42008

14J14
A. Wakahara, Y. Nakanishi, T. Fujiwara, A. Yoshida, T. Ohshima, and T. Kamiya,
Strong blue emission from Er^{3+} doped in $Al_xGa_{1-x}N$,
Phys. Status Solidi (a) 201 (2004) pp.2768-2772
T SCS 42008

14J15
A. Yoshida, A. Wakahara, Y. Nakanishi, H. Okada, T. Ohshima, H. Itoh, and Yong-Tae Kim,
Luminescence properties of rare-earth implanted into AlGaN,
Key Engineering Materials, 270, (2004) pp.878-883
T SCS 42008

14J16
Y. Yokota, N. Shikazono, A. Tanaka, Y. Hase, T. Funayama, S. Wada, M. Inoue,
Comparative Radiation Tolerance Based on the Induction of DNA Double-Strand Breaks in Tobacco BY-2 Cells and CHO-K1 Cells Irradiated with Gamma Rays,
Radiat. Res. 163, 520-525 (2005)

C BIT 41008

14J17

M.Okamura,

Development of New Variety Series in 3 Major Flowers by Ion Beam Breeding,

Bio-Industry, vol.3, 55-60. (2005)

C BIT 41013

14J18

M.Okamura, N.Yasuno, M.Takano, A.Tanaka, N.Shikazono and Y.Hase,

Wide variety of flower-color and –shape mutants regenerated from leaf cultures irradiated with ion beams,

Nucl. Instrum. Methods B 206 (2003)574-578

C BIT 41013

14J19

M.Okamura,

Commercialization of New Variety Series in 3 Major Flowers bred by Ion Beam Breeding,

Radiation & Industries 99,(2003) 46-53

C BIT 41013

14J20

S. Nagayoshi,

Irradiation Breeding in KAGOSHIMA; Breeding of 'few axillary bud lines' using ion beam in Chrysanthemum.

Radiation & Industries 98,(2003) 10-16.

C BIT 41014

14J21

N. Hata, K. Murakami, Y. Yoshida and M. Masuda,

Effect of Temperature on Expression of Gynomonoecy in Selfed-seed Population of Spinacia oleracea L.,

J. Japan. Soc. Hort. Sci. 74 (2005) 228-233.

C BIT 41017 .

14J22

Y. Hase, S. Fujioka, S. Yoshida, G. Sun, M. Umeda and A. Tanaka,

Ectopic endoreduplication caused by sterol alteration results in serrated petals in Arabidopsis.

J. Exp. Bot. 56, 1263-1268.

C BIT 41027

14J23

M. Takahashi, S. Kohama, K. Kondo, M. Hakata, Y. Hase, N. Shikazono, A. Tanaka and H. Morikawa,

Effects of ion beam irradiation of the regeneration and morphology of *Ficus thunberii* Maxim.

Plant Biotechnology 22, 63-67.

C BIT 41027

14J24

T. Funayama, S. Wada, Y. Kobayashi, H. Watanabe,

Irradiation of mammalian cultured cells with collimated heavy ion microbeam,

Radiat. Res. 163, (2005) 241–246.

C BIT 41034

14J25

E. Ling, K. Shirai, R. Kanekatsu, K. Kiguchi, Y. Kobayashi, T. Funayama and H. Watanabe,

Contribution of invaded circulating hemocytes to the regeneration of heavy ion beams ($^{12}C^{5+}$) irradiated hematopoietic organs in the silkworm, *Bombyx mori*, through the way of phagocytosis of injured cells inside

Development & Comparative Immunology (submitted)

C BIT 41035

14J26

C. Shao, M. Aoki, Y. Furusawa,

Bystander effect in lymphoma cells vicinal to

irradiated neoplastic epithelial cells: Notric oxide is involved. ,
J. Radiat. Res., 45, (2004) 97-103,
C BIT 41036

14J27
S. Wada, T. V. Khoa, Y. Kobayashi, T. Funayama, K.Yamamoto, M. Natsuhori, and N. Ito,
Detection of Radiation-Induced Apoptosis Using the Comet Assay.
J. Vet. Med. Sci., 2003, 65(11): 1161-1166
C BIT 41037

14J28
C. Zheng-Guo, T Kondo, H. Matsumoto
Enhancement of apoptosis by nitric oxide released from α-phenyl-tert-butyl nitrone under hyperthermic conditions.
J. Cell. Physiol. In press, 2005.
C BIT 41039

14J29
N. Narita, S. Fujieda, H. Matsumoto, M. Tokuriki, N Takahashi, H. Tsuzuki, T. Ohtsubo
Inhibition of Histone Deacetylase 3 Stimulates Apoptosis Induced by Heat Shock under the Acidic Conditions in Human Maxillary Cancer *In Vitro and In Vivo*.
Oncogene, in press, 2005.
C BIT 41039

14J30
A. Takahashi, H. Matsumoto, K. Nagayama, M. Kitano, S. Hirose, H. Tanaka, E. Mori, N. Yamakawa, J. Yasumoto, K. Yuki, K. Ohnishi, T. Ohnishi,
Evidence for the involvement of DSBs in heat-induced cell killing.
Cancer Res., 64: 8839-8845, 2004
C BIT 41039

14J31
A. Takahashi, H. Matsumoto, K. Yuki, J. Yasumoto, A. Kajiwara, M. Aoki, Y. Furusawa, K. Ohnishi, T. Ohnishi,
High-LET radiation enhanced apoptosis but not necrosis regardless of p53 status.
Int. J. Radiat. Oncol. Biol. Phy., 60: 591-597, 2004.
C BIT 41039

14J32
M. Watanabe, T. Kikawada, A. Fujita, T. Adati, E. Forczek, T. Okuda,
Physiological traits of invertebrates entering cryptobiosis in a post-embryonic stage.
Eur. J. Entomol. 101: 439-444 (2004).
C BIT 41040

14J33
M. Watanabe, T. Kikawada, A. Fujita, T. Okuda T,
Induction of cryptobiosis in fat body from an insect.
J. Insect Physiol. in press.
C BIT 41040

14J34
S. Matsuhashi, S. Fujimaki, N. Kawachi, K. Sakamoto, N. S. Ishioka and T. Kume,
Quantitative modeling of photoassimilate flow in an intact plant with the Positron Emitting Tracer Imaging System (PETIS),
Soil Sci. Plant Nutr., 51. 417-423 (2005)
C RCO 01043

14J35
R. E. Moghaieb. N. Tanaka, H. Saneoka, Y. Murooka, H. Ono, H. Morikawa, N. T. Nguyen, R. Suwa, A. Nakamura, and K. Fujita,
Transgenic tobacco plant introduced by ectoine gene, in relation to nitrogen metabolism

2005, Plant Cell, Environment, in press
O BIT 41046

14J36
N. T. Nguyen, N. D. Hiep, K. Fujita,
Effects of aluminium and iron on plant growth and concentrations of antioxidants and pigments in leaves of Eucalyptus camaldulensis
Plant and Soil, 2005
O BIT 41046

14J37
R. E. Moghaieb, A. M. I. Saana, H. Saneoka, K. Fujita,
Molecular characterization of heat tolerance in two isolates(HTS-1 and HTS-2) derived from the entomopathogenic nematode strain ISK-2 (Heterorhabditis species)
International Journal of Nematology, 14, No.1 2004, 66-72)
O BIT 41046

14J38
T. N. Nguyen, R. E. Moghaieb, H. Saneoka and K. Fujita,
RAPD markers associated with salt tolerance in Acacia auriculiformis and Acacia mangium,
Plant Science, Volume 167, Issue 4, October 2004, Pages 797-805
O BIT 41046

14J39
H. Saneoka, R. E. Moghaieb, G.S. Premachandra, and K. Fujita,
Nitrogen nutrition and water stress effects on cell membrane stability and leaf water relations in Agrostis palustris Huds,
Environmental and Experimental Botany, 2004
O BIT 41046

14J40

R. E. Moghaieb, H. Saneoka, K. Fujita,
Shoot regeneraion from GUS-transformed tomato (Lycopersicon esculentum) hairy root
Cellular & Molecular Biology Letters Vol. 9, No. 3, 439 − 449、 2004
O BIT 41046

14J41
R. E. Moghaieb, H. Saneoka, K. Fujita.
Effect of salinity on osmotic adjustment, glycinebetaine accumulation and the betaine aldehyde dehydrogenase gene expression in two halophytic plants, Salicornia europaea and Suaeda maritima,
Plant Science 166, 1345-1349, 2004
O BIT 41046

14J42
T. N. Nguyen, K. Fujita,
Eucalyptus camaldulensis Dehnh. is sensitive to Al and low pH
SSPN Special Vol. 2004
O BIT 41046

14J43
T. Tsukamoto, H. Uchida, H. Nakanishi, S. Nishiyama, H. Tsukada, S. Matsuhashi, N. K. Nishizawa,
Mori S, $H_2{}^{15}O$ translocation in rice was enhanced by 10 μM 5-aminolevulinic acid as monitored by positron emitting tracer imaging system (PETIS).
Soil Sci. Plant Nutr. 50: 1085-1088 (2004).
C BIT 41047

14J44
M. N. Saha, A. Tanaka, A. Jinno-Oue, N. Shimizu, K. Tamura, M. Shinagawa, J. Chiba, and H. Hoshino
Formation of Vesicular Stomatitis Virus Pseudotypes Bearing Surface Proteins of Hepatitis B Virus.

J. Virol. (in press)
C ACT 41067

14J45
Y. Shimizu a , M. Okoba, N. Yamazaki, Y. Goto, T. Miura, M. Hayami b , H. Hoshino, and T. Haga
Construction and in vitro characterization of a chimeric simian and human immunodeficiency virus with the RANTES gene.
Microbes Infect. (in press)
C ACT 41067

14J46
A. Jinno-Oue, N. Shimizu, Y. Soda, A. Tanaka, T. Ohtsuki, D. Kurosaki, Y. Suzuki, H. Hoshino
The synthetic peptide derived from the NH2-terminal extracellular region of an orphan G protein-coupled receptor,
GPR1, preferentially inhibits infection of X4 human immunodeficiency virus type 1.
J. Biol. Chem. (in press)
C ACT 41067

14J47
K. Tamura, A. Oue, A. Tanaka, N. Shimizu, H. Takagi, N. Kato, A. Morikawa, H. Hoshino.
Efficient formation of vesicular stomatitis virus pseudotypes bearing the native forms of hepatitis C virus envelope proteins detected after sonication.
Microbes Infect. 2005, 7:29-40
C ACT 41067

14J48
A. Shimizu, N. Shimizu, A. Tanaka, A. Jinno-Oue, BB Roy, M. Shinagawa, O. Ishikawa, H. Hoshino.
Human T-cell leukaemia virus type I is highly sensitive to UV-C light.
J. Gen. Virol. 2004, 85:2397-406.

C ACT 41067

14J49
Y. Suzuki, T. Yamaki, M. Asano, M. Yoshida,
First successful results of etched track formation in poly(p-phenylene terephthalamide) with ion beam from MeV to GeV,
Polymer, in preparation
C RCO 41055

14J50
M. Taguchi and T. Kojima
Yield of OH radicals in water under high-density energy deposition by heavy ion irradiation.
Radiat. Res. 163, 455 (2005).
C RCO 41057

14J51
S. Tsukuda, S. Seki, M. Sugimoto, S. Tagawa
Formation of nanowires based on π-conjugated polymers by high-energy ion beam irradiation
Jpn. J. Appl. Phys. 44 (2005) in press.
C RCO 41059

14J52
Y. Matsui, S. Seki, S. Tagawa
Fluoropolymer Outgassing in Focused Ion Beam Micromachining
J. Photopolym. Sci. Technol., 18 (2005) 501-502.
C RCO 41059

14J53
S. Seki, S. Tsukuda, S. Tagawa, M. Sugimoto
Correlation between Edge Roughness of Nanostructures and Backbone Configuration of Polymer Materials
J. Photopolym. Sci. Technol., 18 (2005) 449-450.
C RCO 41059

14J54

S. Seki, S. Kawachi, S. Tagawa, A. Egami, K. Kurihara, M. Nakamura, H. Itoh

Etching Efficiency of Polymethacrylates for Monochromatic

Low Energy Ion Beams

J. Photopolym. Sci. Technol., 18 (2005) 255-256.

C RCO 41059

14J55

A. Saeki, S. Seki, Y. Koizumi, T. Sunagawa, K. Ushida, and S. Tagawa

Increase of Mobility of Photogenerated Positive Charge Carriers in Polythiophene

J. Phys. Chem. B, 109 (2005) 10015-10019.

C RCO 41059

14J56

A. Acharya, Y. Koizumi, S. Seki, A. Saeki, S. Tagawa, Y. Ie, and Y. Aso

Effect of Substituents on Charge Carrier Dynamics in Thiophene Oligomers

J. Photochem. Phtobiol. A, 173 (2005) 161-168.

C RCO 41059

14J57

A. Acharya, S. Seki, A. Saeki, Y. Koizumi, S. Tagawa

Study of transport properties in fullerene-doped polysilane films using flash photolysis time-resolved microwave technique

Chem Phys. Lett. 404 (2005) 356-360.

C RCO 41059

14J58

M. Todo, K. Okamoto, S. Seki, S. Tagawa

Formation of benzene trimer radical cation in g-irradiated low temperature 2-methylpentane matrices

Chem. Phys. Lett. 399 (2004) 378-383.

C RCO 41059

14J59

S. Seki, S. Tsukuda, K. Maeda, Y. Matsui, A. Saeki, and S. Tagawa

Inhomogeneous distribution of crosslinks in ion tracks in polystyrene and polysilanes

Phys. Rev. B, 70 (2004) 144203.

C RCO 41059

14J60

Y. Koizumi, S. Seki, A. Acharya, A. Saeki, and S. Tagawa

Delocalization of Positive and Negative Charge Carriers on Oligo- and Poly-fluorenes Studied by Low Temperature Matrix Isolation Technique

Chem. Lett., 33 (2004) 1290-1291.

C RCO 41059

14J61

Y. Matsui, S. Seki, S. Tagawa, S. Kishimura, M. Sasago

157-nm-induced resist outgassing studied by film thickness loss and in-situ quadrupole mass spectrometry

J. Photopolym. Sci. Technol., 17 (2004) 671-673.

C RCO 41059

14J62

S. Tsukuda, S. Seki, S. Tagawa, M. Sugimoto, A. Idesaki, S. Tanaka, A. Ohshima

Fabrication of Nano-Wires Using High-Energy Ion Beams

J. Phys. Chem. B, 108 (2004) 3407-3409

C RCO 41059

14J63

S. Seki, Y. Koizumi, T. Kawaguchi, H. Habara, S. Tagawa

Dynamics of Positive Charge Carriers on Si

Chains of Polysilanes
J. Am. Chem. Soc. 126 (2004) 3521-3528
C   RCO   41059

14J64
S. Tsukuda, S. Seki, A. Saeki, T. Kozawa, S.
Tagawa, M. Sugimoto, A. Idesaki, S. Tanaka
Precise Control of Nanowire Formation Based
on Polysilane for Photoelectronic Device
Application
Jpn. J. Appl. Phys. 43 (2004) 3810-3814.
C   RCO   41059

14J65
Y. Terashima, S. Seki, M. Tashiro, Y. Honda,
S. Tanaka
Formation   of   Defect   Structures   in
Au-Polysilane Interfaces Probed by Low
Energy Positron Beams
Solid State Commun.,132 (2004) 641-645.
C   RCO   41059

14J66
K. Hirata, Y. Saitoh, A. Chiba, K. Narumi, Y.
Kobayashi, and Y. Ohara,
Highly sensitive time-of-flight secondary-ion
mass spectroscopy for contaminant analysis of
semiconductor surface using cluster impact
ionization,
Appl. Phys. Lett., 86, 044105 (2005)
T I   RCO   42016

14J67
T. Taguchi, N. Igawa, E. Wakai, S. Miwa, S.
Jitsukawa, L. L. Snead, A. Hasegawa,
Synergistic effect of helium and hydrogen as
transmutation   products   and   irradiation
temperature on microstructural change of
SiC/SiC composite,
J. Nucl. Mater., 335 (2004) 508-514.
T I S   IOM   42009

14J68
T. Taguchi, N. Igawa, S. Jitsukawa and K.
Shimura,
Effect of He ions implantation on thermal
diffusivities of SiC and SiC/SiC composites,
Nucl. Instrum. Methods. B, in press.
C   IOM   42009

14J69
S. Miwa, A. Hasegawa, T. Taguchi, N. Igawa
and K. Abe,
Cavity Formation in a SiC/SiC Composite
under Simultaneous Irradiation of Hydrogen,
Helium and Silicon ions,
Mater. Trans., 46 (2005) 536-542.
T I S   IOM   42009

14J70
M. Ando, E. Wakai, T. Sawai, H. Tanigawa, K.
Furuya, S. Jitsukawa, H. Takeuchi, K. Oka, S.
Ohnuki and A. Kohyama,
Synergistic effect of displacement damage and
helium atoms on radiation hardening in F82H
at TIARA facility,
J. Nucl. Mater. 329-333(2004)1137-1141.
T I S   IOM   42010

14J71
E. Wakai, M. Sato, T. Sawai, K. Shiba and S.
Jitsukawa,
Mechanical Properties and Microstructure of
F82H Steel Doped with Boron or Boron and
Nitrogen as a Function of Heat Treatment
Mater. Trans., 45 (2004) P.P407-410.
T I S   IOM   42010

14J72
T. Tanaka, K. Oka T. Suda, S. WatanabeS.
Ohnuki, S. Yamashita E. Wakai,
Synergistic effect of helium and hydrogen for
defect evolution under multi-ion irradiation of
Fe-Cr ferritic alloys,

J. Nucl. Mater. 329-333(2004)294-298.

T I S   IOM   42010

14J73

S. Yamashita, N. Akasaka S. Ohnuki,

Nano-oxide particle stability of grain morphology modified oxide dispersion strengthened (ODS) steels under neutron irradiation circumstance,

J. Nucl. Mater. 329-333(2004)377-381.

T I S   IOM   42010

14J74

I.Ioka, M.Futakawa, A.Naito, Y.Nanjyo, K.Kiuchi and T.Naoe,

Mechanical Characterization of Austenitic Stainless Steel ion-irradiated under External Stress,

J. Nucl. Mater. 329-333(2004)1142-1146.

T I S   MAN   42012

14J75

D.Yamaki, T.Nakazawa, T.Tanifuji, T.Aruga, S.Jitsukawa, K.Hojou,

Observation of the microstructural changes in lithium titanate by multi-ion irradiation,

J. Nucl. Mater., 329-333, 2004,

T I S   IOM   42040

14J76

H. Abe, N. Sekimura and T. Tadokoro

Stability and Mobility of Interstitial-Type Defect Clusters Generated from Displacement Cascades in Copper and Gold by In-Situ Transmission Electron Microscopy

Mater. Trans., 46 (2005) 433-439

I   IOM   42018

14J77

S. Kitazawa, H. Abe and S. Yamamoto

Formation of nanostructured solid-state carbon particles by laser ablation of graphite in

isopropyl alcohol

J. Phys. Chem. Solids. 66 (2005) 555-559

I   IOM   42018

14J78

J. Vacik, H. Naramoto, K. Narumi, S. Yamamoto, H. Abe

Study of the nickel-fullerene nano-structured thin films

Nucl. Instrum. Methods B219-220 (2004) 862-866

I   IOM   42018

14J79

J. Vacik, H. Naramoto, K. Narumi, S. Yamamoto, H. Abe

RBS and SEM analysis of the nickel-fullerene hybrid systems

Nucl. Instrum. Methods B206 (2004) 395-398

I   IOM   42018

14J80

H. Abe, N. Sekimura, Y. Yang

Stability and mobility of defect clusters in copper under displacement cascade conditions

J. Nucl. Mater., 323 (2003) 220–228

I   IOM   42018

14J81

Hiroaki Abe

Atomistic observations and analyses of lattice defects in transmission electron microscopes (Japanese)

Journal the Visualization Society of Japan 23(2003)145

I   IOM   42018

14J82

V. Lavrentiev, H. Abe, S. Yamamoto, H. Naramoto, K. Narumi

Isolation of Co nanoparticles by C_{60} molecules in co-deposited film

Mater. Lett. 57 (2003)4093-4097

I IOM 42018

14J83

V. Lavrentiev, H. Abe, S. Yamamoto, H. Naramoto, K. Narumi

Formation of promising Co-C nanocompositions

Surf. Interface Anal., 35 (2003) 36-39

I IOM 42018

14J84

M. Matsubara, T. Yamaki, H. Itoh, H. Abe, K. Asai

Preparation of TiO2 nanoparticles by pulsed laser ablation: ambient pressure dependence of crystallization

Jpn. J. Appl. Phys. 42 (2003) L479-L481

I IOM 42018

14J85

Y. Kasukabe, Z.L. Dizard, Y. Fujino, H. Tani, M. Osaka, Y. Yamada, H. Abe

In-situ observation of formation process of titanium compound thin films due to ion implantation in a transmission electron microscope

Nucl. Instrum. Methods. B 206 (2003) 390-394

I IOM 42018

14J86

Y. Kasukabe, J. J. Wang T. Yamamura, S. Yamamoto and Y. Fujino,

Nitriding Transformation of Titanium Thin Films by Nitrogen-Implantation,

Thin Solid Films, 464-465(2004) 180-184.

I IOM 42019

14J87

J. J. Wang, Y. Kasukabe, T. Yamamura, S.

Yamamoto and Y. Fujino,

In-situ Transmission Electron Microscope Observation of Nitriding Processes of Titanium Thin Films by Nitrogen-Implantation,

Thin Solid Films, 464-465(2004) 175-179.

I IOM 42019

14J88

A. Takeyama, Y. Yamamoto, H. Yoshikawa, H. Ito,

Growth of ZnO Nanorods on Cu Implanted Substrates,

Jpn. J. Appl. Phys. 44 1B, (2005) 750-753.

I S IOM 42023

14J89

A. Takeyama, Y. Yamamoto, H. Ito, H. Yoshikawa,

Formation of Cu precipitates by ion implantation and thermal annealing for the growth of oxide nanorods,

Nucl. Instrum. Methods B 232 (2005) 333-337

I S IOM 42023

14J90

A. Takeyama, Y. Yamamoto, H. Ito, H. Yoshikawa,

Catalytic Effect of Cu Precipitates for the Growth of ZnO Rods,

Trans. Mater. Res. Soc. Jpn. in press.

I S IOM 42023

14J91

Z. Q. Chen, M. Maekawa, S. Yamamoto, A. Kawasuso, X. L. Yuan, T. Sekiguchi, R. Suzuki, T. Ohdaira,

Evolution of voids in Al+-implanted ZnO probed by a slow positron beam,

Phys. Rev. B69 (2004)35210-35219.

I IOM 42035

14J92

Z. Q. Chen, Y. Xu, A. Kawasuso, X. L. Yuan, T. Sekiguchi, R. Suzuki and T. Ohdaira,
Production and recovery of defects in P+-implanted ZnO studied by positron annihilation, Raman scattering, and cathodoluminescence measurements,
J. Appl. Phys. 97,(2005)13528-13533.
I IOM 42035

14J93

Z. Q. Chen, A. Kawasuso, Y. Xu, H. Naramoto, X. L. Yuan, T. Sekiguchi, R. Suzuki and T. Ohdaira,
Hydrogen implantation induced microvoid formation in ZnO probed by a slow positron beam,
Phys. Rev. B71(2005)115213-115220.
I IOM 42035

14J94

N. T. Son, A. Henry, J. Isoya, E. Janzén,
Eelectron paramagnetic resonance of shallow phosphorous centers in 4H- and 6H-SiC
Mate. Sci. Forum 483-485 (2005) 515
T IOM 42033

14J95

T. Umeda, J. Isoya, N. Morishita, T. Ohshima, T. Kamiya, A. Gali, P. Deák, N. T. Son, E. Janzén,
Physical Review B 70, 235212 (2004).
EPR and theoretical studies of positively-charged carbon vacancy in 4H-SiC,
O IOM 42033

14J96

N. T. Son, E. Janzén, J. Isoya, S. Yamasaki,
Hyperfine interaction of the nitrogen donor in 4H-SiC,
Physical Review B 70, 193207 (2004).
O IOM 42033

14J97

T. Umeda, J. Isoya, N. Morishita, T. Ohshima, T. Kamiya,
EPR identification of two types of carbon vacancies in 4H-SiC,
Physical Review B 69, 121201(R) (2004).
O IOM 42033

14J98

K.Awazu, H. Yasui, N. Ikenaga, T. Kawabata, Y. Hasegawa and N. Sakudo,
The properties of Hybrid Nanodiamond (HND) films,
New Diamond, 2005, Vol.21, No1. pp.28-29.
T IOM 42026

14J99

V. Lavrentiev, H. Naramoto, H. Abe, S. Yamamoto, K. Narumi and S. Sakai,
Chemically-driven Microstructure Evolution in Cobalt-fullerene Mixed System
Fullerene, Nanotubes and Carbon Nanostructures 12 (2004) 519-528.
I S IOM 12029

14J100

X. D. Zhu, X. H. Wen, R. J. Zhan, H. Naramoto and F. Arefi-Khonsart,
Control of Characteristic Lengths for Self-Organized Nanostructures of Amorphous Carbon
J. Phys. : Con. Mat. 16 (2004) 1175-1181.
O IOM off line

14J101

J. Vacik, H. Naramoto, K. Narumi, S. Yamamoto and H. Abe,
Study of the Nickel-Fullerene Nano-structured Thin Films
Nucl. Instrum. Methods B 219-220 (2004) 862-866.
I S IOM 32024

14J102

A. E. Aleksensky, M. V. Baidakova, M. A. Yagovkina, V. I. Siklitsky, A. Ya. Vul', H. Naramoto and V. I. Lavrentiev,

Nanodiamonds Intercalated with Metals. Structure and Diamond Graphite Phase Transitions

Diamond and Related Materials 13 (2004) 2076-2080.

O IOM off line

14J103

X. D. Zhu, K. Narumi, Y. Xu, H. Naramoto and F. Arefi-Khonsari,

Self-organized Textured Surfaces of Amorphous Carbon

J. Appl. Phys. 95 (2004) 4105-4110.

O IOM off line

14J104

J. Vacik, H. Naramoto, S. Kitazawa, S. Yamamoto and L. Juha,

Laser-induced phase separation in the nickel–fullerene nano-composite

J. Phys. Chem. Solids. 66 (2005) 581-584.

I S IOM 42027

14J105

S. Sakai1, H. Naramoto, V. Lavrentiev, K. Narumi, M. Maekawa, A. Kawasuso, T. Yaita and Y. Baba,

Polymeric Co-C$_{60}$ Compound Phase Evolved in Atomistically Mixed Thin Films

Mater. Trans., 46 (2005) 765-768.

I S IOM 42027

14J106

Y. Aratono, A. Wada, K. Akiyama, S. Kitazawa, K. Hojou and H. Naramoto,

Formation of Fullerene (C$_{60}$) by Laser Ablation in Superfluid Helium at 1.5 K

Chem. Phys. Lett., 408 (2005) 247-251

O IOM off line

14J107

S. Watanabe, N. S. Ishioka, T. Sekine, H. Kudo, H. Shimomura, H. Muramatsu, T. Kume

Conversion of endohedral ^{133}Xe-fullerene to endohedral ^{133}Xe-fullerenol to be used for nuclear medicine.

J. Radioanal. Nucl. Chem. in press

O NRI off line 42043

14J108

C.-J. Ma, S. Tohno, M. Kasahara

2004. A case study of the single and size-resolved particles in roadway tunnel in Seoul,

Korea. Atmos. Environ. 38, 6673-6677.

S RCO 42041

14J109

T. Ohnuki, F. Sakamoto, N. Kozai, T. Ozaki, T. Yoshida, I. Narumi, E. Wakai, T. Sakai, A. J. Francis,

Mechanisms of arsenic immobilization in biomat from mine discharge water,

Chem. Geol., 212(2004)279-290.

S IOM 42042

14J110

H. Fujii, K. Hara, K. Komine, T. Ozaki, T. Ohnuki, and Y. Yakamoto,

Accumulation of Cu and its oxidation state in Tremolecia atrata (rusty-rock lichen) mycobiont,

J. Nuclear and Radiochemical Sciences, in press(2005)

T C IOM 42042

14J111

T. Sakai, M. Oikawa, T. Sato, T. Nagamine, H. D. Moon, K. Nakazato and K. Suzuki,

New in-air micro-PIXE system for biological

applications
Nucl. Instr. Meth. B231 (2005) 112.
S ACT 42044

14J112
T. Sakai, M. Oikawa, T. Satoh,
Elemental analysis technique using proton
microprobe
Ionizing Radiation Vol. 31, No. 2 (2005) 129.
(in Japanese)
S ACT 42044

14J113
T. Sakai, M. Oikawa and T. Sato,
External scanning proton microprobe
- a new method for in-air elemental analysis –
J. Nucl. Radiochem. Sci., Vol. 6, No.1 (2005)
71-73,
S ACT 42044

14J114
H.Yamamoto, M.Nomachi , K.Yasuda ,
Y.Iwami, S.Ebisu, T.Sakai, M.Fukuda,
Fluorine Mapping in Sound and Carious
Fissures of Human Teeth Using PIGE,
Nucl. Instrum. Methods B 231 (2005) P.300.
S ACT 42047

14J115
T. Sakai, M. Oikawa, T. Sato, T. Nagamine,
H.D. Moon, K. Nakazato, K. Suzuki.
New in-air micro-PIXE system for biological
applications.
Nucl. Instrum. Methods B 231 (2005)
P.P112-116
S ACT 42048

14J116
S. Harada, K. Ishii, A. Tanaka, T. Satoh, S.
Matsuyama, H. Yamazaki, T. Kamiya, T.
Sakai, K. Arakawa, M. Saitoh, S. Oikawa and
K. Sera

Method for Determing the localization of
Trace Elements Observed by the Micro PIXE
camera,
Int. J. PIXE, 14 (3&4), 2004, 83-88
S BIT 42051

14J117
S. Harada,K. Ishii, and Y. Ohara.
Determination of radiation Induced
apoptosis by the kinetics of the
trace-elements, and predicting the
antitumor effect and prognosis of radiation
therapy
INNERVISION (2004) 17/7 27-28
S BIT 42051

14J118
S. Harada, S. Ehara, K. Ishii, A. Tanaka, T.
Satoh, S. Matsuyama, H. Yamazaki, Y.
Komori, T. Kamiya, T. Arakawa, M. Saitoh, M.
Oikawa, and K. Sera.
The kinetics of Fe and Ca for the development
of apoptosis.
Nucl. Instrum. Methods B 210 (2003) 388-394
S BIT 42051

14J119
S.Harada, Y.Tamakawa, K.Ishii, A.Tanaka,
T.Satoh, S.Matsuyama, H.Yamazaki,
Y.Komori, T.Kamiya, T.Sakai, K.Arakawa,
M.Saitoh, S.Oikawa, K.Sera ,
The kinetics of Fe and Ca for the development
of radiation-induced apoptosis by micro-PIXE
imaging,
Nucl. Instrum. Methods B 210 (2003)
383-387.
S BIT 42051

14J120
K.Ishii, H.Yamazaki, S.Matsuyama and
Y.Kikuchi,
Establishment of Central Research Laboratory

for Accurate Quantitative PIXE Analysis -An Approach of Tohoku University-,
Int. J. PIXE, 13 (1&2), 2003, 17-22
S   ACT   42053

14J121
S.Matsuyama,   K.Ishii,   H.Yamazaki, Y.Barbotteau, Ts. Amartaibvan, D.Izukawa, K.Hotta,   K.Mizuma,   S.Abe,   Y.Ohishi, M.Rodrigeez,   A.Suzuki,   R.   Sakamoto, M.Fujisawa, T.Kamiya, M.Oikawa,
Microbeam Analysis System at Tohoku University,
Int. J. PIXE, 14, (2004) 1-8.
S   ACT   42053

14J122
Y.   Barbotteau,   K.Ishii,   K.   Mizuma, H.Yamazaki, S.Matsuyama,T.Sakai, T. Satoh, and T. Kamiya,
Behavior of Pet Foil Used as Beam Extraction Window During Irradiation at Atmospheric Pressure,
Int. J. PIXE, 14, (2004) 19-25
S   ACT   42053

14J123
K.Mizuma,   K.Ishii,   Y.Barbotteau,   S.Abe, H.Yamazaki,   S.Matsuyama,   E.Sakurai, K.Yanai,   T.Kamiya,   T.Sakai,   T.   Satoh, M.Oikawa and K. Arakawa,
The Elemental Analysis of IgE-Sensitized RBL-2H3 Cells Using In-Air Micro-PIXE,
Int. J. PIXE, 14, (2004) 27-34.
S   ACT   42053

14J124
H.Yamazaki,   K.Ishii,   S.Matsuyama,   Ts. Amartaivan,   A.Suzuki,   T.Yamaguchi,   G. Momose, K.Hotta, K.Mizuma, T.Izukawa, S.Abe and T.Sasaki,
PIXE Analysis of Water Leakage from a

Landfill Site of Industrial Waste-Geneating Hydrogen Sulfide,
Int. J. PIXE, 14, (2004) 57-66
S   ACT   42053

14J125
H.Komori, K.Mizuma, K.Ishii, H.Yamazaki, S.Matsuyama,   Ts.Amartaivan,   Y.Ohishi, M.Rodriguez, T.Yamaguchi and A.Suzuki,
Int. J. PIXE, Beam Damage of Cellular Samples in In-Air
Micro PIXE Analysis, 14(3&4), 2004, 75-81
S   ACT   42053

14J126
S.Harada,   K.Ishii,   A.Tanaka,   T.Satoh, S.Matsuyama,   H.Yamazaki,   T.Kamiya, T.Sakai, K.Arakawa, S.Oikawa and K.Sera,
Method for Determining the Localization of Trace Elements Observed by the Micro PIXE Camera,
Int. J. PIXE, 14 (3&4), 2004, 83-88
S   ACT   42053

14J127
R.Watanabe, J.Hara, C.Inoue, T.Chiba, Ts. Amartaivan, S.Matsuyama, H.Yamazaki and K.Ishii,
Mapping of Heavy Metals Accumulated in Plants Using Submilli-PIXE Camera,
Int. J. PIXE, 14 (1&2), 2004, 35-42
S   ACT   42053

14J128
K.Ishii,   H.Yamazaki,   S.Matsuyama,   W. Galster, T.Satoh, and M.Budnar,
Contribution of Atomic Bremsstrahlung in PIXE spectra and screening effect in atomic bremsstrahlung,
X-ray Spectrometry, 34 (2005) 363-365.
S   ACT   42053

14J129

H. Kudo, M. Nagata, H. Wakamatsu, S. Tomita,

Resonant Coherent Excitation of C^{5+} in Si Observed with Backward Electron Spectroscopy,

Nucl. Instrum. Methods B 229 (2005)227-231.

O · IOM 42054

14J130

S. Yokoyama, K. Sato, H. Noguchi, Su. Tanaka, T. Iida, S. Furuichi, Y. Kanda, Y. Oki and T. Kaneto,

Characterization of Radionuclides Formed by High-Energy Neutron Irradiation,

Radia. Protect. Dosim., in press.

C RSH 41061

14J131

A. Chiba, Y. Saitoh, S. Tajima,

Measurement of carbon cluster charge state passing through thin foils using a luminance plate,

Nucl. Instrum. Methods B 232 (2005) 32-36.

T ACT 42055

14J132

S. Okumura, K. Arakawa, M. Fukuda, Y. Nakamura, W. Yokota, T. Ishimoto, S. Kurashima, I. Ishibori, T. Nara, T. Agematsu, M. Sano,T. Tachikawa,

Magnetic field stabilization by temperature control of an azimuthally varying field cyclotron magnet,

Rev. Sci. Instrum. 76, 033301(2005).

C ACT Machine Study

This is a blank page.

A.1.2 Publications in Proceeding

14C01

M. Imaizumi, T. Sumita, S. Kawakita, T. Ohshima, H. Ito, and S. Kuwajima,
Analysis of Flight Demonstration Results of an InGaP/GaAs Dual- Junction Tandem Solar Cell
Proc. of 31st IEEE Photovoltaic Specialists Conf., January 2005 (Lake Buena Vista) in press.
C T I   SCS   41004   42003

14C02

T. Sumita, M. Imaizumi, S. Kuwajima, T. Ohshima, and H. Itoh
Analysis of prediction methodology for triple-junction cell in composite radiation environment
Proc. of 31st IEEE Photovoltaic Specialists Conf., January 2005 (Lake Buena Vista) in press.
C T I   SCS   41004   42003

14C03

T. Ohshima, T. Sumita, M. Imaizumi, S. Kawakita, K. Shimazaki, S. Kuwajima, A. Ohi, and H. Itoh
Evaluation of The Electrical Characteristics of III-V Compound Solar Cells Irradiated with Protons at Low Temperature
Proc. of 31st IEEE Photovoltaic Specialists Conf., January 2005 (Lake Buena Vista) in press.
C T I   SCS   41004, 42003

14C04

K. Shimazaki, M. Imaizumi, S. Kuwajima, K. Sakurai, K. Matsubara, and S. Niki
Computational Design of Optical Coatings for Thermal Control of Thin Film Cu(In,Ga)Se2 Solar Cell for Space Applications

Proc. of 19th European Photovoltaic Solar Energy Conf. and Exhibition, June 2004 (Paris), pp. 3575-3580
C T I   SCS   41004, 42003

14C05

S. Kawakita, K. Shimazaki, M. Imaizumi, S. Kuwajima, S. Yoda, T. Ohshima, T. kamiya, and S. Nakasuka
Demonstration of Cu(In,Ga)Se2 Thin-Film Solar Cells and Modules by Microsatellites
Proc. of 19th European Photovoltaic Solar Energy Conf. and Exhibition, June 2004 (Paris), pp. 3598-3601
C T I   SCS   41004, 42003

14C06

T. Ohshima, T. Sumita, M. Imaizumi, S. Kawakita, K. Shimazaki, S. Kuwajima, A. Ohi, H. Itoh
Evaluation of the Electrical Characteristics of III-V Compounds Solar Cells Irradiated with Protons at Low Temperature
Proceedings of 31st IEEE Photovoltaic Specialists Conference 2005, 3-7 Jan. 2005, Florida (USA) pp.806-809.
C   SCS   41007

14C07

M. Imaizumi, T. Sumita, S. Kawakita, T. Ohshima, H. Itoh, and S. Kuwajima,
Analysis of flight demonstration results of an InGaP/GaAs dual-junction tandem solar cell
Proceedings of 31st IEEE Photovoltaic Specialist Conference 2005, 3-7 Jan., 2005 Florida (USA) pp.563-566.
C T I   SCS   41007   42005

14C08

T. Sumita, M. Imaizumi, T. Ohshima, H. Itoh,

and S. Kuwajima,
Analysis of EOL prediction methodology for triple-junction solar cells in actual radiation environment,
Proceedings of 31st IEEE Photovoltaic Specialist Conference 2005, 3-7 Jan., 2005 Florida (USA) pp.667-670.
C T I. SCS 41007 42005

14C09
N. J. Ekins-Daukes, K. Arafune, H. S. Lee, T. Sasaki, M. Yamaguchi, A. Khan, T. Takamoto, T. Agui, K. Kamimura, M. Kaneiwa, M. Imaizumi, T. Ohshima, and H. Itoh,
Native and radiation induced defects in lattice mismatched InGaAs and InGaP
Proceedings of 31st IEEE Photovoltaic Specialist Conference 2005, 3-7 Jan., 2005 Florida (USA) pp.683-686.
T SCS 42005

14C10
H. Shindou, S. Kuboyama, N. Ikeda, S. Matsuda. T. Hirao
Bulk Damage Caused by Single Protons in SDRAMs
The IEEE Nuclear and Space Radiation Effects Conference(NSREC 2003).
C SCS 41002

14C11
S. Kuboyama, H. Shindo S. Matsuda, T. Hirao
Consistency of Bulk Damage Factor and NIEL for Electrons, Protons, and Heavy Ions in Si CCDs
The IEEE Nuclear and Space Radiation Effects Conference(NSREC 2002).
C SCS 41002

14C12
A. Makihara, S. Kuboyama, S. Matsuda, N. Nemoto, H. Ohtomo, K. Furuse, S. Baba and T.

Hirose
Non-Damaging Beam Blanking SEM Test Method and its Application to Highly Integrated Devices
The IEEE Nuclear and Space Radiation Effects Conference(NSREC 2001).
C SCS 41002

14C13
A. Makihara, H. Shindou, N. Nemoto, S. Kuboyama, S. Matsuda, T. Ohshima, T. Hirao, H. Itoh, S. Buchner, A. B. Campbell
Analysis of. Single-Ion Multiple-Bit Upset in High-Density DRAMs
The IEEE Nuclear and Space Radiation Effects Conference(NSREC 2000)..
C SCS 41002

14C14
T. Hirao, J. S. Laird, S. Onoda, T. Shibata, T. Wakasa, T. Yamakawa, H. Abe, Y. Takahashi, K. Ohnishi and H. Itoh
Charge collected in Si MOS Capacitors and SOI Devices $P^{+}N$ Diodes due to Heavy Ion Radiation
Proc. of the 6th International Workshop on Radiation Effects on Semiconductor Devices for Space Application, Oct. 2004 (Tsukuba) p.105
C SCS 41003

14C15
Y. Takahashi, T. Shibata, Y. Murase, K. Ohnishi, T. Hirao and T. Kamiya
Heavy-Ion induced Current in MOS Structure
Proc. of the 6th International Workshop on Radiation Effects on Semiconductor Devices for Space Application, Oct. 2004 (Tsukuba) p.111
C SCS 41003

14C16

T. Abe, K. Ohnishi, Y. Takahashi and T. Hirao
Consideration to Reliability of Laser Testing
for Evaluating SEU Tolerance
Proc. of the 6th International Workshop on
Radiation Effects on Semiconductor Devices
for Space Application, Oct. 2004 (Tsukuba)
p.157
C SCS 41003

14C17
H. Fukui, M. Hamaguchi, H. Yoshimura, H.
Oyamatsu, F. Matsuoka, T. Noguchi, T. Hirao,
H. Abe, S. Onoda, T. Yamakawa, T. Wakasa,
T. Kamiya
Comprehensive Study on Layout Dependence
of Soft Errors in CMOS Latch Circuits and Its
Scaling Trend for 65 nm Technology Node and
Beyond
2005 Symposium on VLSI Technology Digest
of Technical Papers, June 2005 (Kyoto) p. 222.
C SCS 41006

14C18
T. Wakasa, T. Hirao, T. Sanami, S. Onoda, H.
Abe, Su. Tanaka, T. Kamiya, T. Okamoto, H.
Itoh,
Measurement and Analysis of Single Event
Transient Current Induced in Si Devices by
Quasi-Monoenergetic Neutrons,
The 6nd International Workshop on Radiation
effects of Semiconductor Devices for Space
Application, pp.213-216 (2004).
C SCS 41005

14C19
T. Hirao, T. Wakasa, T. Sanami, S. Onoda, H.
Abe, Su Tanaka, T. Okamoto, Y. Koizumi, T.
Kamiya, H. Itoh,
Measurement of Single-Event Transient
Current Induced by Quasi-Monoenergetic
Neutron in a Si PIN photodiode,
5th Radiation and its Effects on Components

and Systems (RADECS) Workshop,
pp.185-188 (2004).
C SCS 41005

14C20
J. S. Laird, T. Hirao, S. Onoda, T. Wakasa, T.
Yamakawa, H. Abe, T. Kamiya, and H. Itoh,
Time-resolved laser and ion microbeam studies
of single event transient in high speed
optoelectronic devices,
Proceedings of the 6th International Workshop
on Radiation Effects on Semiconductor
Devices for Space Application, October 2004
(Tsukuba) pp.125-129.
T SCS 42002

14C21
T. Hirao, J. S. Laird, S. Onoda, T. Shibata, T.
Wakasa, T. Yamakawa, H. Abe, Y. Takahashi,
K. Ohnishi, H. Itoh,
Charge Collected in Si MOS Capacitors and
SOI Devices p+n Diodes due to Heavy Ion
Irradiation,
The 6nd International Workshop on Radiation
effects of Semiconductor Devices for Space
Application, pp.105-109 (2004).
T SCS 42001

14C22
T. Hirao, T. Shibata, J. S. Laird, S. Onoda, Y.
Takahashi, K. Ohnishi, T. Kamiya,
Experimental Study of Single-Event Transient
Curent in SOI Devices,
7th European Conference on Radiation and its
Effects on Components and Systems
(RADECS 2003), pp.305-310 (2003).
C T SCS 42001

14C23
T. Hirao, J. S. Laird, S. Onoda, T. Shibata, T.
Wakasa, T. Yamakawa, H. Abe, Y. Takahashi,
K. Ohnishi, and H. Itoh,

Charge collected in Si MOS capacitors and SOI devices p^+n diodes due to heavy ion irradiation,

Proceedings of the 6th International Workshop on Radiation Effects on Semiconductor Devices for Space Application, October 2004 (Tsukuba) pp.105-109

CT SCS 41001

14C24

Y. Takahashi, T. Shibata, Y. Murase, K. Ohnishi. T. Hirao, and T. Kamiya,

HEAVY-ION INDUCED CURRENT IN MOS STRUCTURE

Proceedings of the 6th International Workshop on Radiation Effects on Semiconductor Devices for Space Application, October 2004 (Tsukuba) pp.111-114

C SCS 41001

14C25

T. Abe, K. Ohnishi, Y. Takahashi, and T. Hirao,

CONSIDERATION TO RELIABILITY OF LASER TESTING FOR EVALUATING SEU TOLERANCE

Proceedings of the 6th International Workshop on Radiation Effects on Semiconductor Devices for Space Application, October 2004 (Tsukuba) pp. 157-160

C SCS 41001

14C26

T. Ohshima, H. Itoh

Change in the electrical characteristics of p-channel 6H-SiC MOSFET by gamma-ray irradiation

Proceedings of the 6th international workshop on radiation effects on semiconductor devices for space application, Oct. 6-8, 2004, Tsukuba (Japan) pp.191-194.

I SCS 42004

14C27

A. Wakahara, T. Fujiwara, H. Okada, A. Yoshida, T. Ohshima, and H. Itoh,

Energy-back-transfer process in rare-earth doped AlGaN,

MRS Spring meeting, March 2005 (San Francisco) V3.9

T SCS 42008

14C28

T. Fujiwara, A. Wakahara, Y. Nakanishi, H. Okada, A. Yoshida, T. Ohshima, and T. Kamiya,

Photoluminescence properties of Eu-implanted $Al_xGa_{1-x}N (0 \leqq x \leqq 1)$,

The 2004 Int. Workshop on Nitride Semiconductors (IWN2004), July 2004 (Pittsburgh) P8.32

T SCS 42008

14C29

A. Wakahara, Y. Nakanishi, T. Fujiwara, H. Okada, A. Yoshida, T. Ohshima, and T. Kamiya,

Enhancement of Tb-related cathodoluminescence in $Al_xGa_{1-x}N (0 \leqq x \leqq 1)$,

The 2004 Int. Workshop on Nitride Semiconductors (IWN2004), July 2004 (Pittsburgh) P8.28

T SCS 42008

14C30

A. Wakahara, T. Fujiwara, Y. Nakanishi, H. Okada, A. Yoshida, T. Ohshima, T. Kamiya, and Y.-T. Kim,

Fabrication and Characterization of Rare-earth Doped AlGaN for Light Source Application of Bio-MEMS,

Int. Conf. on Electrical Engineering 2004/ Asia-Pasific Conf. on Transducers and Micro-Nano Technology 2004 (ICEE2004/APCOT MNT 2004), July 2004

(Sapporo), OB4-5, Proceedings, Vol.1, pp.44-49

T SCS 42008

14C31

M. Okamura

Application of Ion-beams to Plant Science and Commercialization

Plant Cell Physiol. Vol.46 Supplement , s21 (2005)

C BIT 41013

14C32

M. Okamura, N. Yasuno, M. Takano, A. Tanaka, and Y. Hase,

Mutation Generation and the Development of New Varieties in Ornamentals by Ion Beam Breeding

JAERI-Review 2004-033, 50-51 (2004)

C BIT 41013

14C33

K. Ueno, T. Shirao, S. Nagayoshi, S. Imakiire, K. Kooriyama, Y. Hase, A. Tanaka,

Additional improvement of *Chrysanthemum* using Ion Beam re-irradiation.

Breeding Sci. conf (2005) :

C BIT 41014

14C34

T. Sato,

Breeding of Chrysanthemum.

Annual of Akita prefecture Agricultural experiment station (2004) in press .

C BIT 41019

14C35

M. Kondo, N. Hamato, Y. Hoshi, Y. Hase, N. Shikazono, A. Tanaka and H. Kobayashi,

Mutation induction by Ion-beam irradiation to the calluses and analysis of regenerated plants in Japanese bunching onion

J.Japan.Soc.Hort.Sci.73(Suppl. 2), September 2004 Meeting (Shizuoka) p.266.

C BIT 41020

14C36

Y. Hase, K. H. Trung and A. Tanaka,

Characterization of UV-B resistant Arabidopsis uvi4 mutant.

Plant Cell Physiology 46, supplement 161.

C BIT 41027

14C37

K. Akeo, Y. Akeo, A. Ogawa, T. Funayama, Y. Kobayashi

Effects of ion beam irradiation on genes related to apoptosis in the ciliary body.

15th Annual Meeting of Ocular Oxidative Stress Research Society 11. 26. 2004. Osaka

O BIT 41038

14C38

K. Akeo, T. Funayama, Y. Kobayashi, Y. Akeo

Ion beam irradiation has different influences on glutathione peroxidase of retinal pigment epithelial cells among ^{20}Ne, ^{12}C, and ^{4}He

109th Annual Meeting of Japanese Ophthalmological Society. 3. 24 2005. Kyoto

O BIT 41038

14C39

K. Akeo, T. Funayama, A. Ogawa, Y. Kobayashi, Y. Akeo

The effects of irradiation by ion beams on the morphology and p53-regulated Bcl-2/Bax expression in the cultured ciliary body

The Association for Research in Vision and Ophthalmology. 5. 4 2005 Fort Lauderdale

O BIT 41038

14C40

H. Matsumoto, K. Takahashi, C. Matsudaira, N.

Yamada, S. Hayashi, Z. H. Jin, M. Hatashita, ,
p53-independent thermosensitization by nitric
oxide-generating agent in human NSCLC cells
in vitro and in vivo.
9th International Congress on Hyperthermic
Oncology (ICHO2004), St. Louis, MO, USA,
Apr 20-24, 2004. pp46-47
C BIT 41039

14C41
H. Matsumoto, S. Hayashi, M. Hatashita, T.
Ohnishi,
Induction of radio- or thermo-resistance by
nitric oxide-mediated bystander effect.
3rd International Conference on the Biology,
Chemistry and Therapeutic Application of
Nitric Oxide (NO2004), Nara, Japan, May
24-28, 2004. pp77
C BIT 41039

14C42
T. Okuda, M. Watanabe, T. Kikawada, A.
Fujita, E. Forczek,
Cryptobiosis in the African chironomid:
physiological mechanism to survive complete
dehydration.
Proc. Arthropod Embryo. Soc. Jpn 39: 1-7
(2004).
C BIT 41040

14C43
M. Saitou, T. Sugihara, K. Tanaka and Y.
Oghiso,
Gene Expression Analysis of Radiation-Highly
Sensitive Mouse Cultured Cells Exposed to
Low Dose Radiation – Analysis of p53
Transcription Activity of Mouse Cultured
Cells by Irradiation to One Cell,
Effects of Low Dose-Rate Radiation on Genes.
The 2004 Fiscal Year Report of Institute for
Environmental Sciences, 2005. (In press) [In
Japanese]

C BIT 41041

14C44
Y. Kanasugi, K. Taklakura, T. Funayama, S.
Wada, T. Sakashita, Y. Kobayashi
Bystander Effects on Chromosomal
Aberrations Induced by Heavy Ion Beam
Irradiation.
Proc. of 47th Annual Meeting Japan Radiation
Research Society, November 2004 (Nagasaki)
p.34, 122
C BIT 41042

14C45
T. Ohshima, A. Uedono, H. Itoh, K. Abe, R.
Suzuki, T. Ohdaira, Y. Aoki, M. Yoshikawa, T.
Mokado, H. Okumura, S. Yoshida, S.
Tanigawa and I. Nashiyama,
Study of Thermal Annealing of Vacancies in
Ion-Implanted 3C-SiC by Positron
Annihilation
Proc. of Internat. conf. on Silicon Carbide,
III-nitrides and Related Materials, September
1997 (Stockholm) p.745.
I BIT 41044

14C46
K. Sakamoto, S. Fujimaki, N. Kawachi, S. Ishii,
N. Suzui, N. S. Ishioka, T. Tsukamoto, S.
Watanabe and S. Matsuhashi
Analysis of Transportation and distribution of
photosynthates in hemp with the
Positron-Emitting Tracer Imaging System
The 46th Annual Meeting of the Japanese
Society of Plant Physiologist (JSPP), March
2005 (Niigata) p.150.
I C 41049

14C47
S. Hasegawa, H. Koshikawa, Y. Maekawa, M.
Yoshida,
Optical resolution of racemic phenyl alanine

through PET membranes with chiral pore surface

Annual Meetings of The Chemical Society of Japan, 85th Spring Meeting 26-29 March 2005, Kanagawa University, C RCO 41056

14C48

Y. Yoshida, M. Taguchi, J. Yang, S. Seki, T. Kozawa, S. Tagawa, H. Shibata, M. Taguchi, H. Nanba, and T. Kojima,

Heavy ion beam pulse radiolysis for absorption spectroscopy

Proc. of Radiat. Chem. workshop, October 2003 (Hakone) p.102.

C RCO 41058

14C49

T. Sawai, M. Ando, E. Wakai, H. Tanigawa, S. Jitsukawa,

Hardening behavior of F82H irradiated by multi-beam in TIARA

The Japan Society of Plasma Science and Nuclear Fusion Research, and Atomic Energy Society of Japan, 5th United conference on Fusion Energy,2004, July (Sendai), p162.

T I S IOM 42010

14C50

T. Hirabayashi, H. Abe, T. Fukui, N. Sekimura

Microstructure of fullerene nanowhiskers and their stability under irradiation with electrons and ions

The 59th annual meeting of Japanese society of microscopy (2003)

I IOM 42018

14C51

H. Abe, T. Tadokoro, N. Sekimura

Experimental evidence of crowdion bundles by in-situ TEM under ion irradiations

The 59th annual meeting of Japanese society of microscopy (2003)

I IOM 42018

14C52

O. Shepelyev, N. Sekimura, H. Abe

Migration of interstitial complexes in irradiated Fe-Cr-Ni alloys

The 132nd JIM spring meeting (2004)

I IOM 42018

14C53

Y. Yang, H. Abe, N. Sekimura

Behavior of Dislocation Loops under Stress Environment

The 132nd JIM spring meeting (2004)

I IOM 42018

14C54

T. Tadokoro, H. Abe, N. Sekimura

Stability of displacement cascades in gold by in-situ TEM observations

The 132nd JIM spring meeting (2004)

I IOM 42018

14C55

H. Abe, T. Hirabayashi, N. Sekimura

Irradiation induced amorphization of fullerene nanowhiskers under irradiations with electrons and ions

The 132nd JIM spring meeting (2004)

I IOM 42018

14C56

Y. Yang, H. Abe, N. Sekimura

Behavior of Dislocation Loops under Stress Environment

The 132nd JIM spring meeting (2004)

I IOM 42018

14C57

H. Abe, N. Sekimura, R. E. Stoller, S. J. Zinkle

Studies for the formation and motion of SIA clusters by in-situ TEM observation and MD

simulations
3rd JUPITER –II Workshop on Interaction of Modeling and Design of Materials Systems for Fusion Blankets
I IOM 42018

14C58
H. Abe and N. Sekimura
Stability of interstitial-type defect clusters in Cu and Au
The 133rd JIM fall meeting (2004)
I IOM 42018

14C59
M. Ishikawa, H. Abe, Z. C. Li, N. Sekimura
Ion irradiation effects on coherency of precipitates in Cu-Co alloys
The 133rd JIM fall meeting (2004)
I IOM 42018

14C60
H. Abe, D. Hamaguchi and T. Sonoda
Electron microscopic investigations in cerium oxide under irradiations with ions and/or electrons
The 134th JIM fall meeting (2005)
I IOM 42018

14C61
S. Yamamoto, S. Nagata, A. Takeyama, M. Yoshikawa
Blister Formation in Rutile TiO_2 (100) Thin Films by Helium Ion Implantation
The 15th Symposium of The Materials Research Society of Japan Dec. 2004, Nihon University, Suruga-dai
Proceedings in press
S I IOM 42021

14C62
K. Takahiro, A. Terai, S. Oizumi, K. Kawatsura, S. Yamamoto, H. Naramoto

Amorphization of Carbon Materials Studied by X-ray Photoelectron Spectroscopy
14th International Conference on Ion Beam Modification of Materials (IBMM 2004), September 2004 (California), in press.
I IOM 42024

14C63
M. Takeuchi, Y. Matsumura, H. Uchida, T. Kuji and H. Abe,
Influence of Ion Beam Modification on Magnetostrictive Property of A RFe2 (R; Rare Earth) Thin Film,
The 9th International Conference on New Actuators and the 3rd International Exhibition on Smart Actuators and Drive Systems, June 2004, Germany (Bremen).
I T IOM 42034

14C64
R. Morimoto, H. Uchida and H. Abe,
Effects of Ion Irradiation on the Rate of Electrochemical Hydrogen Absorption of Pd,
International Hydrogen Energy Congress & Exhibition, July 2005, Turkey (Istanbul).
I T IOM 42034

14C65
H. Abe, R. Morimoto, F. Satoh, Y. Azuma and H. Uchida,
Effects of Surface Modification by Ion Irradiation on Electrochemical Hydriding Rate of Pd,
International Symposium on Metal-Hydrogen Systems Fundamentals & Applications 2004, September 2004, Poland (Cracow) in press.
I T IOM 42034

14C66
H. Abe, R. Morimoto, F. Satoh, Y. Azuma and H. Uchida,
Effects of Ion Irradiation on Electrochemical

Hydriding Rate of Misch-Metal Based Alloys,
The International Conference on Rare Earths,
November (2004), Japan (Nara) in press.
I T IOM 42034

14C67

M. Takeuchi, Y. Matsumura, H. Uchida and H. Abe,
Magnetostrictive Properties of Tb-Fe Thin Films Irradiated with Ar Ion,
The International Conference on Rare Earths,
November (2004), Japan (Nara) in press.
I T IOM 42034

14C68

K. Narumi, S. Sakai, H. Naramoto and K. Takanashi
Characterization of C_{60} Films Polymerized by Ion Irradiation
7th Biennial International Workshop Fullerenes and Atomic Clusters IWFAC'2005, St. Petersburg, Russia, June 27-July 1, 2005.
S IOM MAN 42025

14C69

H. Nishikawa, K. Fukagawa, T. Yanagi, Y. Ohki, E. Watanabe, M. Oikawa, T. Kamiya, K. Arakawa,
Proton Microbeam Irradiation Effects on Silica Glass,
1st International Workshop on Proton Beam Writing, Abstract No. 26, July, 18-22, 2004
I IOM 42038

14C70

H. Nishikawa, K. Fukagawa, T. Yanagi, Y. Ohki, E. Watanabe, M. Oikawa, T. Kamiya, K. Arakawa,
Spatial distribution of irradiation effects on silica glass induced by ion microbeam,
14th International Conference on Ion Beam Modification of Materials, Abstract No.87,

September 5-10, 2004
T I IOM 42038

14C71

K. Fukagawa, H. Nishikawa, T. Nakamura, Y. Ohki , M. Oikawa, T. Sato and K. Arakawa,
Dose dependence of irradiation effects on silica glass by ion microbeam Ⅱ,
Extended Abstracts (The 65th Autumn Meeting, 2004); The Japan Society of Applied Physics and Related Societies, No.2, p794, 1p-F-3
T I IOM 42038

14C72

K. Fukagawa, H. Nishikawa, T. Nakamura, Y. Ohki , M. Oikawa, T. Sato and K Arakawa,
Irradiation Effects on Silica glass by ion microbeam for fabrication of optical elements,
Proceedings of The 35th Symposium on Electrical and Electronic Insulating Materials and Applications in Systems, I-6、 pp.193-196、
November 17-18, 2004
T I IOM 42038

14C73

T. Nakamura, T. Yanagi, Y. Ohki, K. Fukagawa, H. Nishikawa, E. Watanabe, M. Oikawa, T. Sato and K. Arakawa,
Modification of Silica Glass for Optical Devices by Ion Microbeam Irradiation - Evaluation of the Microscopic Structural Change Including Densification by AFM -,
Proceedings of The 35th Symposium on Electrical and Electronic Insulating Materials and Applications in Systems, C-3、 pp.77-80、
November 17-18, 2004
T I IOM 42038

14C74

M. Murai, K. Fukagawa, H. Nishikawa, T. Nakamura, Y. Ohki , M. Oikawa, T. Sato and K. Arakawa,

Dose dependence of irradiation effects on silica glass by ion microbeam for different ion species,
Extended Abstracts (The 52nd Spring Meeting, 2005); The Japan Society of Applied Physics and Related Societies, No.2, p1019, 30p-ZG-5
T I IOM 42038

14C75
M. Murai, K. Fukagawa, H. Nishikawa, T. Nakamura, Y. Ohki , M. Oikawa, T. Sato and K. Arakawa,
Irradiation Effects on Silica Glass by Ion Microbeam for Fabrication of Optical Elements,
Proceedings of 2005 International Symposium on Electrical Insulating Materials, B3-7, pp.210-213, June 5-9, 2005, Kitakyushu, Japan
T I IOM 42038

14C76
S. Yamamoto, A. Takeyama, M. Yoshikawa
Characterization of sulfur-doped TiO_2 films by ion beam analysis
14th International Conference on Ion Beam Modification of Materials, IBMM2004 California, USA, September 5-10, 2004
S I IOM 42022

14C77
K. Awazu, H. Yasui, N. Ikenaga, T. Kawabata, Y. Hasegawa and N. Sakudo,
The properties of Hybrid Nanodiamond (HND) films (1),
Proceeding of the 110th Conference on The Surface Finishing Society of Japan, September 2004 (Matsushima) p.178.
T IOM 42026

14C78
H. Yasui, K. Awazu, N. Ikenaga, T. Kawabata, Y. Hasegawa and N. Sakudo,

The properties of Hybrid Nanodiamond (HND) films (2),
Proceeding of the 110th Conference on The Surface Finishing Society of Japan, September 2004 (Matsushima) p.179.
T IOM 42026

14C79
H. Yasui and K. Awazu,
Hydrogen analysis in DLC films by the high energy ion beam technique,
Proceeding of the 14th Radiation use technological seminar, October 2004 (Kanazawa) p.37.
T IOM 42026

14C80
Y. Mokuno, A. Chayahara, Y. Soda, Y. Horino, N. Fujimori,
Synthesizing single-crystal diamond by repetition of high rate homoepitaxial growth by microwave plasma CVD,
Proc. of the 10th International Conference on New Diamond Science and Technology, May 2005 (Tsukuba) p.54.
T IOM 42026

14C81
H. Yasui, K. Awazu, N. Ikenaga, Y. Hasegawa, N. Sakudo,
The properties of hybrid nanodiamond (HND) films
Proc. of the 10th International Conference on New Diamond Science and Technology, May 2005 (Tsukuba) p.157.
T IOM 42026

14C82
J. Vacik, H. Naramoto, K. Narumi, S. Yamamoto and H. Abe,
Synthesis and Characterization of the Nickel-Fullerene Nano-structured Materials

4th Int. Conf. on Materials Structures and Micromechnics of Fracture (MSMF-4), June 23-25, 2004 (Brno, Czech).

I S   IOM   32024

14C83

H. Naramoto, S. Sakai, K. Narumi, V. Lavrent'ev, J. Vacik and P. Avramov,

Structure Evolution Induced by Physical and Chemical Processes in the Mixtures between Co(Ni) and C_{60}

Proc. of the 1st Inter. Nanocarbon Workshop, July 30-31, 2005, (Hayama, Japan).

I S T   IOM   42027

14C84

P. Avramov, S. Sakai, H. Naramoto, V. Lavrantiev and K. Narumi

Quantum Chemical Investigation of Atomic and Electronic Structure of 1D Co/C_{60} Composites

Proc. of 1st NAREGI Inter. Nanoscience Conf., June 14-17, 2005 (Nara, Japan).

O   IOM   off line

14C85

S. Sakai, H. Naramoto, V. Lavrentiev, K. Narumi and A. Rikukawa,

Periodic Pattern Formation in Nickel-Fullerene Mixed Thin Films Induced by Penetrating Liquid-Indium

Proc. of 2005 Inter. Conf. on Surfaces, Coatings and Nanostructured Materials (nanoSMat 2005), September 6-9, 2005 (Aveiro, Portugal).

I S T   IOM   42027

14C86

H. Tanimoto, H. Mizubayashi, S.Sakai, K. Narumi and H. Naramoto,

Elasticity Study on irradiation-induced Polymerization and decomposition of C_{60} solid

Proc. of 14th Inter. Conf. on Internal Friction and Mechanical Spectroscopy, September 5-9, 2005 (Kyoto, Japan).

I T   IOM   42027

14C87

S. Sakai, H. Naramoto, T. Yaita, M. Maekawa, A. Kawasuso, P. Avramov, K. Narumi and Y. Baba,

Structures and Thermal Stabilities of Polymeric Transition Metal-C_{60} Compounds Evolved in Atomistically Mixed Thin Films

Proc. of 4th Inter. Sym. on Surface Science and Nanotechnology (ISSS-4), November 14-17, 2005 (Omiya, Japan).

I T   IOM   42027

14C88

N. S. Ishioka, S. Watanabe, S. Fujimaki, K. Sakamoto and S. Matsuhashi

Extention of the Irradiation System at TIARA for Production of Radioisotopes to Be Used in Plant Physiology

Proc. of the Internat. conf. on Cyclotrons and Their Applications, October 2004 (Tokyo, Japan) p.45-47.

C   NRI   41052

14C89

T. Satoh, M. Oikawa, T. Sakai, S. Okumura, S. Kurashima, M. Miyawaki, M. Fukuda, W. Yokota and T. Kamiya

Development of a High-enregy Heavy Ion Microbeam System at the JAERI AVF Cyclotron

Proc. of the 6th Internat. Workshop on Radiation Effects on Semiconductor Devices for Space Application, October 2004 (Tsukuba) p.207.

C   SCS   41060

14C90

C.-J. Ma, M. Kasahara, S. Tohno, M. Okumura,
T. Sakai,
The nature of Asian dust sources.
Proc. of 21st Symposium on Aerosol Science
and Technology, Aug. 2004 (Sapporo)
p.117-118.
S RCO 42041

14C91
M. Okumura, C.-J. Ma, M. Kasahara, S. Tohno,
T. Sakai,
2004. The chemical characteristics of spring
aerosols on the West Coast of Korea.
Proc. Of 21st Symposium on Aerosol Science
and Technology, Aug. 2004 (Sapporo)
pp.67-68.
S RCO 42041

14C92
T. Ohshima, T. Satoh, M. Oikawa, T.
Yamakawa, S. Onoda, T. Wakasa, J. S. Laird,
T. Hirao, T. Kamiya, H. Itoh, A. Kinoshita , R.
Tanaka, I. Nakano, M. Iwami, Y. Fukushima
Analysis of transient current induced in silicon
carbide diodes by oxygen-ion microbeams
Proceedings of the 6th international workshop
on radiation effects on semiconductor devices
for space application, Oct. 6-8, 2004, Tsukuba
(Japan) pp.177-180.
T I SCS ACT 42043

14C93
T. Nagamine,
Intracellular changes of trace elements by
interferon and zinc
21st Century COE program, The first
international symposium on Biomedical
research using accelerator technology, March
2005, Maebashi, p27-29
S ACT 42048

14C94

T. Kusakabe
Significance about the phosphorous
measurement in air micro-PIXE
21st Century COE program, The first
international symposium on Biomedical
research using accelerator technology, March
2005, Maebashi, p60
S ACT 42048

14C95
K. Nakazato, K. Suzuki, T. Nagamine, K.
Nakajima,T. Sakai.
Storage of cadmium in the liver and kidney
following a long term period of oral
administration of cadmium.
The 16th Japan Society for Biomedical
Research on Trace Elements, June 2005
(Kyoto) p160
S ACT 42048

14C96
S. Harada, S. Ehara, K. Ishii, A. Tanaka, T.
Satoh, S. Matsuyama, H. Yamazaki, Y.
Komori, T. Kamiya, T. Arakawa, M. Saitoh, M.
Oikawa, and K. sera.
Innovation of the Target preparation of the
micro PIXE Camera for the floating cells.
Proceeding of the 10 th International
Conference on Particle-Induced X-ray
Emission and its Analytical Applications
(CDR publication)
S BIT 42051

14C97
S. Harada, S. Ehara, K. Ishii, A. Tanaka, T.
Satoh, S. Matsuyama, H. Yamazaki, Y.
Komori, T. Kamiya, T. Arakawa, M. Saitoh, M.
Oikawa, and K. sera.
The alteration of the cis-platinum (Platinum
analogues for cancer therapy) by the low dose
irradiation studied in human leukemia, A
preliminary study.

Proceeding of the 10 th International Conference on Particle-Induced X-ray Emission and its Analytical Applications (CDR publication)

S BIT 42051

14C98

K. Ishii, H. Yamazaki, S. Matsuyama, W. Galster, T. Satoh, and M. Budnar,

Continuous background in PIXE: Screening Effect in Atomic Bremsstrahlung,

Proceedings of 10th International conference on PIXE and its applications, Portoroz, Slovenia, June 4-8, 2004, 160.1~4, http//pixe2004.ijs.si/,.

S ACT 42053

14C99

S. Harada, S. Ehara, K. Ishii, H. Yamazaki, S. Matsuyama, K. Mizuma, K. Hotta, T. Izukawa, S. Abe, S. Obara, T. Kamiya, T. Sakai, T. Satoh, and S. Oikawa,

A new target preparation procedure of the micro-PIXE Camera for the floating cells,

Proceedings of 10th international conference on PIXE and its applications, Portoroz, Slovenia, June 4-8, 2004, 821.1~3, http//pixe2004.ijs.si/.

S ACT 42053

14C100

S. Matsuyama, K. Ishii, S. Abe, H. Ohtsu, H. Yamazaki, A. Suzuki, Ts. Amartaibvan, Y. Barbotteau, T. Yamaguchi, G. Momose, K. Inomata, Y. Watanabe, T. Kamiya, M. Oikawa, K. Arakawa and H. Imazeki,

Micro-beam Analysis at Tohoku University for Biological Studies,

Proceedings of 10th international conference on PIXE and its applications, Portoroz, Slovenia, June 4-8, 2004, 931.1~3, http//pixe2004.ijs.si/.

S ACT 42053

14C101

Ts. Amartaibvan, K. Ishii, H. Yamazaki, S. Matsuyama, A. Suzuki, T. Yamaguchi, S. Abe, K. Inomata, and Y. Watanabe,

PIXE Analysis using 70 MeV Carbons,

Proceedings of 10th international conference on PIXE and its applications, Portoroz, Slovenia, June 4-8, 2004, 823.1~3, http//pixe2004.ijs.si/.

S ACT 42053

14C102

H. Yamazaki, K. Ishii, Y. Takahashi, S. Matsuyama, Ts. Amartaibvan, A. Suzuki, T. Yamaguchi, G. Momose, K. Hotta, T. Izukawa, K. Mizuma, and S. Abe,

Quantitative Analysis of Arsenic Environmental Water samples by using PIXE,

Proceedings of 10th international conference on PIXE and its applications, Portoroz, Slovenia, June 4-8, 2004, 911.1~3, http//pixe2004.ijs.si/.

S ACT 42053

14C103

S. Harada, S. Ehara, K. Ishii, H. Yamazaki, S. Matsuyama, K. Mizuma, K. Hotta, T. Izukawa, S. Abe, S. Obara, T. Kamiya, T. Sakai, T. Satoh, and S. Oikawa,

The alteration of the Carboplatin (Platinum analogues for cancer therapy) by the low dose irradiation studied in human leukemia, A preliminary study,

Proceedings of 10th international conference on PIXE and its applications, Portoroz, Slovenia, June 4-8, 2004, 706.1~3, http//pixe2004.ijs.si/.

S ACT 42053

14C104

M. Hagiwara, T. Sanami, M. Baba, T. Ohishi, N. Hirabayashi, M. Takada, H. Nakashima and S. Tanaka
Measurement of Double Differential Cross Section of Secondary Heavy Particles Induced by Tens of MeV Particles
Proc. of Internat. conf. on Nuclear Data for Science and Technology, September 2004 (Saint Fe) p.1031.
C ACT 41062

14C105
S. Kurashima, M. Fukuda, N. Miyawaki, S. Okumura, K. Yoshida, T. Nara, T. Agematsu, I. Ishibori, K. Arakawa. Y. Nakamura
DEVELOPMENT OF THE FLAT-TOP ACCELERATION SYSTEM FOR THE JAERI AVF CYCLOTRON
Proc. 17th Int. Conf. on Cyclotron and Their Applications, Shibuya, JAPAN, 362 (2004).
C ACT Machine Study

14C106
S. Okumura, I. Ishibori, M. Fukuda, N. Miyawaki, S. Kurashima, T. Agematsu, T. Nara, K. Yoshida, Y. Nakamura, and K.

Arakawa,
Instrumentation for Measurement of Beam Energy Spread
Proceedings of the 17th International Conference on Cyclotrons and Their Applications, Tokyo, Japan (2004).p.410.
C ACT Machine Study

14C107
Y. Nakamura, T. Nara, T. Agematsu, I. Ishibori, S. Kurashima, M. Fukuda, S. Okumura, W. Yokota, K. Yoshida, N. Miyawaki, and K. Arakawa
Status Report on JAERI-AVF Cyclotron System
Proceedings of the 17th International Conference on Cyclotrons and Their Applications, Tokyo, JAPAN, pp 157-159 (Oct/2004)
C STA Machine Study

Appendix 2. Type of Research Collaboration

Section of this Report	Reseach Program Number	Type of Research Collaborations*	Section of this Report	Reseach Program Number	Type of Research Collaborations*
1.1	41004/42003	Joint.Res.	2.35	41042	Coop.Res.Univ.
1.2	41007/42005	Joint.Res.	2.36	41043	Coop.Res.Univ.
1.3	41002/42003	Joint.Res.	2.37	41044	Joint Res. Proj.
1.4	41003	Coop.Res.Univ.	2.38	41045	Joint Res. Proj.
1.5	41005	Coop.Res.Univ.	2.39	41046	Joint Res. Proj.
1.6	41006/42006	Joint.Res.	2.40	41047	Joint Res. Proj.
1.7	42002	JAERI	2.41	41048	Joint Res. Proj.
1.8	42001	JAERI	2.42	41049	JAERI
1.9	4001	JAERI	2.43	41050	Coop.Res.Univ.
1.10	42007	Coop.Res.Univ.	2.44	41051	Joint.Res.
1.11	42004	JAERI	2.45	41065	JAERI
1.12	42008	Coop.Res.Univ.	2.46	41067	JAERI
			2.47	41068	Joint Res. Proj.
2.1	41008	Coop.Res.Univ.	2.48	41069	Joint Res. Proj.
2.2	41009	Joint.Res.	2.49	42057	Joint Res. Proj.
2.3	41010	Joint.Res.			
2.4	41011	JAERI	3.1	41055	JAERI
2.5	41012	Joint.Res.	3.2	41064	JAERI
2.6	41013	Joint.Res.	3.3	41057	JAERI
2.7	41014	Joint.Res.	3.4	41058	Coop.Res.Univ.
2.8	41015	Joint.Res.	3.5	41059/42017	Coop.Res.Univ.
2.9	41016	Coop.Res.Univ.	3.6	42016	Joint Res. Proj.
2.10	41017	Coop.Res.Univ.			
2.11	41018	Coop.Res.Univ.	4.1	42009	Joint Res. Proj.
2.12	41019	Joint.Res.	4.2	42010	Joint Res. Proj.
2.13	41020	Joint.Res.	4.3	42011	Joint.Res.
2.14	41021	Coop.Res.Univ.	4.4	42012	JAERI
2.15	41022	Joint.Res.	4.5	42013	JAERI
2.16	41023	Coop.Res.Univ.	4.6	42014	JAERI
2.17	41024	Coop.Res.Univ.	4.7	42040	JAERI
2.18	41025	Coop.Res.Univ.	4.8	42018	Coop.Res.Univ.
2.19	41026	Joint.Res.	4.9	42019	Coop.Res.Univ.
2.20	41027	JAERI	4.10	42021	JAERI
2.21	41028	Joint.Res.	4.11	42023	JAERI
2.22	41030	Coop.Res.Univ.	4.12	42024	Coop.Res.Univ.
2.23	41031	Joint.Res.	4.13	42034	Coop.Res.Univ.
2.24	41032/42015	JAERI	4.14	42035	JAERI
2.25	41033	JAERI	4.15	42036	Coop.Res.Univ.
2.26	41034	JAERI	4.16	42025	JAERI
2.27	41035	Coop.Res.Univ.	4.17	42028	Joint Res. Proj.
2.28	41036	Joint.Res.	4.18	42029	JAERI
2.29	41037	Coop.Res.Univ.	4.19	42030	Coop.Res.Univ.
2.30	41038	Joint.Res.	4.20	42031	Coop.Res.Univ.
2.31	41039	Coop.Res.Univ.	4.21	42032	Coop.Res.Univ.
2.32	41040	Joint.Res.	4.22	42033	Coop.Res.Univ.
2.33	41041	Joint.Res.	4.23	42037	Coop.Res.Univ.
2.34	41042	Coop.Res.Univ.	4.24	42038	Coop.Res.Univ.

Section of this Report	Reseach Program Number	Type of Research Collaborations*
5.1	42022	JAERI
5.2	42026	Joint.Res.
5.3	42027	Joint Res. Proj.
6.1	41052	JAERI
6.2	41053	JAERI
6.3	41054	JAERI
6.4	off line	JAERI
7.1	41060	JAERI
7.2	42041	Coop.Res.Univ.
7.3	42042	JAERI
7.4	42044	JAERI
7.5	42045	Coop.Res.Univ.
7.6	42046	Joint Res. Proj.
7.7	42043	JAERI
7.8	42047	Joint Res. Proj.
7.9	42048	Joint Res. Proj.
7.10	42050	Joint Res. Proj.
7.11	42051	Joint Res. Proj.
7.12	42052	Joint Res. Proj.
7.13	42053	Joint Res. Proj.
7.14	42054	Joint Res. Proj.
8.1	41061	Joint Res. Proj.
8.2	41062	Joint Res. Proj.
8.3	41063	Joint Res. Proj.
9.1	42055	Joint Res. Proj.
9.2	42056	Joint Res. Proj.
9.3	Machine Study	JAERI
9.4	Machine Study	JAERI
9.5	Machine Study	JAERI
9.6	Machine Study	JAERI
9.7	Machine Study	JAERI

*Joint Res.: Joint research with private company or governmental institution
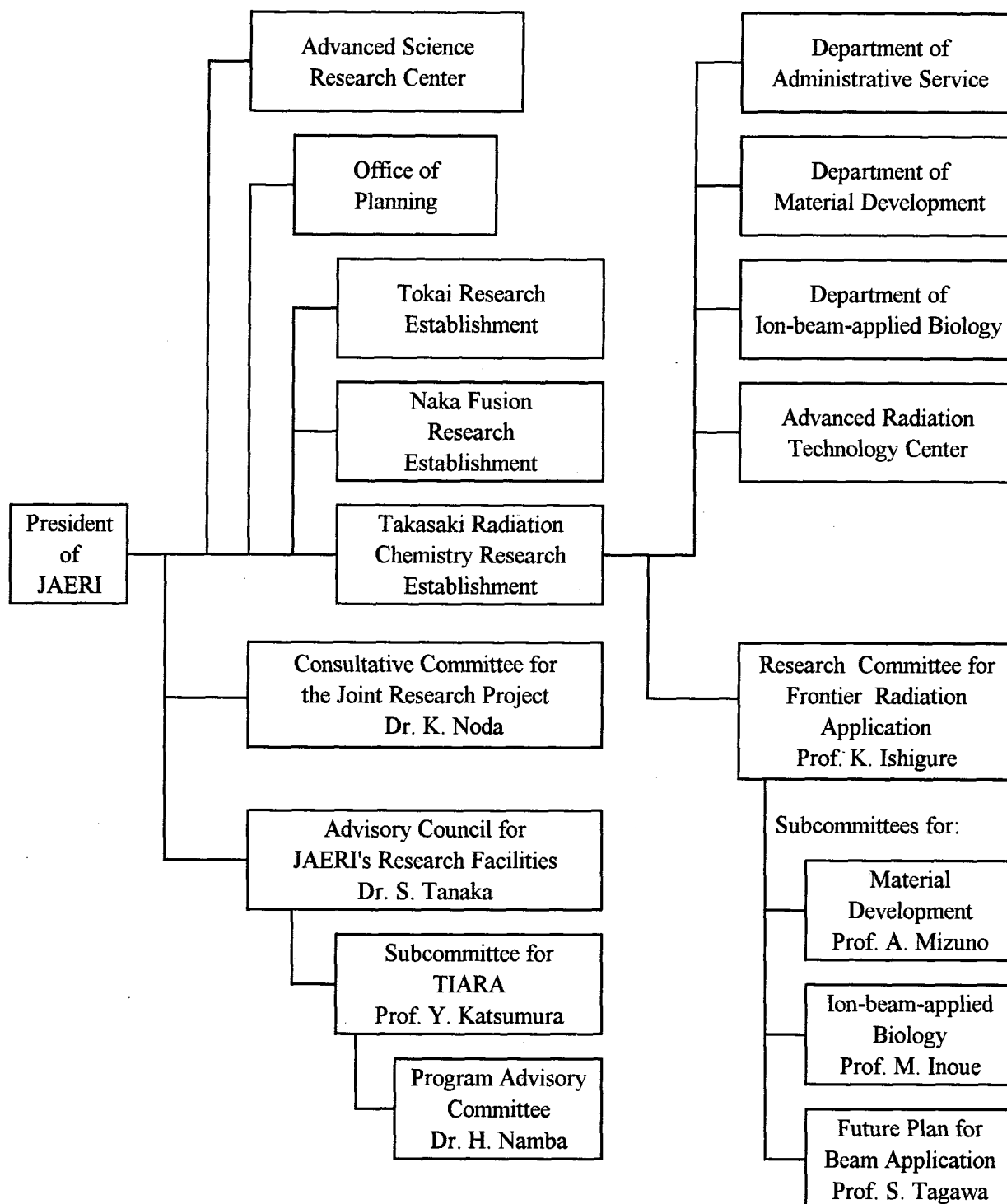Coop. Res. Univ.: Cooperative research with a university or universities
Joint Res. Proj. : The Joint Research Project #
#For administration of these programs, we appreciate the cooperation of
Research Center for Nuclear Science and Technology, The University of Tokyo.

Appendix 3. Organization and Personnel of TIARA (FY 2004)

1) Organization for the Research and Development of Advanced Radiation Technology

2) Personnel for the Administration, Operation and Control of TIARA

Advanced Radiation Technology Center

Director	Y. Ohara
Deputy Director	K. Arakawa
Senior Staff	I. Takada

Administration Division

General Manager	M. Otsubo
Staff Member	J.Kobayashi, T.Tabata

Utilization and Coordination Division

General Manager	Su. Tanaka
Staff Member	K. Nishimura, H. Kaneko, M. Hosono

Ion Accelerator Operation Division

General Manager	W. Yokota

Group of Cyclotron Operation

Staff Member	Y. Nakamura, T. Nara, T. Agematsu, I. Ishibori, S. Kurashima, K. Yoshida

Guoup of Electrostatic Accelerators Operation

Staff Member	K. Mizuhashi, S. Uno, K. Ohkoshi, A. Chiba, K.Yamada

Ion Beam Engineering Division

Head	M. Fukuda
Staff Member	S. Okumura, Y. Saito, Y. Ishii, T. Sakai, T. Satoh, N. Miyawaki, M. Oikawa, H. Kashiwagi

Irradiation Service Division

General Manager	H. Sunaga
Staff Member	T. Kanazawa, Y. Haruyama, N. Haneda, H. Hanaya, R.Yamagata

Department of Administrative Services

Safety Division

Staff Member (Radiation Monitoring and Control in TIARA)	Y. Asano, Y. Muto

Utilities and Maintenance Division

Staff Member (Radioactive Waste Management and Utility Control in TIARA)	M. Kawano, Y. Takayama